556836
P68

NASA Technical Memorandum 101656

NUMERICAL SOLUTION OF 3D NAVIER-STOKES EQUATIONS WITH UPWIND IMPLICIT SCHEMES

Yves P. Marx

JANUARY 1990

(NASA-TM-101656) NUMERICAL SOLUTION OF 3D NAVIER-STOKES EQUATIONS WITH UPWIND IMPLICIT SCHEMES (NASA) 65 p CSCL 01A
N90-19205
Unclas
G3/02 0271144

National Aeronautics and
Space Administration

Langley Research Center
Hampton, Virginia 23665

Abstract

An upwind MUSCL type implicit scheme for the three-dimensional Navier- Stokes equations is presented. Comparison between different approximate Riemann solvers (Roe and Osher) are performed and the influence of the reconstructions schemes on the accuracy of the solution as well as on the convergence of the method is studied. A new limiter is introduced in order to remove the problems usually associated with non-linear upwind schemes. The implementation of a "diagonal" upwind implicit operator for the three-dimensional Navier-Stokes equations is also discussed. Finally the turbulence modeling is assessed. Good prediction of separated flows are demonstrated if a non-equilibrium turbulence model is used.

1 Introduction

Much efforts have been deployed during the last years to build efficient numerical methods for the solution of the equations of compressible viscous flows. Following the pioneer work of Godunov [16], efficient upwind methods were developed [42,36] which enable an almost perfect capture of stationnary shocks. With the introduction of essentially non-linear schemes, TVD [52,17,47] and ENO [19,18] schemes, the good shock capturing properties of the first-order upwind schemes were extended to higher order schemes. Acceleration techniques were also improved, reducing the cost of the computation of steady states. The diagonal dominance of the jacobian matrices obtained with upwind schemes was for instance exploited to construct relaxation based implicit methods [8,27,49], which may eventually be combined with multigrid methods [20,3,31]. Non-elliptic multigrid techniques were also introduced for the centered approximation of the Euler equations [21]. In this case, the damping of the high frequencies arises from a careful design Runge-Kutta time stepping scheme combined with an adapted non-linear artificial dissipation term [23]. In [28] the procedure was extended to the Navier-Stokes equations and the success of the method is clearly demonstrated in [40,54]. While the numerical techniques were drastically improved, in the meantime no much progress were reported in the modeling of the Reynolds stresses. Thus, even if the computation of the flowfield around a complete aircraft has become possible, [22,50], realistic simulation of separated flows around complex geometries remains unpractical. In this report a newly developed code, enabling the simulation of three-dimensional flows with reverse flow regions, on simple geometries (wings) is presented. The report is outline as follows; after a short description of the equations to be solved (§2), the numerical procedure is detailed: the spatial discretization in §3, the time integration and acceleration technique in §4 and the boundary conditions in §5. The turbulence models used are then presented (§6) and finally in §7 the results are discussed.

2 Governing Equations

The basic equations used as the physical model are the integral form of the mass-averaged Navier-Stokes equations — Reynolds equations. Since the dominant viscous effects for high-Reynolds number flows arise from the diffusion normal to the body surfaces, the thin-layer approximation is employed. The turbulent transport of momentum and energy due to the fluctuations of velocity and pressure is modeled with the eddy viscosity concept making the form of the Reynolds equations identical to the form of the Navier-Stokes equations. The equations to be solved are then

$$\frac{\partial}{\partial t}\iiint_{\mathcal{V}} U\,dv + \iint_{\partial\mathcal{V}} \mathbf{F}\vec{n}\,ds = \iint_{\partial\mathcal{V}} \mathbf{F}_{V}\vec{n}\,ds \tag{1}$$

where

$$U = (\rho\,,\ \rho u\,,\ \rho v\,,\ \rho w\,,\ e)^{\mathrm{T}}$$

is the vector of the conserved variables. The quantity $\mathcal{V}$ denotes an arbitrary control volume, $\partial\mathcal{V}$ and $\vec{n}$ correspond then respectively to the boundary surface and the outer normal of this volume.

In the cartesian frame $(\vec{\imath},\vec{\jmath},\vec{k})$ the tensor $\mathbf{F}$ of the convection terms is

$$\mathbf{F} = \begin{bmatrix} \rho u & \rho v & \rho w \\ \rho u^2 + P & \rho uv & \rho uw \\ \rho uv & \rho v^2 + P & \rho vw \\ \rho uw & \rho vw & \rho w^2 + P \\ u(e+P) & v(e+P) & w(e+P) \end{bmatrix} \tag{2}$$

and the tensor $\mathbf{F}_V$ of the diffusion terms in the thin-layer approximation in the direction $\vec{\eta}$, is

$$\mathbf{F}_V = \begin{bmatrix} 0 & 0 & 0 \\ \sigma_{xx} & \sigma_{xy} & \sigma_{xz} \\ \sigma_{xy} & \sigma_{yy} & \sigma_{yz} \\ \sigma_{xz} & \sigma_{yz} & \sigma_{zz} \\ u\sigma_{xx} + v\sigma_{xy} + w\sigma_{xz} - q_x & u\sigma_{xy} + v\sigma_{yy} + w\sigma_{yz} - q_y & u\sigma_{xz} + v\sigma_{yz} + w\sigma_{zz} - q_z \end{bmatrix} \tag{3}$$

with

$$\begin{aligned}
\sigma_{xx} &= \lambda(\eta_x \frac{\partial u}{\partial \eta} + \eta_y \frac{\partial v}{\partial \eta} + \eta_z \frac{\partial w}{\partial \eta}) + \mu(2\eta_x \frac{\partial u}{\partial \eta}) \\
\sigma_{yy} &= \lambda(\eta_x \frac{\partial u}{\partial \eta} + \eta_y \frac{\partial v}{\partial \eta} + \eta_z \frac{\partial w}{\partial \eta}) + \mu(2\eta_y \frac{\partial v}{\partial \eta}) \\
\sigma_{zz} &= \lambda(\eta_x \frac{\partial u}{\partial \eta} + \eta_y \frac{\partial v}{\partial \eta} + \eta_z \frac{\partial w}{\partial \eta}) + \mu(2\eta_z \frac{\partial w}{\partial \eta}) \\
\sigma_{xy} &= \mu(\eta_y \frac{\partial u}{\partial \eta} + \eta_x \frac{\partial v}{\partial \eta}) \\
\sigma_{xz} &= \mu(\eta_z \frac{\partial u}{\partial \eta} + \eta_x \frac{\partial w}{\partial \eta}) \\
\sigma_{yz} &= \mu(\eta_z \frac{\partial v}{\partial \eta} + \eta_y \frac{\partial w}{\partial \eta}) \\
q_x &= -\frac{\gamma\mu}{\mathrm{Pr}} \eta_x \frac{\partial e_i}{\partial \eta} \\
q_y &= -\frac{\gamma\mu}{\mathrm{Pr}} \eta_y \frac{\partial e_i}{\partial \eta} \\
q_z &= -\frac{\gamma\mu}{\mathrm{Pr}} \eta_z \frac{\partial e_i}{\partial \eta}
\end{aligned}$$

where e_i represents the internal energy. The bulk viscosity λ is evaluated using the Stokes hypothesis

$$3\lambda + 2\mu = 0$$

and the molecular viscosity is determined from the Sutherlands law

$$\mu = \mu_\infty \left(\frac{T}{T_\infty}\right)^{\frac{3}{2}} \frac{T_\infty + 110.4}{T + 110.4}. \tag{4}$$

As a result of the eddy viscosity assumption, the equations (1) with the expression (3) for the tensor $\mathbf{F}_V$ correspond also to the Reynolds equations for turbulent flows if the molecular viscosity is replaced by an "effective" viscosity $\mu + \mu_t$ and the quantity $\frac{\mu}{\mathrm{Pr}}$ by $\frac{\mu}{\mathrm{Pr}} + \frac{\mu_t}{\mathrm{Prt}}$. The symbols μ_t and Prt used in the previous expressions denote respectively the eddy viscosity and the turbulent Prandtl number.

3 Numerical Method

The equations (1) are solved with an implicit upwind method of the form

$$\begin{aligned} (I + \Delta t\ \mathrm{L})\delta U &= -\Delta t\ \mathrm{R}^n \\ U^{n+1} &= U^n + \delta U \end{aligned} \tag{5}$$

where L is a spatial operator and R is the residual of the steady equations. No accuracy restriction will be imposed on the implicit operator as we are interested only in steady state solutions.

3.1 Computation of the residual

The computation of the residual is performed following the idea of Godunov [16] and generalized by Van Leer [53]. The procedure comprises of three stages. The first stage consists of the **Reconstruction** of the flowfield from its cell average values by piecewise polynomial approximations. In the second stage, the time **Evolution** (in the small, i.e. $0 \leq t < \varepsilon$) of the reconstructed flowfield is computed by solving, at each interface, a Riemann problem. The procedure is therefore "upwind" as the wave propagation is taken into account when the Riemann problem is solved. In the final stage, the solution obtained by the resolution of the Riemann problems is **Projected** on the cells and new average values are computed. This step makes the overall procedure conservative.

3.2 Reconstruction schemes

Two reconstruction schemes were employed, a second-order ENO scheme of Harten and Osher [19] and a family of upwind biased schemes known as the κ scheme. With the second-order ENO scheme, the smoothest parabola on the interval $[x_i, x_{i+1}]$ is first computed,

$$\mathrm{P}_{i+\frac{1}{2}}(x) = q_i + (x - x_i)\left[\frac{q_{i+1} - q_i}{x_{i+1} - x_i} + (x - x_{i+1})\delta^2 q\right]$$

with

$$\begin{aligned} \delta^2 q &= \mathbf{minmod}(Dq_{i-1}, Dq_i) \\ Dq_i &= \frac{1}{x_{i+2} - x_i}\left[\frac{q_{i+2} - q_{i+1}}{x_{i+2} - x_{i+1}} - \frac{q_{i+1} - q_i}{x_{i+1} - x_i}\right] \end{aligned}$$

where the **minmod** operator is defined as

$$\mathbf{minmod}(x, y) = \begin{cases} \mathrm{sign}(x)\ \min(|x|, |y|) & \text{if } \mathrm{sign}(x) = \mathrm{sign}(y) \\ 0 & \text{otherwise.} \end{cases}$$

The derivatives of $\mathrm{P}_{i+\frac{1}{2}}(x)$ and $\mathrm{P}_{i-\frac{1}{2}}(x)$ are then computed at x_i and the value of the slope of the reconstructed field on $\left[x_{i-\frac{1}{2}}, x_{i+\frac{1}{2}}\right]$ is obtained from

$$\delta^1 q = \mathbf{minmod}\left[\frac{d\mathrm{P}_{i+\frac{1}{2}}(x_i)}{dx}, \frac{d\mathrm{P}_{i-\frac{1}{2}}(x_i)}{dx}\right].$$

The cell interface values are therefore,

$$\begin{aligned} q_{L\,i+\frac{1}{2}} &= q_i + \frac{h_i}{2}\delta^1 q \\ q_{R\,i-\frac{1}{2}} &= q_i - \frac{h_i}{2}\delta^1 q \end{aligned}$$

with

$$h_i = x_{i+\frac{1}{2}} - x_{i-\frac{1}{2}}.$$

With the second-order ENO scheme, the computation of $\bar{u}^{n+1}$ involves the value of $\bar{u}^n$ at the points $i-3$ through $i+3$. This seven points stencil is required in order to distinguish between the variation of the flowfield near a shock from the variation of the flowfield near a smooth extremum. Five point schemes (like the κ scheme presented below) cannot ensure, even if the limiter is designed such as it does not "clip" at an extremum, second-order accuracy in the vicinity of all smooth extrema.

When the κ scheme is used, the left and right values at the $i+\frac{1}{2}$ cell interfaces are computed with an upwind biased interpolation,

$$\begin{aligned} q_{L\,i+\frac{1}{2}} &= q_i &+ \tfrac{h_i}{2} &\left[(1+\kappa)\delta q_{i+\frac{1}{2}} + (1-\kappa)\delta q_{i-\frac{1}{2}}\right] \\ q_{R\,i+\frac{1}{2}} &= q_{i+1} &- \tfrac{h_{i+1}}{2} &\left[(1+\kappa)\delta q_{i+\frac{1}{2}} + (1-\kappa)\delta q_{i+\frac{3}{2}}\right] \end{aligned} \qquad (6)$$

with

$$\delta q_{i+\frac{1}{2}} = \frac{q_{i+1} - q_i}{h_{i+1} + h_i}.$$

In order to ensure an interpolation which does not increase the Total Variation of the initial distribution, the gradients δq have to be limited. Following [6], the gradients were limited by replacing δq by $\tilde{\delta}$ with

$$\begin{aligned} \tilde{\delta}_i^+ &= \mathbf{minmod}\left[\frac{q_{i+1} - q_i}{h_{i+1} + h_i}, b\frac{q_i - q_{i-1}}{h_i + h_{i-1}}\right] \\ \tilde{\delta}_i^- &= \mathbf{minmod}\left[\frac{q_i - q_{i-1}}{h_i + h_{i-1}}, b\frac{q_{i+1} - q_i}{h_{i+1} + h_i}\right] \end{aligned}$$

where the value of b corresponds to the largest value for which the interpolated $q_{i+\frac{1}{2}}$ lies between q_i and q_{i+1},

$$b = \frac{3-\kappa}{1-\kappa}.$$

The cell interfaces values are thus computed with

$$\begin{aligned} q_{L\,i+\frac{1}{2}} &= q_i &+ \tfrac{h_i}{2} &\left[(1+\kappa)\tilde{\delta}_i^+ + (1-\kappa)\tilde{\delta}_i^-\right] \\ q_{R\,i+\frac{1}{2}} &= q_{i+1} &- \tfrac{h_{i+1}}{2} &\left[(1+\kappa)\tilde{\delta}_{i+1}^- + (1-\kappa)\tilde{\delta}_{i+1}^+\right]. \end{aligned} \qquad (7)$$

For $\kappa \in [-1,1]$ the κ scheme is second-order accurate and stable. The particular value $\kappa = \frac{1}{3}$ leads even to a third-order accurate scheme (on a uniform one-dimensional mesh). With the Chakravarthy-Osher limiter, the method is robust and when combined to the "third-order" scheme, fairly accurate results on coarse grids are obtained — see the result section. Unfortunatly, the Chakravarthy-Osher limiter has also the drawback of preventing the scheme to converge to the computer accuracy, hence a different limiter is proposed. The design of the new limiter was based on the following observations.

- In order to have a good convergence rate, smoothness is the name of the game, thus all non-linear changes should be made as smooth as possible.
- The only requirement in the design of a "monotone" shock capturing scheme, is to exclude the use of the gradients accross the shocks.

The procedure developed consists therefore to locate the shocks and to modify, in a *smooth* way, the gradients in their vicinities. As the difference of the unlimited left and right pressure values at the cell faces

$$x = |P_{i+\frac{1}{2}}\mathrm{L} - P_{i+\frac{1}{2}}\mathrm{R}|$$

is of the order of the truncation error in continuous flow regions and of the order of the shock strength in the vicinity of the shock, it can serve as a shock detector. The slopes are then limited according to

$$\tilde{\delta}_i^+ = \Phi\delta_i^+ \ ; \ \tilde{\delta}_i^- = \Phi\delta_i^- \tag{8}$$

where Φ is the restriction to the interval $[0,1]$ of the function $a(x-\varepsilon)^3 + 1.$ with

$$a = -10^5$$

$$\varepsilon = 10^{-7}.$$

The coefficient ε represents the value over which the limiting is effective. As $\Phi'(\varepsilon) = \Phi''(\varepsilon) = 0$, the limiter is smooth and the scheme is not too much sensitive to the value of ε. The coefficient a controls the strength of the limiting and was fixed by numerical experiments.

An other way used to limit the influence of the gradient accross the shock is to combine a fully upwind reconstruction, $\kappa = -1$, with an upwind computation of the fluxes. As the gradients have to be limited only near the shocks, a natural procedure is then to blend, using the shock detector function Φ, the actual value of κ with the fully upwind value $\kappa = -1$.

$$\tilde{\kappa} = \Phi\kappa + (1-\Phi)(-1). \tag{9}$$

In general, the downwind and upwind gradients should not be limited equally. For instance in the ideal shock case presented in the figure (1), only the gradient $\delta q_{i+\frac{1}{2}}$ must be limited. In order to distinctly limit the upwind and downwind gradients the ratios

$$r^- = |\frac{\delta^-}{\delta^+}|$$

and

$$r^+ = |\frac{\delta^+}{\delta^-}|$$

are introduced. If $r^- \ll 1$ ($\delta^+ \gg \delta^-$), respectively $r^+ \ll 1$ ($\delta^- \gg \delta^+$), only δ^+, respectively δ^-, must be limited. The restriction to the interval $[0,1]$ of the function

$$\theta(r) = \frac{b(r-\epsilon)^2+1}{c(r-\epsilon)^2+1} \ ; \ (\theta'(\epsilon)=0) \tag{10}$$

is therefore proposed to compute the limited gradients $\tilde{\delta}^\pm$,

$$\tilde{\delta}^\pm = [\Phi + (1-\Phi)\theta(r^\pm)]\,\delta^\pm. \tag{11}$$

The value $\theta(1)$ has to be set to zero in order to limit equally δ^+ and δ^- when the downwind and upwind gradients are identicals. This choice fixes the value of b. The coefficient c was determined by imposing $\theta(0.5) = 0.5$. In all the computations done with this new limiter, the value of ϵ was set to 0.003.

In summary, with the "smooth limiter" just described, the values $q_{i+\frac{1}{2}}$ at the cell faces are computed using the relation (7) in which the gradients $\tilde{\delta}^\pm$ were obtained through (11) and where the value κ was replaced by the blending $\tilde{\kappa}$ given in (9).

3.3 Resolution of the Riemann problem

In the original work of Godunov, the Riemann problems were solved exactly, but it has been proven that similar flowfields could be obtained at a lower cost if the Riemann problems were solved only approximately. Two of such approximate Riemann solvers are those proposed by Roe [42] and Osher [36]. Both rely on the wave decomposition. In the Roe scheme the decomposition is made by assuming a locally constant state $\tilde{U}$ for which

$$\begin{aligned} U_R - U_L &= \textstyle\sum_k \tilde{r}_k \tilde{\alpha}_k \\ F(U_R) - F(U_L) &= \textstyle\sum_k \tilde{\lambda}_k \tilde{r}_k \tilde{\alpha}_k \end{aligned} \tag{12}$$

where

$\tilde{\lambda}_k$ is an eigenvalue of the jacobian matrix $\frac{\partial F}{\partial U}(\tilde{U})$

$\tilde{r}_k$ is a right eigenvector of $\frac{\partial F}{\partial U}(\tilde{U})$

$\tilde{\alpha}_k = \tilde{l}_k(U_R - U_L)$ with $\tilde{l}_k$ a left eigenvector of $\frac{\partial F}{\partial U}(\tilde{U})$

In [44], Roe and Pike proved that the state $\tilde{U}$ for which the equations (12) are satisfied exist and is unique. It can be computed using the special averaging introduced by Roe in [42],

$$\begin{aligned} \tilde{\rho} &= \alpha\rho_R \\ \tilde{u} &= \tfrac{\alpha u_L + u_R}{1+\alpha} \\ \tilde{v} &= \tfrac{\alpha v_L + v_R}{1+\alpha} \\ \tilde{w} &= \tfrac{\alpha w_L + w_R}{1+\alpha} \\ \tilde{H} &= \tfrac{\alpha H_L + H_R}{1+\alpha} \end{aligned} \tag{13}$$

where

$$\begin{aligned} \alpha &= \sqrt{\frac{\rho_L}{\rho_R}} \\ H &= \frac{a^2}{\gamma - 1} + \frac{1}{2}(u^2 + v^2 + w^2). \end{aligned}$$

The Osher scheme is in some sense, a non linear extension of the Roe scheme. In the case of a non-linear hyperbolic system, the wave decomposition can be written as,

$$\begin{aligned} U_R - U_L &= \textstyle\sum_k \int_{\Gamma_k} r_k \, \mathrm{d}s_k \\ F(U_R) - F(U_L) &= \textstyle\sum_k \int_{\Gamma_k} \lambda_k r_k \, \mathrm{d}s_k \end{aligned} \tag{14}$$

where the Γ_k curves are defined by

$$\frac{dU}{ds_k} = r_k.$$

Using the constancy of the Riemann invariants along the Γ_k curves, explicit expressions for the integrals can be obtained [36] [29],

$$\begin{aligned} \textstyle\int_{\Gamma_1} \lambda_1 r_1 \, \mathrm{d}s_1 &= F(U_{i+\frac{1}{3}}) - F(U_i) \\ \textstyle\int_{\Gamma_2} \lambda_2 r_2 \, \mathrm{d}s_2 &= F(U_{i+\frac{2}{3}}) - F(U_{i+\frac{1}{3}}) \\ \textstyle\int_{\Gamma_3} \lambda_3 r_3 \, \mathrm{d}s_3 &= F(U_{i+1}) - F(U_{i+\frac{2}{3}}) \end{aligned} \tag{15}$$

with

$$U_{i+\frac{1}{3}} \; : \; \left[\begin{array}{l} \left. \begin{array}{lcl} u_{i+\frac{1}{3}} & = & \frac{\alpha u_i + u_{i+1}}{1+\alpha} - \frac{2}{\gamma - 1} \frac{a_{i+1} - \alpha a_i}{1+\alpha} \\ v_{i+\frac{1}{3}} & = & v_i \\ w_{i+\frac{1}{3}} & = & w_i \\ a_{i+\frac{1}{3}} & = & \frac{\gamma-1}{2} \frac{u_i - u_{i+1}}{1+\alpha} + \frac{a_{i+1} + a_i}{1+\alpha} \\ \rho_{i+\frac{1}{3}} & = & \left[\frac{\rho_i^\gamma a^2_{i+\frac{1}{3}}}{\gamma P_i} \right]^{\frac{1}{\gamma-1}} \\ P_{i+\frac{1}{3}} & = & \rho_{i+\frac{1}{3}} \frac{a^2_{i+\frac{1}{3}}}{\gamma} \end{array} \right\} \text{P variant} \\ \\ \left. \begin{array}{lcl} u_{i+\frac{1}{3}} & = & \frac{\alpha u_i + u_{i+1}}{1+\alpha} + \frac{2}{\gamma - 1} \frac{a_{i+1} - \alpha a_i}{1+\alpha} \\ v_{i+\frac{1}{3}} & = & v_i \\ w_{i+\frac{1}{3}} & = & w_i \\ a_{i+\frac{1}{3}} & = & -\frac{\gamma-1}{2} \frac{u_i - u_{i+1}}{1+\alpha} + \frac{a_{i+1} + a_i}{1+\alpha} \\ \rho_{i+\frac{1}{3}} & = & \left[\frac{\rho_i^\gamma a^2_{i+\frac{1}{3}}}{\gamma P_i} \right]^{\frac{1}{\gamma-1}} \\ P_{i+\frac{1}{3}} & = & \rho_{i+\frac{1}{3}} \frac{a^2_{i+\frac{1}{3}}}{\gamma} \end{array} \right\} \text{O variant} \end{array} \right. \qquad (16)$$

$$U_{i+\frac{2}{3}} \; : \; \left[\begin{array}{lcl} u_{i+\frac{2}{3}} & = & u_{i+\frac{1}{3}} \\ v_{i+\frac{2}{3}} & = & v_{i+1} \\ w_{i+\frac{2}{3}} & = & w_{i+1} \\ a_{i+\frac{2}{3}} & = & \alpha a_{i+\frac{1}{3}} \\ \rho_{i+\frac{2}{3}} & = & \frac{\rho_{i+\frac{1}{3}}}{\alpha^2} \\ P_{i+\frac{2}{3}} & = & P_{i+\frac{1}{3}} \end{array} \right\} \text{P and O variant.} \qquad (17)$$

Intermediate states between U_i, $U_{i+\frac{1}{3}}$ and $U_{i+\frac{2}{3}}$, U_{i+1} have also to be introduced in order to account for a possible change of the sign of $\lambda = u + a$ or $\lambda = u - a$. These intermediate states are

$$U^*_{i+\frac{1}{3}} \quad : \quad \left[\begin{array}{l} \left.\begin{array}{lcl} u^*_{i+\frac{1}{3}} & = & \frac{\gamma-1}{\gamma+1}\left(u_i + \frac{2a_i}{\gamma-1}\right) \\ v^*_{i+\frac{1}{3}} & = & v_i \\ w^*_{i+\frac{1}{3}} & = & w_i \\ a^*_{i+\frac{1}{3}} & = & u_{i+\frac{1}{3}} \\ \rho^*_{i+\frac{1}{3}} & = & \left[\frac{\rho_i^\gamma}{P_i}\frac{a^{*2}_{i+\frac{1}{3}}}{\gamma}\right]^{\frac{1}{\gamma-1}} \\ P^*_{i+\frac{1}{3}} & = & \rho^*_{i+\frac{1}{3}}\frac{a^{*2}_{i+\frac{1}{3}}}{\gamma} \end{array}\right\} \text{P variant} \\ \\ \left.\begin{array}{lcl} u^*_{i+\frac{1}{3}} & = & \frac{\gamma-1}{\gamma+1}\left(u_i - \frac{2a_i}{\gamma-1}\right) \\ v^*_{i+\frac{1}{3}} & = & v_i \\ w^*_{i+\frac{1}{3}} & = & w_i \\ a^*_{i+\frac{1}{3}} & = & -u_{i+\frac{1}{3}} \\ \rho^*_{i+\frac{1}{3}} & = & \left[\frac{\rho_i^\gamma}{P_i}\frac{a^{*2}_{i+\frac{1}{3}}}{\gamma}\right]^{\frac{1}{\gamma-1}} \\ P^*_{i+\frac{1}{3}} & = & \rho^*_{i+\frac{1}{3}}\frac{a^{*2}_{i+\frac{1}{3}}}{\gamma} \end{array}\right\} \text{O variant} \end{array}\right. \tag{18}$$

$$U^*_{i+\frac{2}{3}} : \left[\begin{array}{l} \left.\begin{array}{lcl} u^*_{i+\frac{2}{3}} &=& \frac{\gamma-1}{\gamma+1}\left(u_{i+1} - \frac{2a_{i+1}}{\gamma-1}\right) \\ v^*_{i+\frac{2}{3}} &=& v_{i+1} \\ w^*_{i+\frac{2}{3}} &=& w_{i+1} \\ a^*_{i+\frac{2}{3}} &=& -u_{i+\frac{2}{3}} \\ \rho^*_{i+\frac{2}{3}} &=& \left[\frac{\rho^\gamma_{i+1}}{P_{i+1}}\frac{a^{*2}_{i+\frac{2}{3}}}{\gamma}\right]^{\frac{1}{\gamma-1}} \\ P^*_{i+\frac{2}{3}} &=& \rho^*_{i+\frac{2}{3}}\frac{a^{*2}_{i+\frac{2}{3}}}{\gamma} \end{array}\right\} \text{P variant} \\ \\ \left.\begin{array}{lcl} u^*_{i+\frac{2}{3}} &=& \frac{\gamma-1}{\gamma+1}\left(u_{i+1} + \frac{2a_{i+1}}{\gamma-1}\right) \\ v^*_{i+\frac{2}{3}} &=& v_{i+1} \\ w^*_{i+\frac{2}{3}} &=& w_{i+1} \\ a^*_{i+\frac{2}{3}} &=& u_{i+\frac{2}{3}} \\ \rho^*_{i+\frac{2}{3}} &=& \left[\frac{\rho^\gamma_{i+1}}{P_{i+1}}\frac{a^{*2}_{i+\frac{2}{3}}}{\gamma}\right]^{\frac{1}{\gamma-1}} \\ P^*_{i+\frac{2}{3}} &=& \rho^*_{i+\frac{2}{3}}\frac{a^{*2}_{i+\frac{2}{3}}}{\gamma} \end{array}\right\} \text{O variant.} \end{array}\right. \tag{19}$$

Both with the Osher and Roe scheme the flux at the interface is computed using,

$$F_{i+\frac{1}{2}} = F(U_L) + \sum_k \Delta F_k^- \tag{20}$$

with the ΔF^- defined as

$$\Delta F_k^- = \int_{\Gamma_k} \lambda_k^- r_k \, \mathrm{d}s_k \tag{21}$$

or

$$\Delta F_k^- = \tilde{\lambda}_k^- \tilde{r}_k \tilde{\alpha}_k \tag{22}$$

and where

$$\lambda^- = \frac{\lambda - |\lambda|}{2}.$$

Because in the equation (21) the integration is made only on the negative part of λ, the integrand is not an exact differential and the values of the fluxes depend on the ordering in the integration path $\bigcup \Gamma_k$. For the Osher P variant, the integration path is Γ_{u-a} , Γ_u , Γ_{u+a} and for the O variant, it is Γ_{u+a} , Γ_u , Γ_{u-a}. A closer inspection of the integrals shows that if unlikely cases are discarded — supersonic flows in opposite directions on each side of the interface for instance — the computation of the flux at the interface requires at most three evaluations of fluxes for the P variant while it requires four evaluations for the O variant.

The above expressions are useful for computations in a cartesian mesh (the splitting for the Osher scheme was made in the i direction). For general meshes, the splitting is made in the direction normal to the cell face. Such a choice is computationally convenient but is also quite arbitrary; the splitting direction depends on the mesh rather than on the flow properties. In practice however, the procedure appeared to perform well and even if different grid independant splitting formulations have been known for several years [13,43,14,38], their efficiency are yet not fully established. With the "grid splitting" procedure, the extension to generalized coordinates of the approximate Riemann solvers is simple, the cartesian velocities u, v and w have just to be replaced by the contravariant velocities $\check{u}$, $\check{v}$ and $\check{w}$.

$$\begin{aligned} \check{u} &= n_x u + n_y v + n_z w \\ \check{v} &= l_x u + l_y v + l_z w \\ \check{w} &= m_x u + m_y v + m_z w \end{aligned} \tag{23}$$

where $\vec{n}$ is the vector normal to the cell interface and $\vec{l}$, $\vec{m}$ are the tangential vectors. In the two-dimensional case, the tangential vector is uniquely defined by the knowledge of the normal vector, in the three-dimensional case however, the normal vector defines only a *family* of tangential vectors $\vec{l}$ and $\vec{m}$. A precise definition of these tangential vectors can yet be avoided, by noticing that only the linear combination of the tangential velocities

$$\begin{aligned} \Omega_x &= l_x \check{v} + m_x \check{w} \\ \Omega_y &= l_y \check{v} + m_y \check{w} \\ \Omega_z &= l_z \check{v} + m_z \check{w} \end{aligned}$$

are needed, and that these linear combinations can also be written as

$$\begin{aligned} \Omega_x &= u - n_x \check{u} \\ \Omega_y &= v - n_y \check{u} \\ \Omega_z &= w - n_z \check{u}. \end{aligned} \tag{24}$$

Thus in practice, the tangential velocities $\check{v}$, $\check{w}$ are replaced in the computations by the velocities Ω_x, Ω_y, and Ω_z.

3.4 Computation of the viscous terms

In a finite volume approach, the computation of the viscous terms requires the evaluation of first-order derivatives at the cell faces. The computation of such gradients may be obtained using the Gauss theorem [37,35] but in this work a simpler procedure has been employed and the gradients were computed with

$$\frac{\partial q}{\partial \xi}_{i+\frac{1}{2}} = 2\frac{(q_{i+1} - q_i)\mathcal{S}_{i+\frac{1}{2}}}{\mathcal{V}_{i+1} + \mathcal{V}_i} \tag{25}$$

where $\mathcal{S}_{i+\frac{1}{2}}$ is the surface of the interface and $\mathcal{V}_i$, $\mathcal{V}_{i+1}$ are the volumes of the cells on both sides of the interface.

4 Implicit Operator

The implicit operator used to accelerate the convergence to the steady state is an extension to the three-dimensional case of the operator presented by Coakley [10]. It is derived from a backward Euler implicit integration of the equation (1). Instead of solving this operator by relaxation techniques as done in two dimensions by [27,49,30] and partially in three dimensions by [7], the three-dimensional implicit operator is dimensionally splitted [5] leading to the resolution of three one-dimensional operators of the form

$$(I + \Delta t \frac{\partial \check{A}}{\partial \xi} - \Delta t \frac{\partial M}{\partial \xi}\frac{\partial}{\partial \xi})\delta U = \text{RHS} \tag{26}$$

where $\check{A}$ is the jacobian matrix of the Euler flux in the direction ξ

$$\check{A} = \frac{\partial \check{F}}{\partial \xi} = \frac{\partial F}{\partial U} n_x + \frac{\partial G}{\partial U} n_y + \frac{\partial H}{\partial U} n_z$$

with

$$F = \mathbf{F}\vec{\imath};\ G = \mathbf{F}\vec{\jmath};\ H = \mathbf{F}\vec{k}$$

and M is the matrix of the viscous terms.

If the spatial derivatives of (26) are discretized with a three points stencil, the resolution of the system (26) necessitates the inversion of a bloc 5x5 tridiagonal matrix. Following Chaussee and Pulliam [9] the system can be "diagonalized" leading to the inversion of scalar tridiagonal systems. This is accomplished by replacing the matrix M by its spectral radius σI, using the decomposition, $\check{A} = T^{-1} \check{\Lambda} T$ and by taking the product $T^{-1}\check{\Lambda}$ out of the spatial derivative. Introducing the characteristic variables $\delta\check{U} = T\delta U$ and multiplying the equation (26) by the matrix T, the system to be solved is now,

$$(I + \Delta t\ \check{\Lambda}\frac{\partial}{\partial \xi} - \Delta t\ \sigma I \frac{\partial^2}{\partial \xi^2})\delta\check{U} = \text{RHS}. \tag{27}$$

The Coakley scheme is finally obtained if a first-order upwind approximation is used for the spatial derivatives of the convective terms and a centered approximation for the diffusion terms. It should be noted that whereas the matrix $\check{A}$ involves only the components of the normal vector $\vec{n}$, the matrices T^{-1}, T and thereafter $\delta\check{U}$ involve also the tangential vectors $\vec{l}$, $\vec{m}$. In consequence, while the original system requires only the knowledge of the normal vector $\vec{n}$, the "diagonalized" system necessitates also the definition of the tangential vectors $\vec{l}$, $\vec{m}$. As the normal vector $\vec{n}$ was calculated by taking the cross product $\vec{t_1} \times \vec{t_2}$ fig.(2), it seems natural to choose

$$\vec{l} = \frac{\vec{t_1}}{||\vec{t_1}||} \tag{28}$$

and

$$\vec{m} = \vec{n} \times \vec{l}. \tag{29}$$

Such a procedure however produces spurious crossflows for purely two-dimensional flows. In the simple case of a two-dimensional turbulent flow on a flate plate, the vectors $\vec{\jmath}$, $\vec{k}$ can be chosen as the tangential vectors if the mesh is cartesian, fig.(3). The contravariant velocities are then identical to the cartesian velocities,

$$\begin{aligned} \Delta\breve{u} &= \Delta u \\ \Delta\breve{v} &= \Delta v \\ \Delta\breve{w} &= \Delta w\,(=0) \end{aligned}$$

and the implicit system for the tangential velocities can be written as

$$\begin{aligned} \mathcal{L}[\delta v] &= [\Delta v] \\ \mathcal{L}[\delta w] &= [\Delta w] \end{aligned} \tag{30}$$

where

$$[\delta v] = [\delta v_1, \cdots, \delta v_{j-1}, \delta v_j, \delta v_{j+1}, \cdots, \delta v_J]^{\mathrm{T}}.$$

If the matrix $\mathcal{L}$ is not singular, no crossflow can be generated by the implicit operator.

With the procedure proposed for the computation of the tangential vectors $\vec{l}$ and $\vec{m}$, equations (28,29), the vectors will differ from $\vec{j}$, $\vec{k}$, there form will be

$$\begin{aligned} \vec{l}_j &= \alpha_j\vec{j} + \beta_j\vec{k} \\ \vec{m}_j &= \gamma_j\vec{j} + \delta_j\vec{k}. \end{aligned}$$

If these vectors are used for the definition of the contravariant velocities, the "diagonal" implicit system can be written as

$$\begin{aligned} \mathcal{L}[\delta\breve{v}] &= [\alpha][\Delta v] + [\beta][\Delta w] \\ \mathcal{L}[\delta\breve{w}] &= [\gamma][\Delta v] + [\delta][\Delta w] \end{aligned}$$

thus

$$\begin{aligned} [\delta\breve{v}] &= \mathcal{L}^{-1}[\alpha][\Delta v] + \mathcal{L}^{-1}[\beta][\Delta w] \\ [\delta\breve{w}] &= \mathcal{L}^{-1}[\gamma][\Delta v] + \mathcal{L}^{-1}[\delta][\Delta w]. \end{aligned} \tag{31}$$

The solution of the implicit operator will be independant to the choice of the tangential vectors if the tangential velocities satisfy,

$$\begin{aligned} [\delta\breve{v}] &= [\alpha][\delta v] + [\beta][\delta w] \\ [\delta\breve{w}] &= [\gamma][\delta v] + [\delta][\delta w]. \end{aligned} \tag{32}$$

Unfortunatly the relations (32) are not always fulfilled as it can be seen by replacing in (31) $[\Delta v]$ by $\mathcal{L}[\delta v]$ and $[\Delta w]$ by $\mathcal{L}[\delta w]$,

$$\begin{aligned} [\delta\breve{v}] &= \mathcal{L}^{-1}[\alpha]\mathcal{L}[\delta v] + \mathcal{L}^{-1}[\beta]\mathcal{L}[\delta w] \\ [\delta\breve{w}] &= \mathcal{L}^{-1}[\gamma]\mathcal{L}[\delta v] + \mathcal{L}^{-1}[\delta]\mathcal{L}[\delta w]. \end{aligned} \tag{33}$$

The expression (33) can be identical to (32) if and only if the matrix $\mathcal{L}$ commute with the diagonal matrices $[\alpha]$, $[\beta]$, $[\gamma]$, $[\delta]$. For general matrices $\mathcal{L}$, this necessitates that

$$\begin{aligned} [\alpha] &= \alpha I \\ [\beta] &= \beta I \\ [\gamma] &= \gamma I \\ [\delta] &= \delta I. \end{aligned} \tag{34}$$

In the case of the two-dimensional turbulent flow on the flate plate, because of the stretching of the mesh in the boundary layer, the relations (34) are far from being satisfied and as a consequence, a strong crossflow is generated, $\delta w \neq 0$. The "natural" procedure has therefore to be rejected.

The proposed method for the computation of the tangential velocities, follows the procedure used at the explicit step. The computation of the increments of the tangential velocity vectors $\delta\breve{v}$ and $\delta\breve{w}$ are replaced by the computation of linear combinations of them i.e.

$$\begin{aligned} \delta\Omega_x &= (l_x\delta\breve{v} + m_x\delta\breve{w}) &= \delta u - n_x\delta\breve{u} \\ \delta\Omega_y &= (l_y\delta\breve{v} + m_y\delta\breve{w}) &= \delta v - n_y\delta\breve{u} \\ \delta\Omega_z &= (l_z\delta\breve{v} + m_z\delta\breve{w}) &= \delta w - n_z\delta\breve{u}. \end{aligned} \tag{35}$$

Performing some linear combinations on the equations for $\delta\breve{v}$ and $\delta\breve{w}$, the equations (36) can be formed,

$$\delta\Omega_\theta + \breve{u}\Delta t\,(l_\theta\frac{\partial\delta\breve{v}}{\partial\xi} + m_\theta\frac{\partial\delta\breve{w}}{\partial\xi}) = \Delta\Omega_\theta\,; \quad \theta = x,\ y,\ z. \tag{36}$$

Finally the equations for $\delta\Omega_\theta$ are obtained if the coordinate components l_θ, m_θ are taken inside the spatial derivatives — this approximation is of the same order as the approximation used in the "diagonalization" — leading to

$$(I + \breve{u}\Delta t\frac{\partial}{\partial\xi})\delta\Omega_\theta = \Delta\Omega_\theta\,; \quad \theta = x,\ y,\ z. \tag{37}$$

Thus instead of solving the two equations for $\delta\breve{v}$ and $\delta\breve{w}$, the three equations for $\delta\Omega_x$, $\delta\Omega_y$ and $\delta\Omega_z$ will be solved. Of course, the three velocity components $\delta\Omega_\theta$ cannot be independant, they should satisfy

$$n_x\delta\Omega_x + n_y\delta\Omega_y + n_z\delta\Omega_z = 0. \tag{38}$$

Because of the simplification made for the transformation of (36), the equation (38) is generally not verified ; the tangential vector $\delta\vec{\Omega}$ does not lie in the tangential plane. Therefore it is replaced by its projection on the tangential plane $\delta\vec{\Omega}'$,

$$\delta\Omega'_\theta = \delta\Omega_\theta - n_\theta\delta \tag{39}$$

with

$$\delta = n_x\delta\Omega_x + n_y\delta\Omega_y + n_z\delta\Omega_z.$$

By construction no crossflow can be generated when this procedure is used for the computation of the implicit tangential incremental velocities. Numerical experiments have also shown that for purely two-dimensional flows, the three-dimensional operator leads to almost the same convergence rate than the corresponding two-dimensional operator.

5 Boundary Conditions

The use of upwind schemes simplifies significantly the computation at the boundaries as solely the "physical" boundary conditions are needed. For instance, if only simple waves are assumed at the boundaries, the Osher P variant scheme can be used at the boundaries by replacing the information contained in the waves outside of the computational domain by the natural physical boundary conditions [15] : static pressure at an outflow boundary; rest temperature, rest pressure and flow angle at an inflow; no slip velocity, zero normal pressure gradient and adiabaticity at a solid wall .... For lifting airfoils, the freestream conditions are modified by taking into account the circulation around the airfoil as discussed in [48]. The undisturbed flow conditions are used for flows around finite wings as the disturbances created by the wing decay more quickly in the three-dimensional case than in the two-dimensional one. If sufficiently far from the wing, they behave like those generated by a point singularity rather than by a line singularity.

At the implicit step all the boundary conditions are treated implicitly. For the characteristic variables $\delta\Omega_x$, $\delta\Omega_y$, $\delta\Omega_z$ and $a^2\delta\rho - \delta P$, if the index of the boundary is denoted by $N+1$, the equations at all type of boundaries can be cast into the form

$$\delta U_{N+1} = d_1 \delta U_N + d_2 \delta U_{N-1}. \tag{40}$$

with

$d_1 = d_2 = 0$ for a solid wall, a farfield boundary
$d_1 = \frac{3}{2}$, $d_2 = -\frac{1}{2}$ for an extrapolated boundary condition
$d_1 = 1$ or 0, $d_2 = 0$ for a symmetry condition
$\vdots$

If treated implicitly, the symmetry and wall boundary conditions introduce some coupling between the variables $\delta R^+ = \delta P + \rho a\, \delta\tilde{u}$ and $\delta R^- = \delta P - \rho a\, \delta\tilde{u}$. The implicit equations can therefore not completely be decoupled and a 2x2 block tridiagonal system has to be solved for these characteristic variables. The boundary conditions associated with this 2x2 system are the equivalent of (40)

$$\begin{bmatrix} \delta R^+ \\ \delta R^- \end{bmatrix}_{N+1} = \begin{bmatrix} d_1^+ & d_2^+ \\ d_1^- & d_2^- \end{bmatrix} \begin{bmatrix} \delta R^+ \\ \delta R^- \end{bmatrix}_N + \begin{bmatrix} d_3^+ & 0 \\ 0 & d_3^- \end{bmatrix} \begin{bmatrix} \delta R^+ \\ \delta R^- \end{bmatrix}_{N-1} \tag{41}$$

with

$d_{1,2,3}^{\pm} = 0$ for a farfield
$d_1^{\pm} = d_2^{\pm} = \frac{1}{2}$, $d_3^{\pm} = 0$ at a wall and a symmetry plane
$d_1^+ = d_2^- = \frac{3}{2}$, $d_2^+ = d_1^- = 0$, $d_3^{\pm} = -\frac{1}{2}$ for an extrapolated boundary condition
$\vdots$

As the same functional form (40) or (41) is used at all type of boundaries, the computation of implicit boundary conditions does not impaired the vectorizability of the implicit step.

6 Turbulence Modeling

Two simple mixing length turbulence models were examined in this work. The first model considered is the standard Baldwin-Lomax model [4]

$$\begin{aligned} \nu_{ti} &= \rho K^2 \eta^2 D^2 |\omega|; \quad K = 0.4 \\ \nu_{to} &= 1.6\, \mathrm{F}_w \mathrm{Fkleb}(\eta) \\ \nu_t &= \min(\nu_{ti}, \nu_{to}) \end{aligned} \tag{42}$$

where

$$\begin{aligned} D &= 1 - \exp(-\frac{\eta^+}{26}) \\ \eta^+ &= \frac{u_\tau \eta}{\nu}; \quad u_\tau = \max\sqrt{\nu\omega} \\ \mathrm{F}_w &= \min\left[\eta_{\mathrm{max}} \mathrm{F}_{\mathrm{max}}, \frac{\eta_{\mathrm{max}}(|\breve{u}|_{\mathrm{max}} - |\breve{u}|_{\mathrm{min}})^2}{\mathrm{F}_{\mathrm{max}}}\right] \\ \mathrm{F}_{\mathrm{max}} &= \max_j(F(\eta))_{i,j,k}\ ; \quad F(\eta_{\mathrm{max}}) = \mathrm{F}_{\mathrm{max}} \\ F(\eta) &= \eta|\omega|D \\ \mathrm{Fkleb} &= 0.0168\left[1 + 5.5(\frac{0.3\eta}{\eta_{\mathrm{max}}})^6\right]^{-1} \end{aligned}$$

The definition of u_τ was chosen slightly different from the wall shear stress as used in the original Baldwin-Lomax turbulence model. This modification was introduced in order to prevent from the computation of a vanishing eddy viscosity in a section emanating from a saddle separation point ($|\omega|_{\mathrm{W}} = 0$).

It is well known that equilibrium models such as the Baldwin-Lomax model, are not suited for separated flows for which the diffusion and the convection of the turbulence are no more negligible and introduce some imbalance between the production and the dissipation rate of turbulence. While retaining the eddy viscosity assumption these non equilibrium effects can be taken into account by two-equation models, $K - \epsilon$, $K - \omega$, but it seems that despite their "universality" the two-equation models does not improve significantly the agreement between the computed results and the experimental data for separated flows [11]. A less ambitious approach is to modify two-layers mixing length models in order to extend their successes to separated flows. Such an approach was taken by Johnson and King [25] and the model they derived, appeared to be adequate for the computation of separated flows on airfoils and wings [11] [2].

The idea behind the Johnson-King model is (i) to scale the turbulent velocity to the square root of the maximum Reynolds shear stress rather than to a length scale wall vorticity product; (ii) to compute the maximum Reynolds shear stress by solving a differential equation in which non-equilibrium effects are taken into account. As the level of the turbulent shear stress is then determined by the differential equation, the Johnson-King model in contrary to standard mixing length models, neither depends only on local mean flow gradients nor assumed a turbulence in equilibrium. The eddy viscosity distribution in the inner layer used with the Johnson-King model is then

$$\nu_{ti} = K\eta D^2 u_M \tag{43}$$

where

$$\begin{aligned}
u_M &= (\frac{\tau_M}{\rho})^{\frac{1}{2}} \\
D &= 1 - \exp(-\frac{\eta^+}{17}) \\
\eta^+ &= \frac{\eta \max(u_M, u_\tau)}{\nu}.
\end{aligned}$$

Here and below the index $_M$ indicates the location where the Reynolds shear stress is maximum.

In the original formulation of Johnson and King the outer eddy viscosity layer was based on the Cebeci-Smith distribution. This formulation was well suited in the boundary-layer context used by Johnson and King for the derivation of their model, but with Navier-Stokes codes the Baldwin-Lomax formulation is more convenient. The outer eddy viscosity layer is therefore calculated using

$$\nu_{to} = \sigma 1.6 \, \mathrm{F}_w \mathrm{Fk} \tag{44}$$

with

$$\begin{aligned}
\delta &= 1.9 \, \eta_{\max} \\
\mathrm{Fk} &= 0.0168 \left[1 + 5.5(\tfrac{\eta}{\delta})^6\right]^{-1}.
\end{aligned}$$

The coefficient σ is introduced to force the value of the maximum shear stress $\tilde{\tau}_M = \mu_t|\omega|$, to match the value τ_M obtained by the resolution of the differential equation (48). This coefficient can be computed by solving the equation

$$\tilde{\tau}_M(\sigma) - \tau_M = 0 \tag{45}$$

with a Newton method, or with a procedure proposed by Abid [1],

$$\begin{aligned}
\sigma^{t+\Delta t} &= \sigma^t \frac{\tau_M}{\tilde{\tau}_M(\sigma^t)} \\
\sigma^0 &= 1.
\end{aligned} \tag{46}$$

Knowing the values of ν_{ti} and ν_{to}, the actual value of the turbulent eddy viscosity ν_t is computed with

$$\nu_t = \nu_{to}(1 - \exp(-\frac{\nu_{ti}}{\nu_{to}})). \tag{47}$$

As stated, the level of the turbulent shear stress is obtained through the resolution of a differential equation, see [25] for its derivation. In the three-dimensional case, this equation is

$$\breve{u}_M \frac{\partial}{\partial \xi}(\frac{\tau_M}{\rho})^{-\frac{1}{2}} + \breve{w}_M \frac{\partial}{\partial \zeta}(\frac{\tau_M}{\rho})^{-\frac{1}{2}} = \frac{0.125}{L_M}\left[(1 - (\frac{\tau_M}{\tau_{\mathrm{eq}}})^{-\frac{1}{2}}) + \frac{2L_M}{\delta(0.7 - \frac{\eta}{\delta})}\sqrt{(1 - \sigma^{\frac{1}{2}})^+}\right] \tag{48}$$

with

$$L_M = \min(K\eta_M, 0.225K\delta).$$

The left hand side of (48) represents the convection of the turbulent shear stress. The diffusion of the turbulent shear stress being modeled by the last term of the right hand side, the remaining term corresponds then to the imbalance between the production and dissipation of turbulence. This term is consequently approximated by the difference between the actual shear stress and the shear stress that would have been obtained if the turbulence was in equilibrium. This shear stress, τ_{eq}, is computed at $\eta = \eta_M$ using

$$\begin{aligned}
\tau_{\mathrm{eq}} &= \mu_{t\,\mathrm{eq}}|\omega| \\
\nu_{t\,\mathrm{eq}} &= \nu_{to\,\mathrm{eq}}\left(1 - \exp(-\frac{\nu_{ti\,\mathrm{eq}}}{\nu_{to\,\mathrm{eq}}})\right) \\
\nu_{ti\,\mathrm{eq}} &= K\eta D^2 u_{\mathrm{eq}} \\
\nu_{to\,\mathrm{eq}} &= 1.6\,\mathrm{F}_w\mathrm{Fk}
\end{aligned} \qquad (49)$$

with

$$\begin{aligned}
D &= 1 - \exp(-\frac{\eta\, u_{\mathrm{eq}}}{17\nu}) \\
u_{\mathrm{eq}} &= \max(\nu_{t\,\mathrm{eq}}|\omega|, \nu|\omega|).
\end{aligned}$$

The convection terms of (48) are approximate by first-order upwind differences. The equation is then solved with a Point Alternate Symmetric Gauss-Seidel Relaxation with one relaxation performed in each direction. An alternative approach used in [39] and [2], is to add a time dependent term and to solve the equation in the same way as the Navier-Stokes equations (1).

7 Results and Discussions

The newly developed code was first validated on two-dimensional airfoils and the influence of the different choices of Riemann solvers and reconstruction schemes was studied. For instance the influence of the Riemann solver on the solution was studied on the CAST10 airfoil at $M_\infty = .767$, $\alpha = 2.159$, $\mathrm{Re} = 1 \times 10^7$. Under these conditions the shock is strong enough to induce a separation of the boundary layer. As it can be seen from figures (4-6), the results obtained with the Roe and Osher schemes are almost identical for this sensitive test case, even on coarse meshes. In particular the rapid acceleration at the leading edge is well predicted. The difference in the shock location between the experiments of [34] and the computations, can be due to the extreme sensitivity of this airfoil to wind tunnel side-wall effects [33], or are due to the Baldwin-Lomax turbulence model employed in the computations, model which is not adequate for separated flows. A clear improvement in the shock location was obtained with the Johnson-King model, fig.(7). Not only the computed pressure distributions on the airfoil, obtained with the different approximate Riemann solvers are the same, but the whole flowfields look alike fig.(8-10).

The numerical procedure shows a larger sensitivity to the reconstruction schemes than to the Riemann solvers. On both the CAST10 and the RAE2822 airfoils, the inherent numerical viscosity of the second-order ENO scheme induces some significant differences, at the leading edge and on the upper surface of the airfoils, between the computed pressure distribution and the experiments of Mineck [34] and Cook et al. [12], fig.(11, 12). A better agreement with the experimental data and a solution closer to the fine grid solution was obtained if the third-order κ scheme with the Chakravarthy- Osher limiter is used, fig.(4,13). It can be noticed however, that the pressure distribution on the lower surface of the airfoil is better predicted with the uniformly second-order scheme than with the TVD scheme which becomes a first-order scheme at extrema. Comparing the result obtained with the unlimited third-order scheme, fig.(14), and with the TVD scheme, it is clear that the limiter is active not only near the shock but also on the lower surface and near the leading edge.

In order to establish the optimal method, the computing time and the convergence histories of the different approximate Riemann solvers have to be compared. From table (1) it is clear that the Roe scheme is less expensive per iteration than the Osher scheme. The convergence histories have also to be examined as it has been found [41], that the Roe scheme induces some oscillations for slowly moving shocks whereas the Osher scheme does not generate such oscillations. As the shock approaches its final location, a slow moving shock is likely to appear. Therefore, if the oscillations are not damped efficiently, the convergence may slow down. This behavior has not been observed and even the convergence with the Roe scheme was found to be slightly better, fig.(15-17). Thus, as the third-order scheme with the Chakravarthy-Osher limiter, not only is more accurate than the second-order ENO scheme but is also less expensive, table(2), the optimal choice is clearly to combine the Roe scheme with the third-order κ scheme.

As already observed [32], the limiters have usually an adverse effect on the convergence rates of the scheme. This undesirable property can be illustrated by comparing on the RAE2822 airfoil at $M_\infty = .676$, $\alpha = 1.93$, $\text{Re} = 5.7 \times 10^6$ (case 1), the convergence history of the limited scheme with that of the unlimited one, fig.(18-19). The results indicate that even if the flow does not present any shock, the limiter is active and the non-smoothness of the limiting function creates some strong non-linearities which are responsible of the deterioration of the convergence history. It has been shown [55], that even with a differentiable limiter $\Phi(r)$, where r is the ratio of the successive gradients, the problem remains. The reason lies in the behavior of r which is like a random function in the farfield, where the gradients are very smalls. The cure in this case is to use a cutoff value under which the gradients are not limited, as described in [51]. It can be noted, that although only a two order of magnitude decay of the residual is obtained with the limiter turned on, the solution itself is almost identical to the unlimited one and agrees well with the experimental results, fig.(20-21). Therefore a convergence to the level of the truncation error can be suspected. It was found by numerical experiments, that a faster convergence is obtained when higher CFL numbers are combined with an under-relaxation of the increments. This behavior is illustrated by comparing the figures (19) and (22). In both cases near optimal CFL numbers were used.

If the solution contains a shock, the unlimited third-order scheme does not lead to a smooth solution, fig.(23). The non-smoothness of the solution has also an adverse effect on the convergence, fig.(24). In such case, a smooth solution without limiter can be obtained if the fully upwind scheme ($\kappa = -1$) is used, fig.(25). This value of κ leads to a much better convergence history as well, fig.(26). With the limited scheme, a limit cycle was again obtained, figures (27-29). It is interesting to note that the level of the residual increases with increasing CFL numbers. With higher CFL numbers, the lift reaches its mean value more rapidly but noticeable fluctuations around the mean value become more and more apparent. When highly non-linear schemes are used to compute steady solutions, one should therefore ensure that the residual has effectively been reduced below the level of the truncation error.

The convergence problems found with the Chakravarthy-Osher limiter can be elimitated on the RAE2822 airfoil, if the limiter is replaced by the "smooth limiter" described above. A convergence to the machine zero is then obtained on coarse and fine grids, fig.(30). It can be noted that the convergence rates of the scheme with the "smooth limiter" and of the unlimited scheme are alike; they even are almost independant to the grid density, fig.(30, 31). If the convergence properties of the "smooth limiter" and of the unlimited scheme are similar, the solutions calculated with the "smooth limiter" are more accurate than the solutions obtained with the unlimited scheme. Examining the figures (32, 33), it is clear that the solutions computed with the "smooth limiter" do not present any oscillation. Comparing on the RAE2822 airfoil the pressure distributions on the coarse grid, it appears that the accuracy of the scheme with the "smooth limiter" lies between the accuracy of the unlimited second-order scheme and the accuracy of the third-order scheme —with and without the Chakravarthy-Osher limiter— fig.(32). The pressure distribution with the "smooth limiter" for instance presents an overshoot at the leading edge whereas the third-order scheme does not show any overshoot. This overshoot is however more pronounced with the fully upwind scheme. Similar results are obtained for the pressure distribution on the upper surface; the pressure level is better predicted with the "smooth limiter" than with the fully upwind scheme but the shock location and the pressure peak near the leading edge, are not as well predicted with the "smooth limiter" as with the third-order scheme. These results could have been expected as the value $\tilde{\kappa}$ is a blending of the value $\kappa = -1$ (fully upwind) and $\kappa = \frac{1}{3}$ (third-order). It is interesting to note that in contrast to the Chakravarthy-Osher limiter, the "smooth limiter" does not smear the extremum on the under surface of the airfoil. Thus, even if the goal consisting of limiting the gradients only in the vicinity of the shocks, has not been fully achieved, significant improvements were obtained. The excessive dissipation introduced at the leading edge is a consequence of the lack of resolution in this region. As the mesh is refined, the results become more and more alike, fig.(33). A closer inspection on the skin friction coefficient shows however, that the fully upwind scheme introduces more dissipation at the trailing edge than both the third-order scheme with the Chakravarthy-Osher limiter and the "smooth limiter". On the skin friction coefficient, the shock appeared also to be better captured with the "smooth limiter" than with the fully unlimited upwind scheme. From these experiments one can consider that the third-order scheme with the Chakravarthy-Osher limiter is the most accurate scheme used, but the κ scheme with the "smooth limiter" while maintaining most of the accuracy of the third-order scheme, improves drastically the convergence of the scheme.

The "smooth limiter" was also applied to the computation of the flowfield around the same RAE2822 airfoil but with different flow conditions, $M_\infty = .75$, $\alpha = 2.81$, Re$=6.5 \times 10^6$ (case 10). Under these conditions a shock induced separation forms on the upper surface of the airfoil. With the Baldwin-Lomax turbulence model, a wrong shock location is again obtained fig.(34) but no oscillations are created and the "smooth limiter" does not produce too much dissipation at the trailing edge of the airfoil, fig.(34). In this case also, a machine accuracy convergence was reached, fig.(35). On the ONERA M6 wing $M_\infty = .84$, $\alpha = 3.06$, Re $= 11 \times 10^6$, the "smooth limiter" improves the convergence of the method when compared to the Chakravarthy-Osher limiter, but the convergence rate is not as good as that of the unlimited fully upwind scheme, fig.(36). Examining the solution, fig.(37), it is apparent that the results calculated with the "smooth limiter" are in a large part of the wing, close to the results obtained with the Chakravarthy-Osher limiter. While resolving slightly better the leading edge pressure peak, the unlimited scheme smears much more the shock. Near the tip of the wing, $\frac{2y}{B} \geq 0.9$, the "smooth limiter" introduces an additional extremum. This new extremum is probably responsible of the slowdown of the convergence as compared to the unlimited scheme. It is the author belief, that if the limiter is designed correctly, the convergence with the limited scheme should be as good as the convergence obtained with the unlimited scheme. The behavior of the scheme with the "smooth limiter" on the coarse grid indicates that something was not done properly. This indication has been confirmed by the difficulties encounted on a finer mesh with the "smooth limiter". In conclusion, the "smooth limiter" improves significantly the convergence of the method on the RAE2822 airfoil, but it is still not the "Ultimate" limiter and modifications have to be made in order to obtain a broader range of its applicability.

The influence of the turbulence modeling has finally been studied. For attached flows on airfoils, we have seen fig.(18,33) that a good agreement with the experimental data can be obtained with the Baldwin-Lomax turbulence model. The same is true for the attached flow on the ONERA M6 wing $M_\infty = .84$, $\alpha = 3.06$, $\mathrm{Re} = 11 \times 10^6$, if the grid is fine enough, fig.(38). For separated flows, (RAE2822 case 10), the Baldwin-Lomax model predicts a shock location which is far downstream of the location observed experimentally, fig.(39). No improvements are found by refining the mesh. It can be noted once again, that the third-order scheme combined with the Chakravarthy-Osher limiter gives fairly accurate results on coarse grids. If the equilibrium model does not predict the proper shock location, with the non-equilibrium model of Johnson and King, the correct shock location is found, fig.(40). Comparing the grid refinement study made with the Baldwin-Lomax model and with the Johnson-King model, the greater sensitivity of the Johnson-King model clearly appears. A noticeable difference in the shock location is observed whether a 161x33 or a 257x65 mesh is used. Futhermore, the Johnson-King model is particulary sensitive to the initial level of the maximum shear stress. For instance the "solution" (unsteady) shown in figure (41) was obtained in the following manner : the Reynolds equations with the Baldwin-Lomax model were first solved on a 81x17 mesh; this solution was then interpolated on the 161x33 mesh and serves as the initial condition for this finer mesh; fifty iterations were then performed on the 161x33 mesh with the Baldwin-Lomax model before the original Johnson-King model was turned on. If more iterations had been performed on the 161x33 mesh with the Baldwin-Lomax model, steady but wrong solutions would have been obtained as well. The solution shown in figure (40a) was computed by taking as the initial condition, the converged solution obtained with the Baldwin-Lomax model on the 161x33 mesh. In order to enforce a unique solution — independant of the initial condition — the velocity scale used in the inner layer of the equilibrium eddy viscosity, $\nu_{ti\,\mathrm{eq}}$, has to be replaced. Instead of using

$$u_{\mathrm{eq}} = \nu_{t\,\mathrm{eq}} |\omega|$$

as in the original Johnson-King model,

$$u_{\mathrm{eq}} = \max(\nu_{t\,\mathrm{eq}} |\omega|,\ \nu |\omega|)$$

must be employed. This fix was yet not sufficient in the computation of the ONERA M6 wing shown below. The level of the starting maximun shear stress was in this case still to low and in consequence, the shock location was moving upstream without any bound. The fix was then to replace in the computation of $\nu_{ti\,\mathrm{eq}}$, the inner layer formulation of Johnson and King by the Baldwin and Lomax formulation,

$$\nu_{ti\,\mathrm{eq}} = K^2 \eta^2 D^2 |\omega|.$$

With the Baldwin-Lomax formulation for $\nu_{ti\,\mathrm{eq}}$, a better solution was found on the RAE2822 (case 10) airfoil on a coarse grid, fig.(42), but on a finer grid, the pressure recovery was unfortunately not predicted as well as with the "original" formulation; a pressure bump is found, fig.(43). This bump has also been observed by Radespiel [39] and Swanson [46], with a Jameson type scheme and with the "original" formulation of Johnson and King. The extreme sensitivity of the Johnson-King model shows up also on the convergence of the method. From figure (44), it is apparent that the lift converges with difficulties, the clear decay of the oscillations indicates nevertheless that if enough iterations are performed, a steady solution can be expected. It should also be pointed that the computation of σ proposed by Abid, equation (46), introduces some time dependency in the solution. The steady state will slightly depend on the time integration path and depending whether the turbulence quantities were updated at every iterations or only at every five iterations, different convergence histories were found.

As already noticed by Coakley [11], we also observed that whereas the Johnson-King model improves significantly the prediction of separated flows, attached flows are not as well resolved with the non-equilibrium model as with the Baldwin-Lomax model, fig.(45). The reason again lies in the inner layer eddy viscosity formulation of Johnson and King. Recently, Johnson and Coakley [24] proposed a new formulation which consists of a non-linear blending of the Johnson-King and Baldwin-Lomax formulations. This new law seems to ameliorate the results but the added non-linearity increases also the convergence problems.

The behaviors of the Johnson-King model observed in two dimensions were confirmed in three dimensions. The test case used is the ONERA M6 wing, where comparisons with both detailed experiments [45] and numerical results [2] [39] are possible. For an angle of attack of $\alpha = 6.06$, a large separation region forms on the upper surface of the wing, fig.(46). In this case the Baldwin-Lomax model is again inadequate to capture the main feature of the flow. The pressure plateau after the interaction of the two shocks — the shock emanating from the leading edge and the normal shock, fig.(47)— is for instance not captured at all and this disagreement with the experimental data is not due to a lack of resolution, fig.(48). As pressure plateau regions behind a shock wave are usually the result of a large reverse flow region, a non-equilibrium model must be used in order to obtain a good resolution of the pressure distribution. With the non-equilibrium model of the Johnson and King, it is clear that a good representation of this pressure distribution is obtained, fig.(49) and the expected large reverse flow region is effectively found, fig.(50). These results are the consequence of the lower values of eddy viscosity predicted by the Johnson-King model in adverse pressure gradient regions. The lower values of eddy viscosity also induce an upstream movement of the shock location, fig.(51). No experimental visualizations of the wall streamlines were available on the ONERA M6 wing, but the computed, mushroom type, wall streamlines are in good agreement with the results obtained by Abid, Vatsa et al. [2]. The mushroom type structures were also observed experimentally on other wings [26]. If the Baldwin-Lomax formulation for $\nu_{ti_{\rm eq}}$ is used, computation on coarse grids with the Johnson-King model were possible and satisfactory results found, fig.(52-54); even the wall streamlines patern was qualitatively well predicted, fig.(54). For an attached flow case, $\alpha = 3.06$, the Johnson-King model predicts a shock location which is as in the two-dimensional case, slightly upstream of the position obtained with the Baldwin-Lomax model. The difference however seems to be less pronounced in the three-dimensional case than in the two-dimensional one, fig.(55,56).

8 Conclusion

Two and three-dimensional computations have been presented and differences between several upwind schemes discussed. It has been found that the differences due to the upwind schemes are negligible if the three waves existing in the Euler equations are taken into account by a Riemann solver. The reconstruction scheme was found to have more influence on the accuracy of the solution. Accurate solutions on coarse meshes were obtained with a third-order upwind biased scheme. Such scheme requires the use of some limiter in order to compute smooth solutions with shocks. If the use of limiters leads to robust schemes, it has the drawback of preventing a convergence to the machine accuracy. It was proven that the use of a “smooth limiter” can drastically improve the convergence of the method. The “smooth limiter” proposed, while leading to good convergence rates on the RAE2822 airfoil, presents still some defects on the ONERA M6 wing. Thus modifications on the limiter need to be done to enlarge its applicability.

Equilibrium and non-equilibrium mixing length type turbulence model were tested on two and three-dimensional configurations. While the equilibrium model was found to give accurate results for attached boundary layer type flows, it was also proven to be inadequate to predict correctly separated flows. Inversly, the solutions obtained with a modified version of the Johnson-King model agree well with experimental data for separated flows, but are less accurate than the solutions computed with the Baldwin-Lomax model for attached flows. Futhermore, an excessive sensitivity of the non-equilibrium model was experienced. Therefore some changes in the non-equilibrium model in order to improve the accuracy of the solutions for attached flows *and* to reduce the sensitivity of the model, have to be made before it can be used routinely in engineering computations.

Acknowledgement

This report describes the one year work performed by the author while in residence at the NASA Langley Research Center as a National Research Council associate. The author is much obliged to Doctors B. Wedan for providing all the three-dimensional grids, R. Abid for his aide in the implementation of the Johnson-King model, R. C. Swanson and V. Vatsa for the numerous discussions concerning the computations. The support throughout this year of M. D. Salas is also gratefully acknowledged.

References

[1] R. Abid. Extension of the Johnson-King turbulence model to the 3-D flows. *AIAA Paper*, 88-0223, 1988.

[2] R. Abid, V. N. Vatsa, D.A. Johnson, and B.W. Wedan. Prediction of separated transonic wing flows with a non-equilibrium algebraic model. *AIAA Paper*, 89-0558, 1989.

[3] W. K. Anderson. *Implicit Multigrid Algorithms for the Three-Dimensional Flux Split Euler Equations.* PhD thesis, Mississippi State University, 1986.

[4] B. Baldwin and H. Lomax. Thin-layer approximation and algebraic model for separated turbulent flows. *AIAA Paper*, 78-257, 1978.

[5] R. M. Beam and R. F. Warming. An implicit finite-difference algorithm for hyperbolic systems in conservation law form. *Journal of Computational Physics*, 22:87–110, 1976.

[6] S. Chakravarthy and S. Osher. A new class of high accuracy TVD schemes for hyperbolic conservation laws. *AIAA Paper*, 85-0363, 1985.

[7] S. R. Chakravarthy. High resolution upwind formulations for the Navier-Stokes equations. *VKI-LS*, 1988-05, 1988.

[8] S. R. Chakravarthy. Relaxation methods for unfactored implicit upwind schemes. *AIAA Paper*, 84-0165, 1984.

[9] D. S. Chaussee and T. H. Pulliam. A diagonal form of an implicit approximate factorization algorithm with application to a two dimensional inlet. *AIAA Paper*, 80-0067, 1980.

[10] T. J. Coakley. Implicit upwind methods for the compressible Navier-Stokes equations. *AIAA Paper*, 83-1958, 1983.

[11] T. J. Coakley. Numerical simulation of viscous transonic airfoil flows. *AIAA Paper*, 87-0416, 1987.

[12] P. H. Cook, M. A. McDonald, and M. C. P. Firmin. Aerofoil RAE 2822 - pressure distributions and boundary layer and wake measurements. *AGARD-AR*, 138, 1979.

[13] S. Davis. A rotationally biased upwind difference scheme for the Euler equations. *Journal of Computational Physics*, 56:65–92, 1984.

[14] H. Deconinck, C. Hirsch, and J. Peuteman. Characteristic decomposition methods for the multidimensional Euler equations. In *10th International Conference on Numerical Methods in Fluid Dynamics*, Beijing, 1986.

[15] F. Dubois. *Boundary Conditions and the Osher scheme for the Euler Equations of Gas Dynamics.* Technical Report 170, Ecole Polytechnique, 1987.

[16] S. K. Godunov. Finite difference methods for numerical computations of discontinuous solutions of equations of fluid dynamics. *Math. Sbornik.*, 47:271–295, 1959.

[17] A. Harten. High resolution schemes for hyperbolic conservation laws. *Journal of Computational Physics*, 49:357–393, 1983.

[18] A. Harten, B. Engquist, S. Osher, and S. R. Chakravarthy. Some results on uniformly high-order accurate essentially non-oscillatory schemes. *ICASE Report*, 86-18:347–377, 1986.

[19] A. Harten and S. Osher. Uniformly high-order accurate non-oscillatory schemes I. *SIAM J. Numer. Anal.*, 24:279–309, 1987.

[20] P. W. Hemker and S. P. Spekreijse. Multigrid solution of the steady Euler equations. In *Oberwolfach Meeting on Multigrid Methods*, 1984.

[21] A. Jameson. *Multigrid Algorithms for Compressible Flow Calculations.* Technical Report, MAE Report 1743, Text of lecture given at the 2nd European Conference of Multigrid Methods, 1985.

[22] A. Jameson, T. J. Baker, and N. P. Weatherill. Calculation of inviscid transonic flow over a complete aircraft. *AIAA Paper*, 86-0103, 1986.

[23] A. Jameson, W. Schmidt, and E. Turkel. Numerical solution of the Euler equation by finite-volume methods using Runge-Kutta time-stepping. *AIAA Paper*, 81-1259, 81.

[24] D. A. Johnson and T. J. Coakley. Improvements to a nonequilibrium algebraic turbulence model. *AIAA Journal*, to be published, 1989.

[25] D. A. Johnson and L. S. King. A mathematically simple turbulence closure model for attached and separated turbulent boundary layers. *AIAA Journal*, 23:1684–1692, 1985.

[26] W. K. Lockman and H. L. Seegmiller. An experimental investigation of the subcritical and supercritical flow about a swept semispan wing. *NASA Technical Memorandum* 84376, 1983.

[27] R. W. Mac Cormack. Current status of numerical solutions of the Navier-Stokes equations. *AIAA Paper*, 85-0032, 1985.

[28] L. Martinelli. *Calculation of Viscous Flows with Multigrid Methods.* PhD thesis, Princeton University, 1987.

[29] Y. Marx. *Etude d'Algorithmes pour les Equations de Navier-Stokes Compressible.* PhD thesis, University of Nantes, 1987.

[30] Y. Marx and J. Piquet. Comparison of implicit methods for the compressible Navier-Stokes equations. In K. W. Morton and Baines M. J., editors, *Numerical Methods for Fluid Dynamics III*, pages 282–288, ICFD Oxford, Clarendon Press, Oxford, 1988.

[31] Y. Marx and J. Piquet. Towards multigrid acceleration of 2D compressible Navier-Stokes finite volume implicit schemes. In W. Hackbusch, editor, *Robust Multi-Grid Methods*, pages 178–187, 4th GAMM Seminar, Vieweg Verlag, Notes on Numerical Fluid Mechanics, Volume 23, 1988.

[32] Y. Marx and J. Piquet. Two-dimensional compressible Navier-Stokes finite volume computations by means of implicit schemes. *Int. Journ. for Num. Meth. in Fluids*, 8:1195–1202, 1988.

[33] Y. P. Marx. Computation of turbulent flow on a CAST 10 wing using an upwind scheme. *AIAA Paper*, 89-1836, 1989.

[34] R. E. Mineck. Wall interference tests of a CAST 10-2/DoA 2 airfoil in an adaptive-wall test section. *NASA Technical Memorandum* 4015, 1987.

[35] B. Müller and A. Rizzi. Runge-Kutta finite volume simulation of laminar transonic flow over a NACA 0012 airfoil using the Navier-Stokes equations. *FFA TN*, 1986-60, 1986.

[36] S. Osher. Shock modeling in aeronautics. In K. W. Morton and M. J. Baines, editors, *Numerical Methods for Fluid Dynamics*, pages 179–217, Academic Press, 1982.

[37] R. Peyret and T. D. Taylor. *Computational Methods for Fluid Flow.* Springer-Verlag, 1983.

[38] K. G. Powell and B. Van Leer. A genuinely multi-dimensional upwind cell-vertex scheme for the Euler equations. *AIAA Paper*, 89-0095, 1989.

[39] R. Radespiel. A cell-vertex multigrid method for the Navier-Stokes equations. *NASA Technical Memorandum* 101557, 1989.

[40] R. Radespiel, C. Rossow, and R. C. Swanson. An efficient cell-vertex multigrid scheme for the three-dimensional Navier-Stokes equations. *AIAA Paper*, 89-1953-CP, 1989.

[41] T. W. Roberts. The behavior of flux difference splitting schemes near slowly moving shock waves. *FFA TN*, 1988-58, 1988.

[42] P. L. Roe. Approximate Riemann solvers, parameter vectors, and difference schemes. *Journal of Computational Physics*, 43:357–372, 1981.

[43] P. L. Roe. Discrete models for the numerical analysis of time-dependent multidimensional gas dynamics. *ICASE Rept 172574 also in Journal of Computational Physics (87)*, 1985.

[44] P. L. Roe and J. Pike. Efficient construction and utilisation of approximate Riemann solutions. In R. Glowinski and J.-L. Lions, editors, *Computing Methods in Applied Sciences and Engineering*, pages 499–518, Amsterdam North-Holland, 1984.

[45] V. Schmitt and F. Charpin. Pressure distributions on the ONERA-M6 wing at transonic mach numbers. *AGARD-AR*, 138, 1979.

[46] R. C. Swanson. Personal communication. 1989.

[47] P. K. Sweby. High resolution schemes using flux limiters for hyperbolic conservation laws. *SIAM J. Numer. Anal.*, 21:995–1011, 1984.

[48] J. L. Thomas and M. D. Salas. Far-field boundary conditions for transonic lifting solutions to the Euler equations. *AIAA Paper*, 85-0020, 1985.

[49] J. L. Thomas, B. Van Leer, and R. W. Walters. Implicit flux-split schemes for the Euler equations. *AIAA Paper*, 85-1680, 1985.

[50] J. L. Thomas, R. W. Walters, T. Reu, F. Ghaffari, R. P. Weston, and J. M. Luckring. A patched-grid algorithm for complex configurations directed towards the F/A-18 aircraft. *AIAA Paper*, 89-0121, 1989.

[51] G. D. Van Albada, B. Van Leer, and W. W. Roberts. A comparative study of computational methods in cosmic gas dynamics. *ICASE Report*, 81-24, 1981.

[52] B. Van Leer. Towards the ultimate conservative difference scheme II. monotonicity and conservation combined in a second-order scheme. *Journal of Computational Physics*, 14:361–370, 1974.

[53] B. Van Leer. Towards the ultimate conservative difference scheme IV. a new approach to numerical convection. *Journal of Computational Physics*, 23:276–298, 1977.

[54] V. N. Vatsa and B. W. Wedan. Development of an efficient multigrid code for 3-D Navier-Stokes equations. *AIAA Paper*, 89-1791, 1989.

[55] V. Venkatakrishnan and T. J. Barth. Application of direct solvers to unstructured meshes for the Euler and Navier-Stokes equations using upwind schemes. *AIAA Paper*, 89-0364, 1989.

Figures and Tables

	Cpu μs	ratio
Roe	1.8	1
Osher P	4.8	2.67
Osher O	5.4	3

Table 1: Computing times (CRAY2); Riemann Solvers

	Cpu μs	ratio
Chakravarthy-Osher	1.25	1
Harten-Osher	1.75	1.4

Table 2: Computing times (CRAY2); Reconstruction Schemes

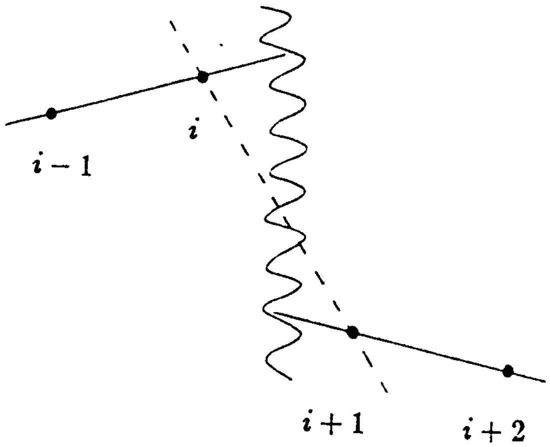

Figure 1: Gradients near a shock

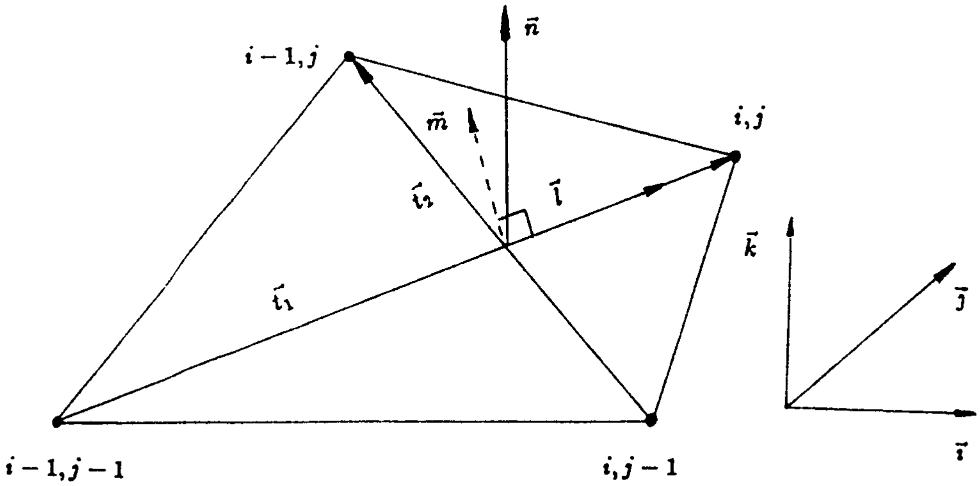

Figure 2: Definition of the cell face reference frame

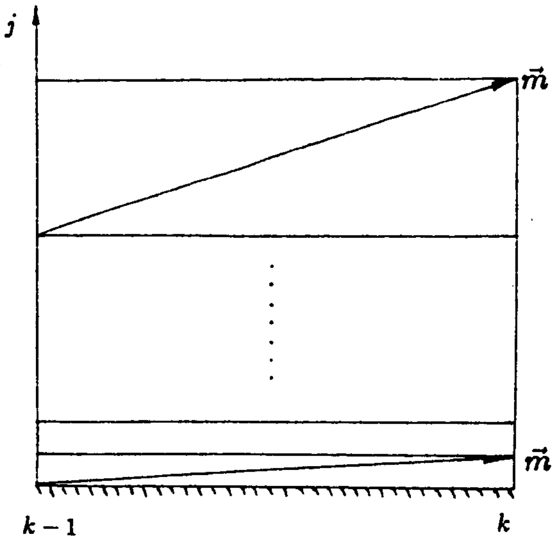

Figure 3: Evolution of the tangential vector $\vec{m}$ in the boundary layer

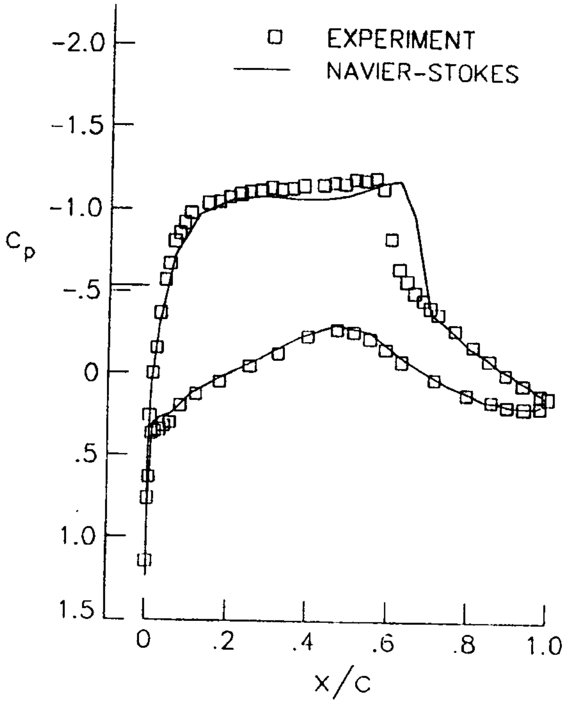

Figure 4:
Pressure distribution
Osher O scheme, $\kappa = \frac{1}{3}$
Chakravarthy-Osher limiter
81x17 mesh (48 points on the airfoil)

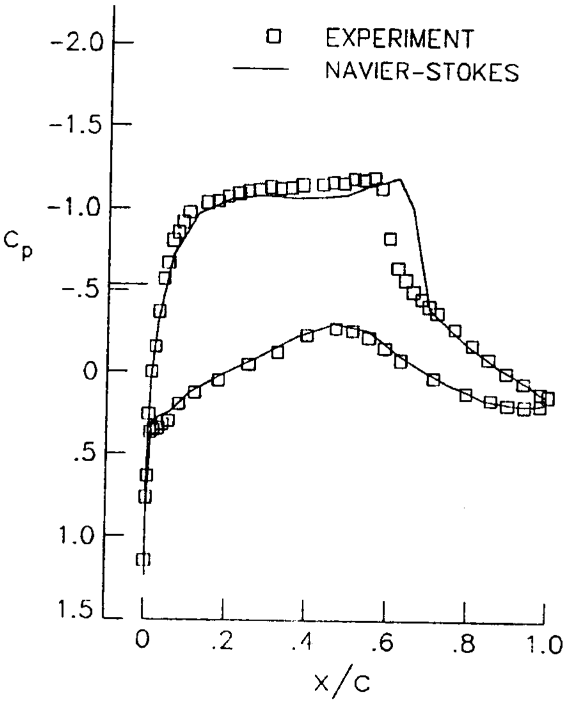

Figure 5:
Pressure distribution
Osher P scheme, $\kappa = \frac{1}{3}$
Chakravarthy-Osher limiter
81x17 mesh (48)

ORIGINAL PAGE IS OF POOR QUALITY

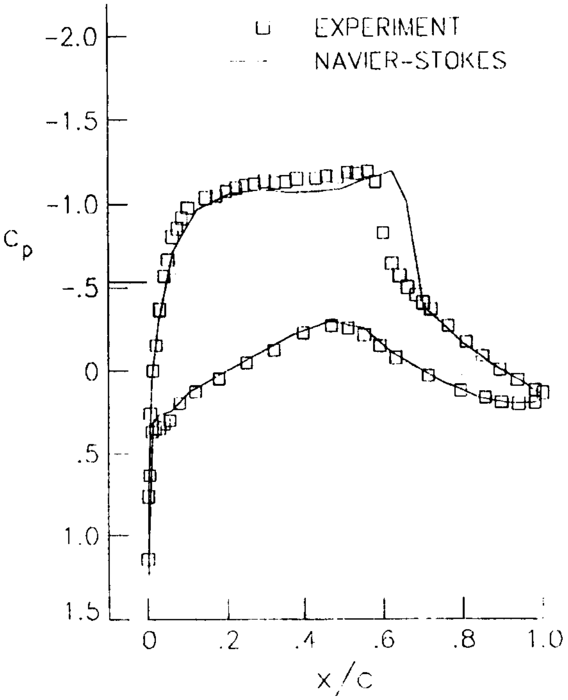

Figure 6:
Pressure distribution
Roee scheme, $\kappa = \frac{1}{3}$
Chakravarthy-Osher limiter
81x17 mesh (48)

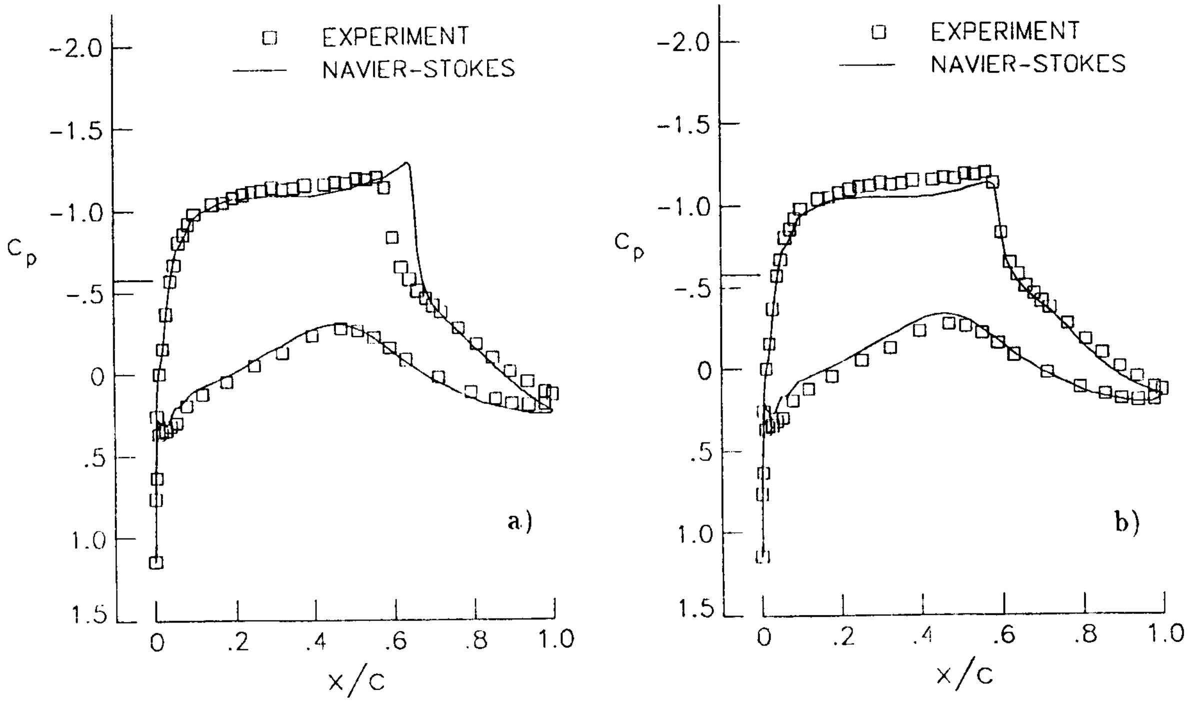

Figure 7:
Influence of the turbulence modeling
Roe scheme
a) Baldwin-Lomax model
b) Johnson-King model
321x65 mesh (192)

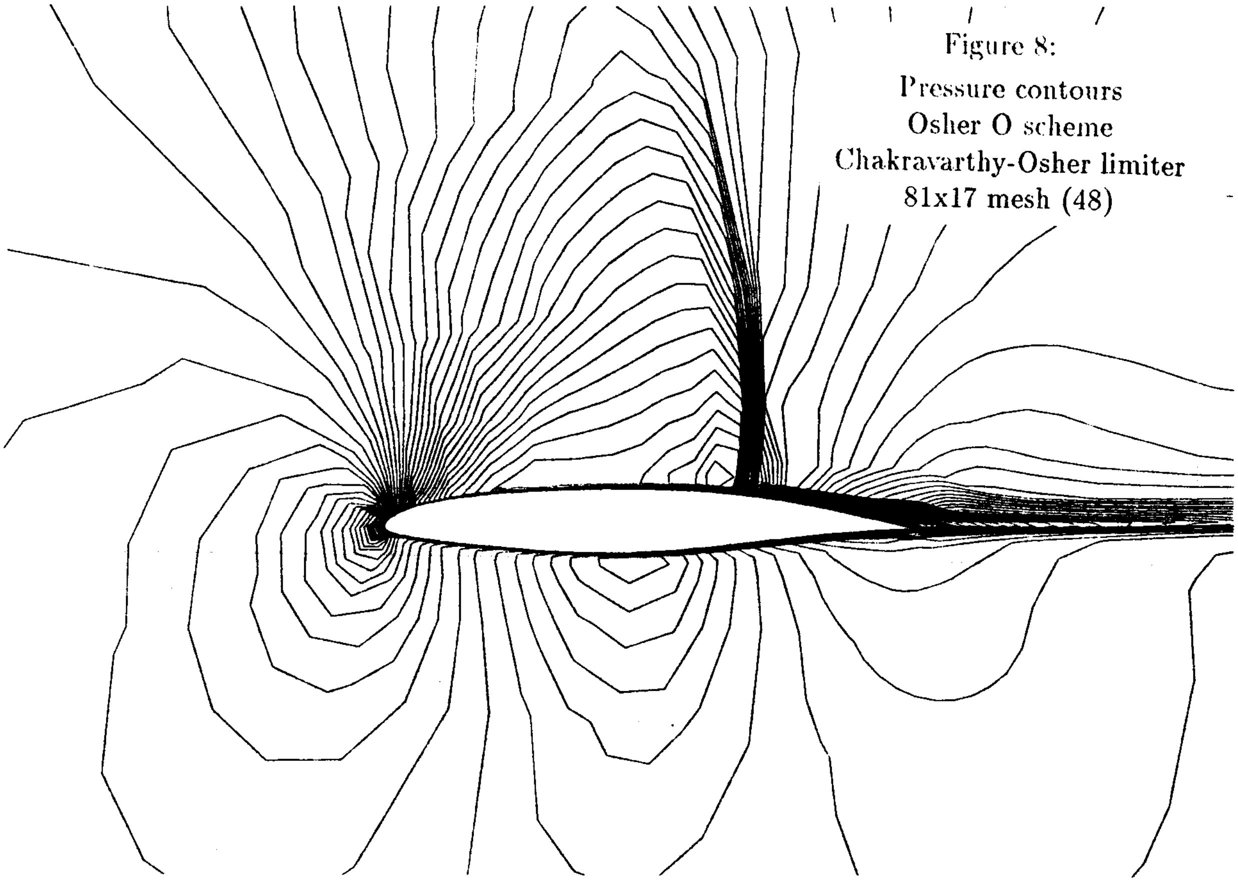

Figure 8:

Pressure contours

Osher O scheme

Chakravarthy-Osher limiter

81x17 mesh (48)

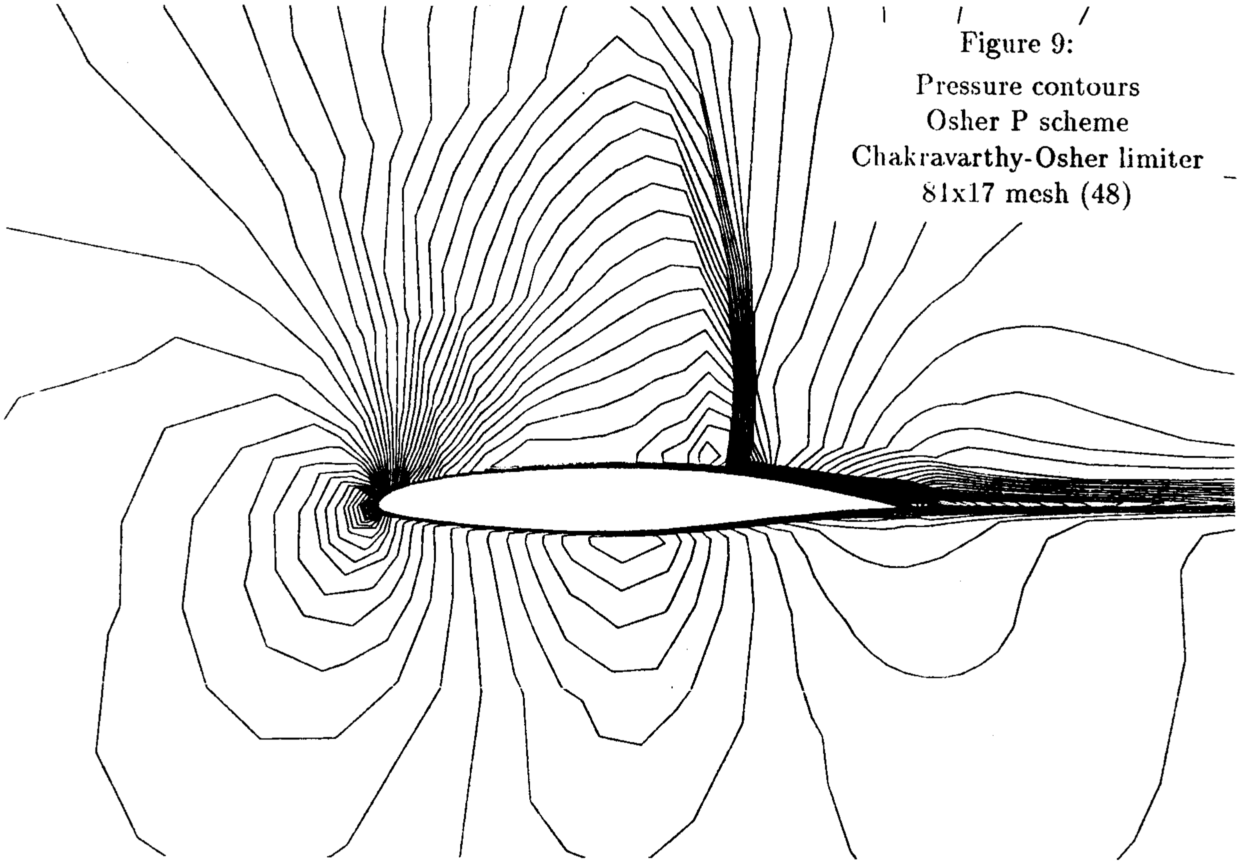

Figure 9:

Pressure contours

Osher P scheme

Chakravarthy-Osher limiter

81x17 mesh (48)

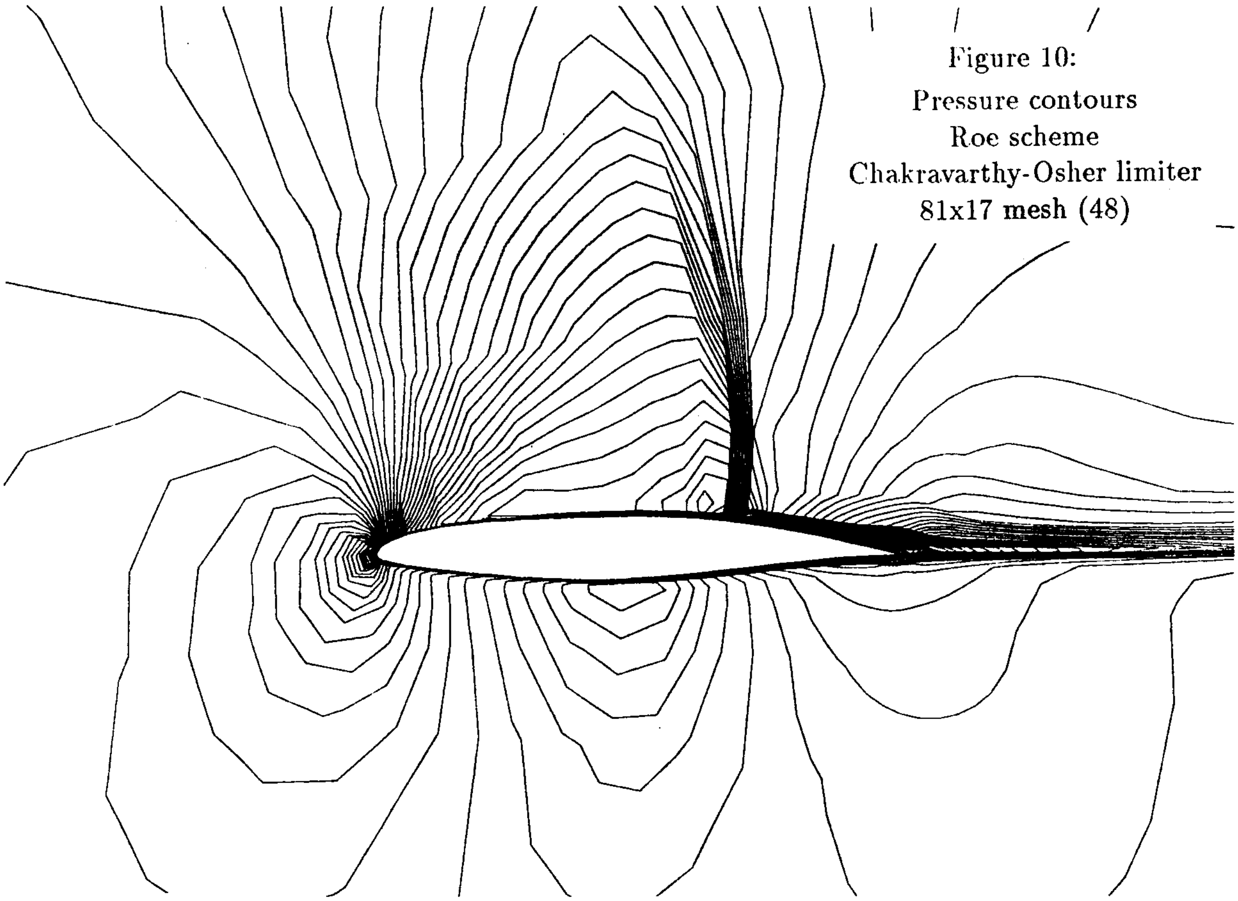

Figure 10:
Pressure contours
Roe scheme
Chakravarthy-Osher limiter
81x17 mesh (48)

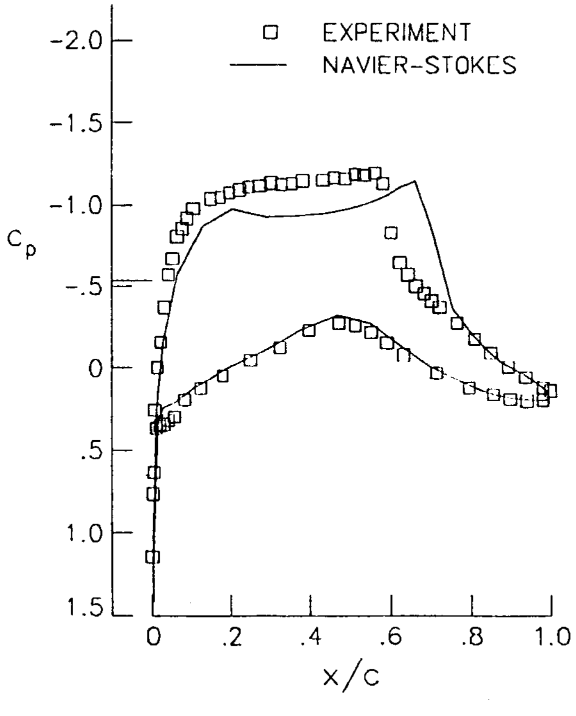

Figure 11:
Pressure distribution (CAST10)
Roe scheme
Harten-Osher limiter
81x17 mesh (48)

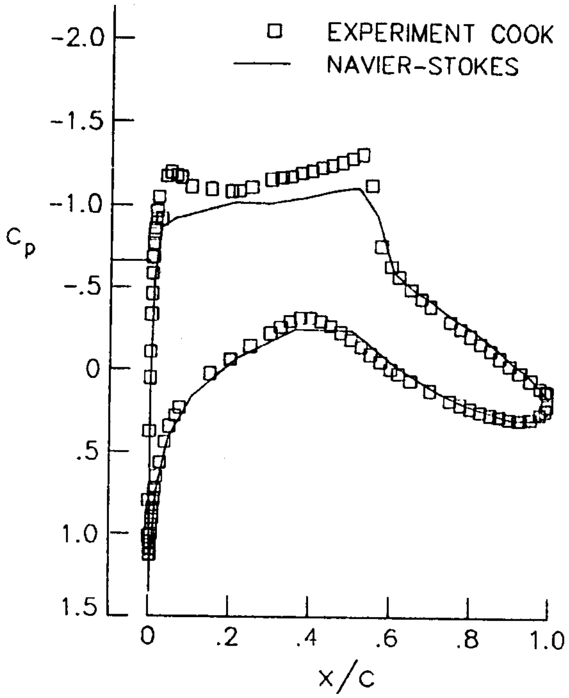

Figure 12:
Pressure distribution (RAE2822)
Roe scheme
Harten-Osher limiter
81x17 mesh (48)

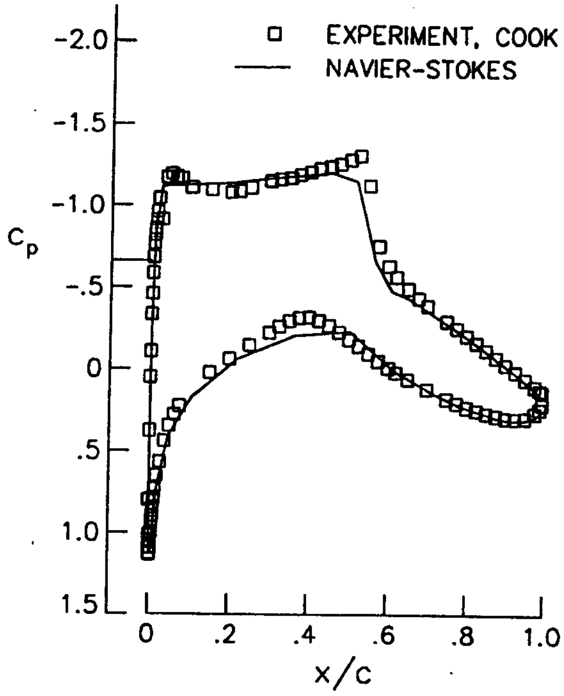

Figure 13:
Pressure distribution (RAE2822)
Roe scheme
Chakravarthy-Osher limiter $\kappa = \frac{1}{3}$
81x17 mesh (48)

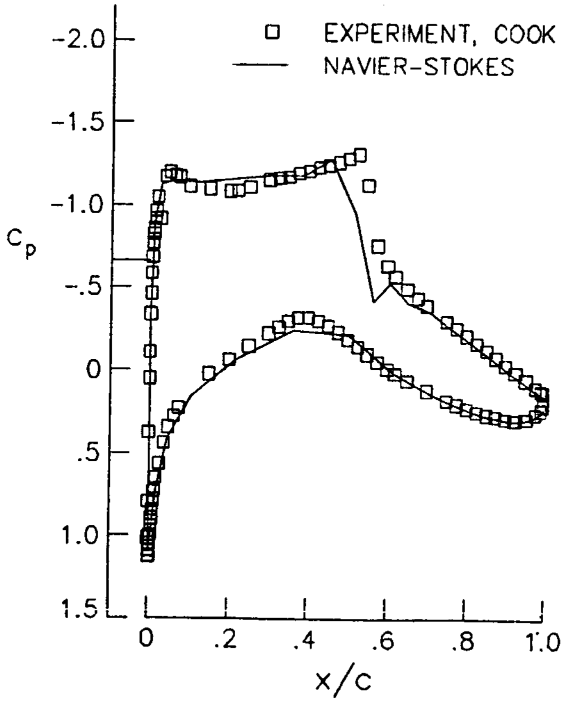

Figure 14:
Pressure distribution (RAE2822)
Roe scheme
Unlimited third order scheme
81x17 mesh (48)

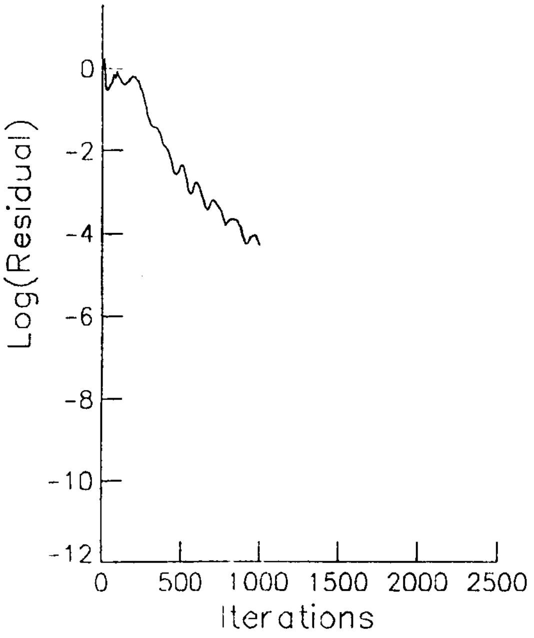

Figure 15:
Convergence history
Osher O scheme, $\kappa = -1$
Unlimited
CFL=50, relax=0.5
161x33 mesh (96)

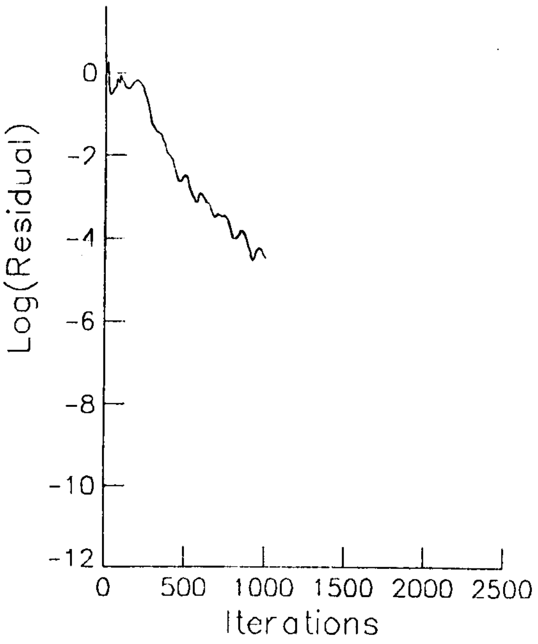

Figure 16:
Convergence history
Osher P scheme, $\kappa = -1$
Unlimited
CFL=50, relax=0.5
161x33 mesh (96)

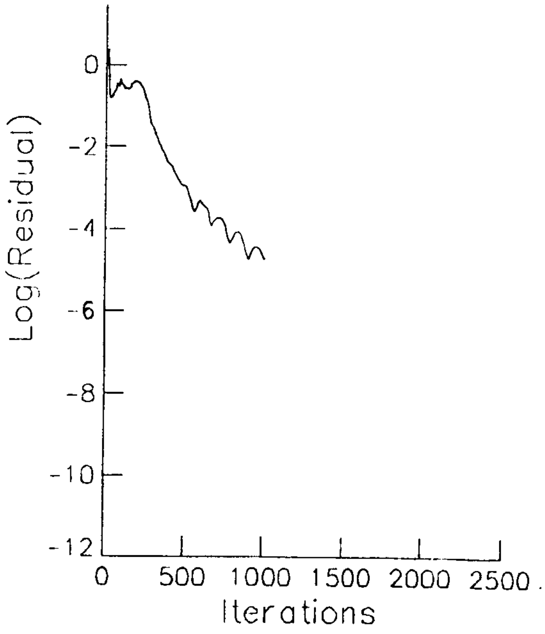

Figure 17:
Convergence history
Roe scheme, $\kappa = -1$
Unlimited
CFL=50, relax=0.5
161x33 mesh (96)

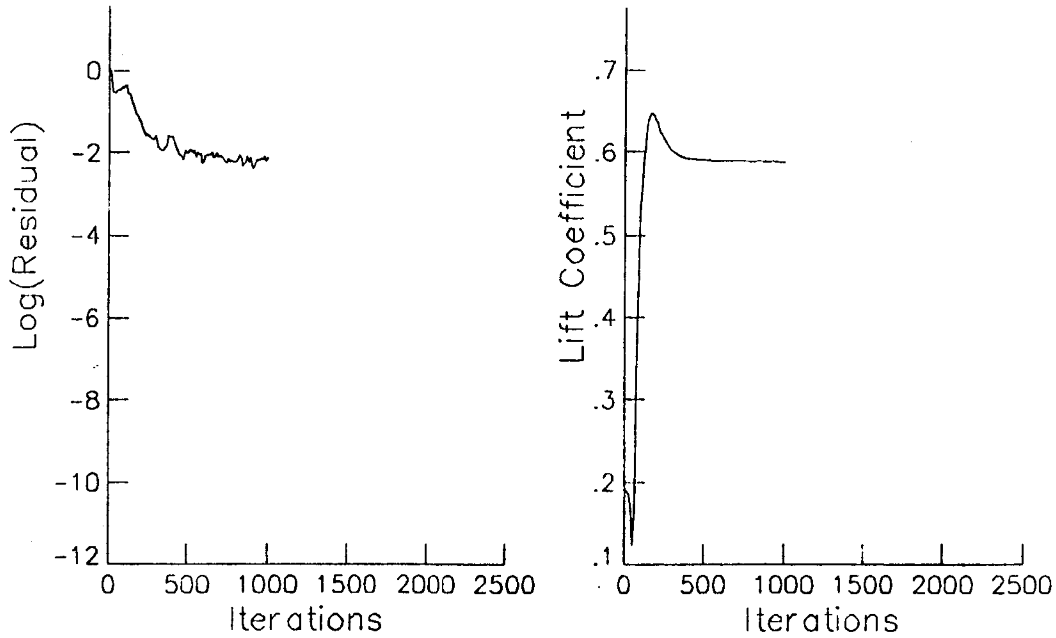

Figure 18:

Convergence history
Chakravarthy-Osher limiter, $\kappa = \frac{1}{3}$
CFL=25, relax=0.5
161x33 mesh (96)

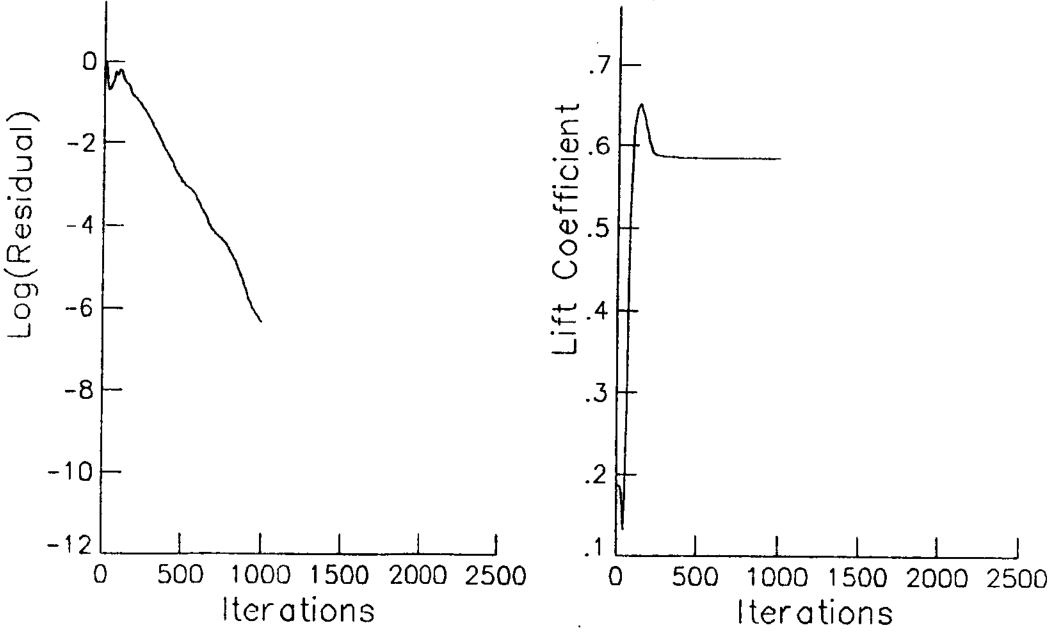

Figure 19:

Convergence history
Unlimited $\kappa = \frac{1}{3}$
CFL=50, relax=0.5
161x33 mesh (96)

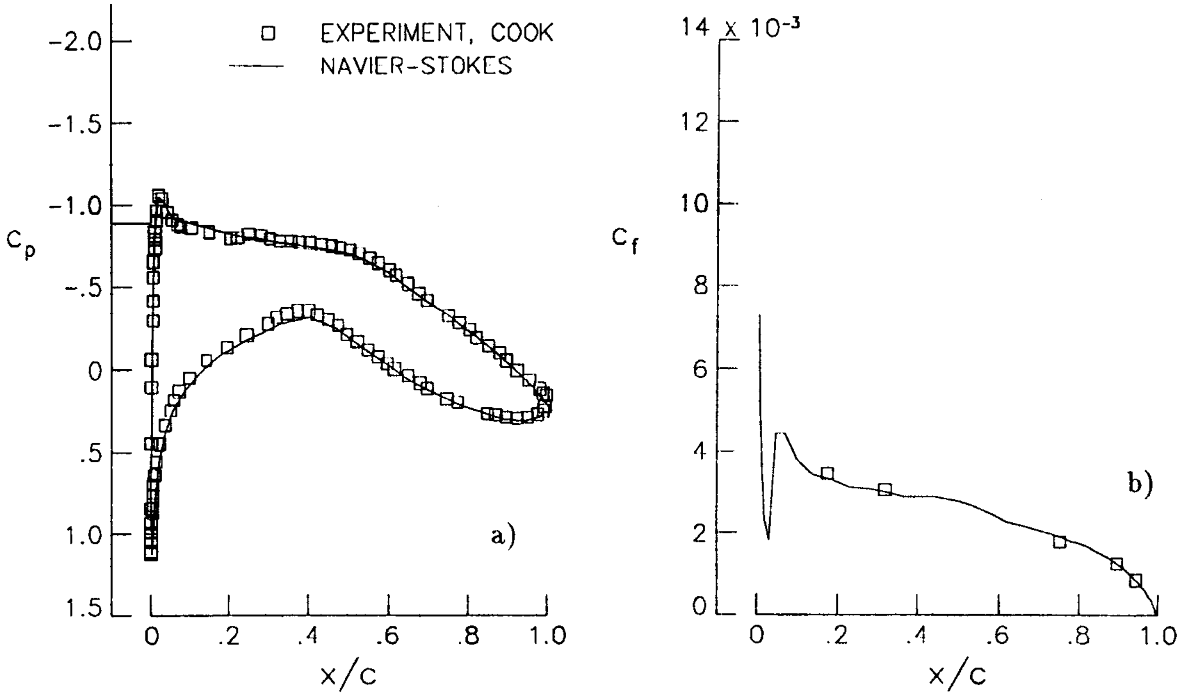

Figure 20:
Pressure (a) and Skin friction (b) distributions
Chakravarthy-Osher limiter $\kappa = \frac{1}{3}$
161x33 mesh (96)

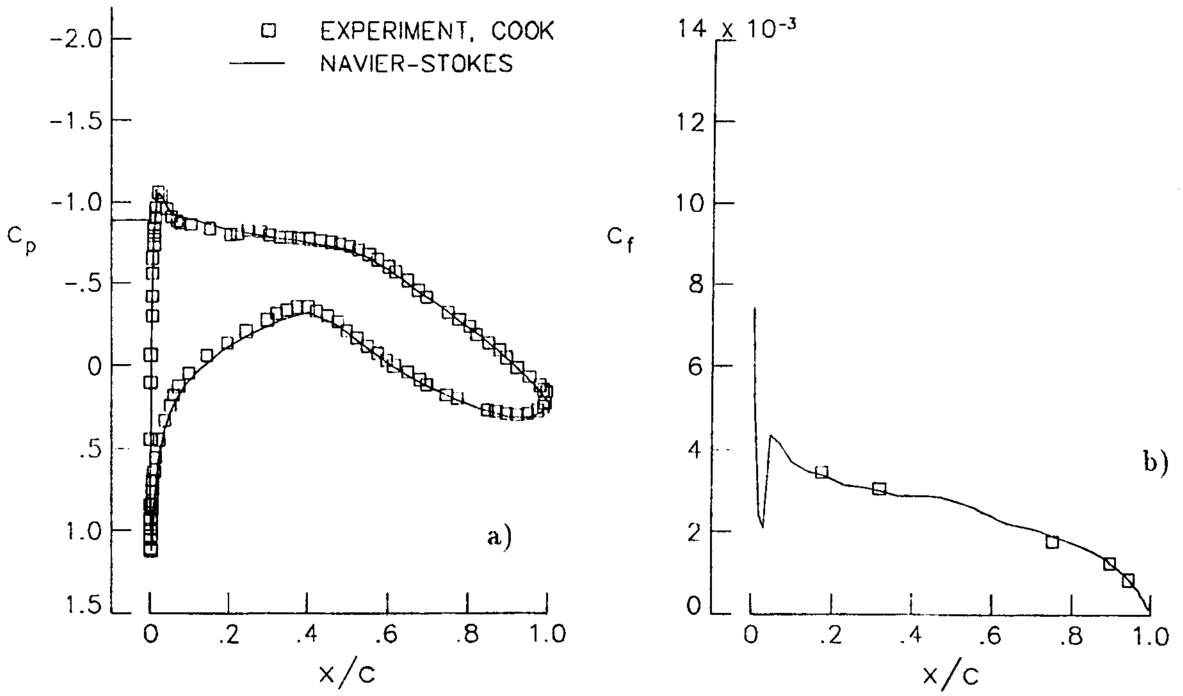

Figure 21:
Pressure (a) and Skin friction (b) distributions
Unlimited $\kappa = \frac{1}{3}$
161x33 mesh (96)

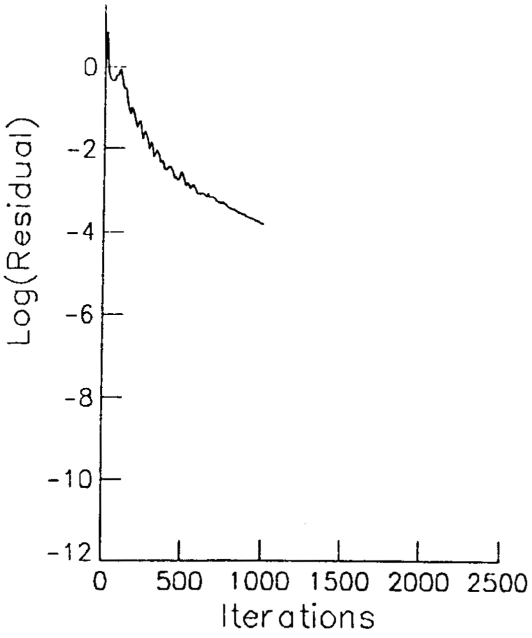

Figure 22:
Convergence history
Unlimited $\kappa = \frac{1}{3}$
CFL=10, relax=1
161x33 mesh (96)

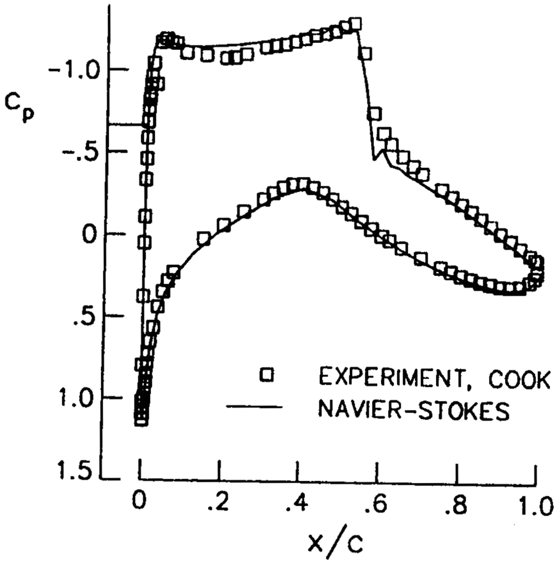

Figure 23:
RAE2822 $M_\infty = .73$, $\alpha = 2.79$, $\mathrm{Re} = 6.5 \times 10^6$ (case 9)
Pressure distribution
Unlimited $\kappa = \frac{1}{3}$
CFL=30, relax=0.5
161x33 mesh (96)

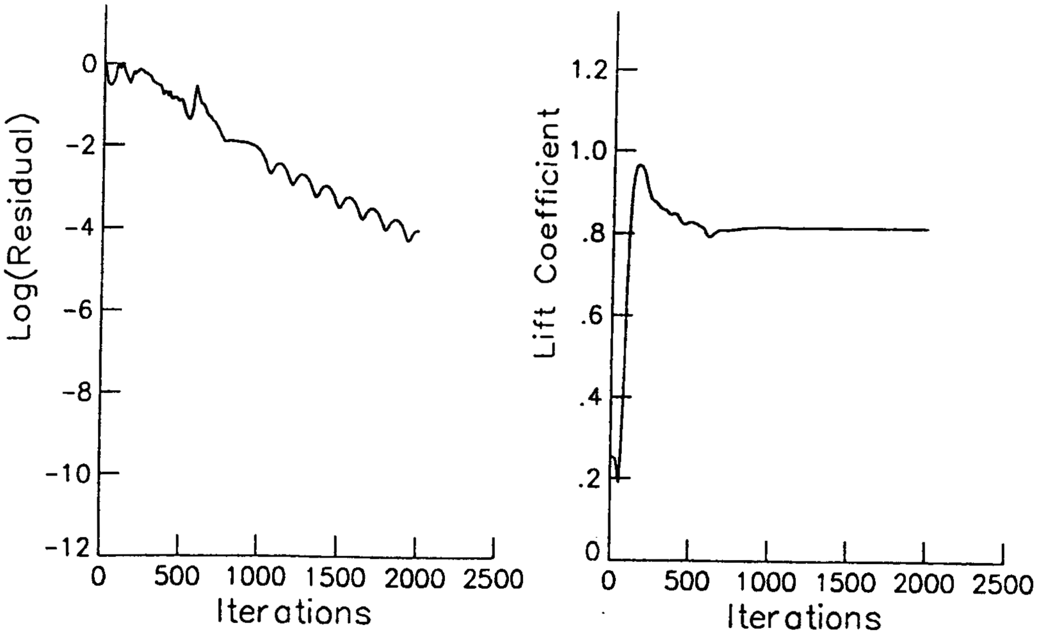

Figure 24:
Convergence history
Unlimited $\kappa = \frac{1}{3}$
CFL=30, relax=0.5
161x33 mesh (96)

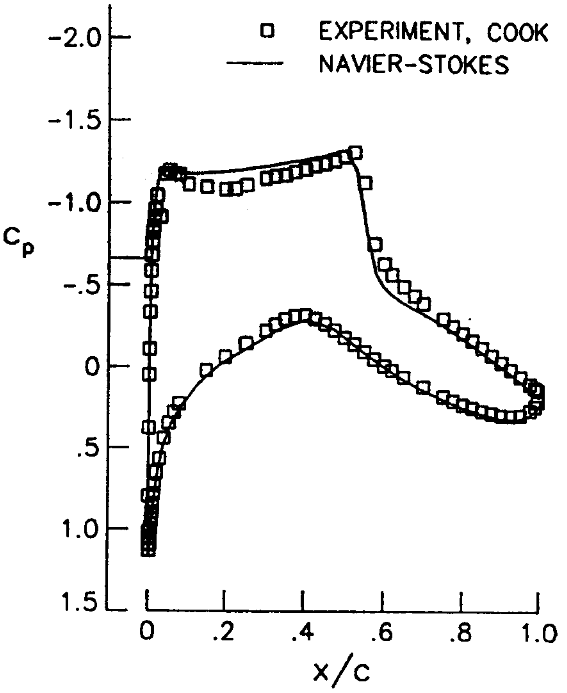

Figure 25:
Pressure distribution
Unlimited $\kappa = -1$
161x33 mesh (96)

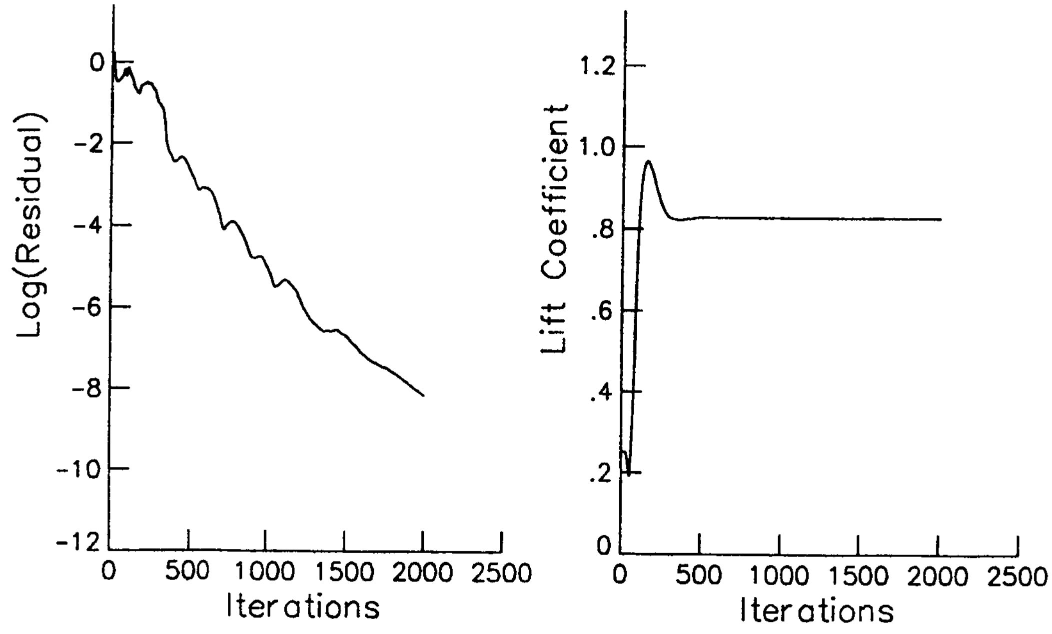

Figure 26:
Convergence history
Unlimited $\kappa = -1$
CFL=30, relax=0.5
161x33 mesh (96)

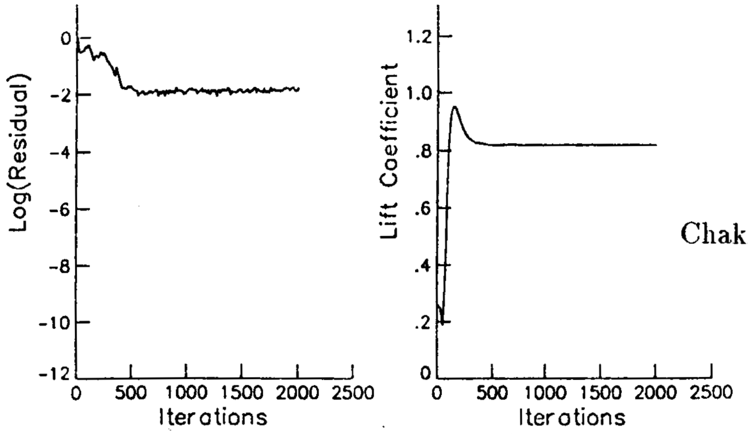

Figure 27:
Convergence history
Chakravarthy-Osher limiter $\kappa = \frac{1}{3}$
CFL=30, relax=0.5
161x33 mesh (96)

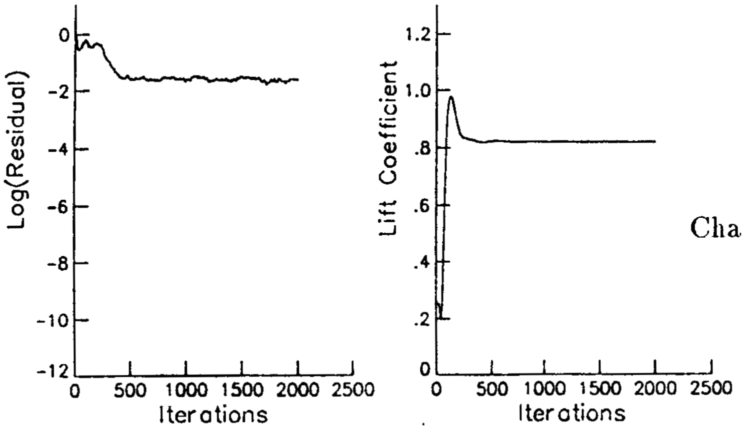

Figure 28:
Convergence history
Chakravarthy-Osher limiter $\kappa = \frac{1}{3}$
CFL=50, relax=0.5
161x33 mesh (96)

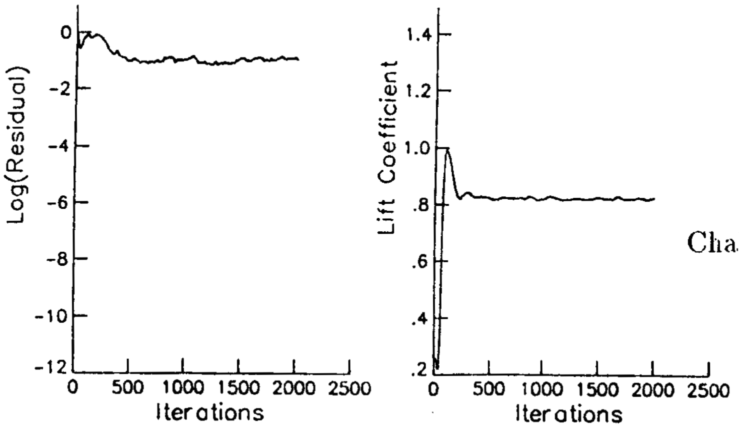

Figure 29:
Convergence history
Chakravarthy-Osher limiter $\kappa = \frac{1}{3}$
CFL=100, relax=0.5
161x33 mesh (96)

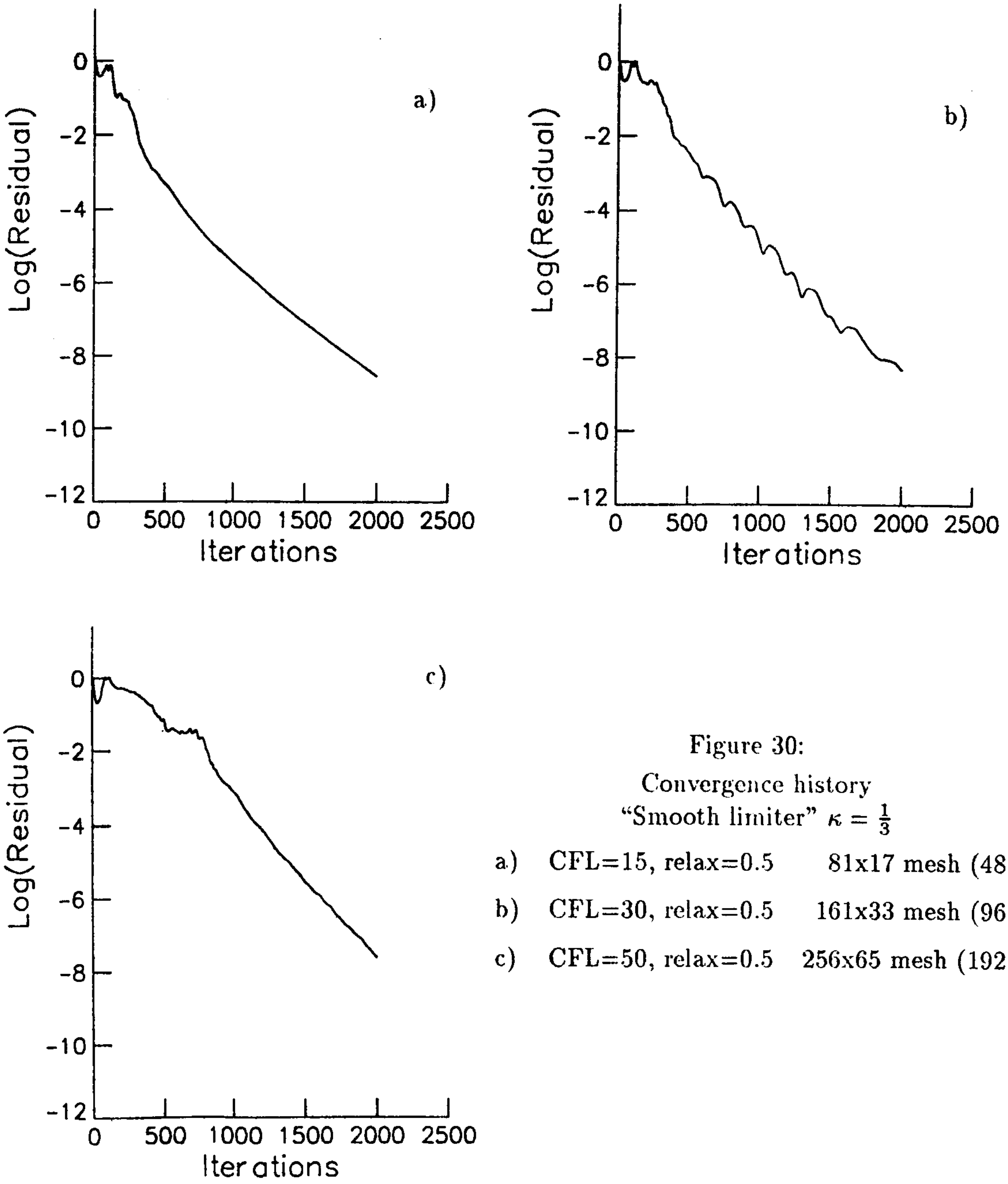

Figure 30:
Convergence history
"Smooth limiter" $\kappa = \frac{1}{3}$

a)	CFL=15, relax=0.5	81x17 mesh (48)
b)	CFL=30, relax=0.5	161x33 mesh (96)
c)	CFL=50, relax=0.5	256x65 mesh (192)

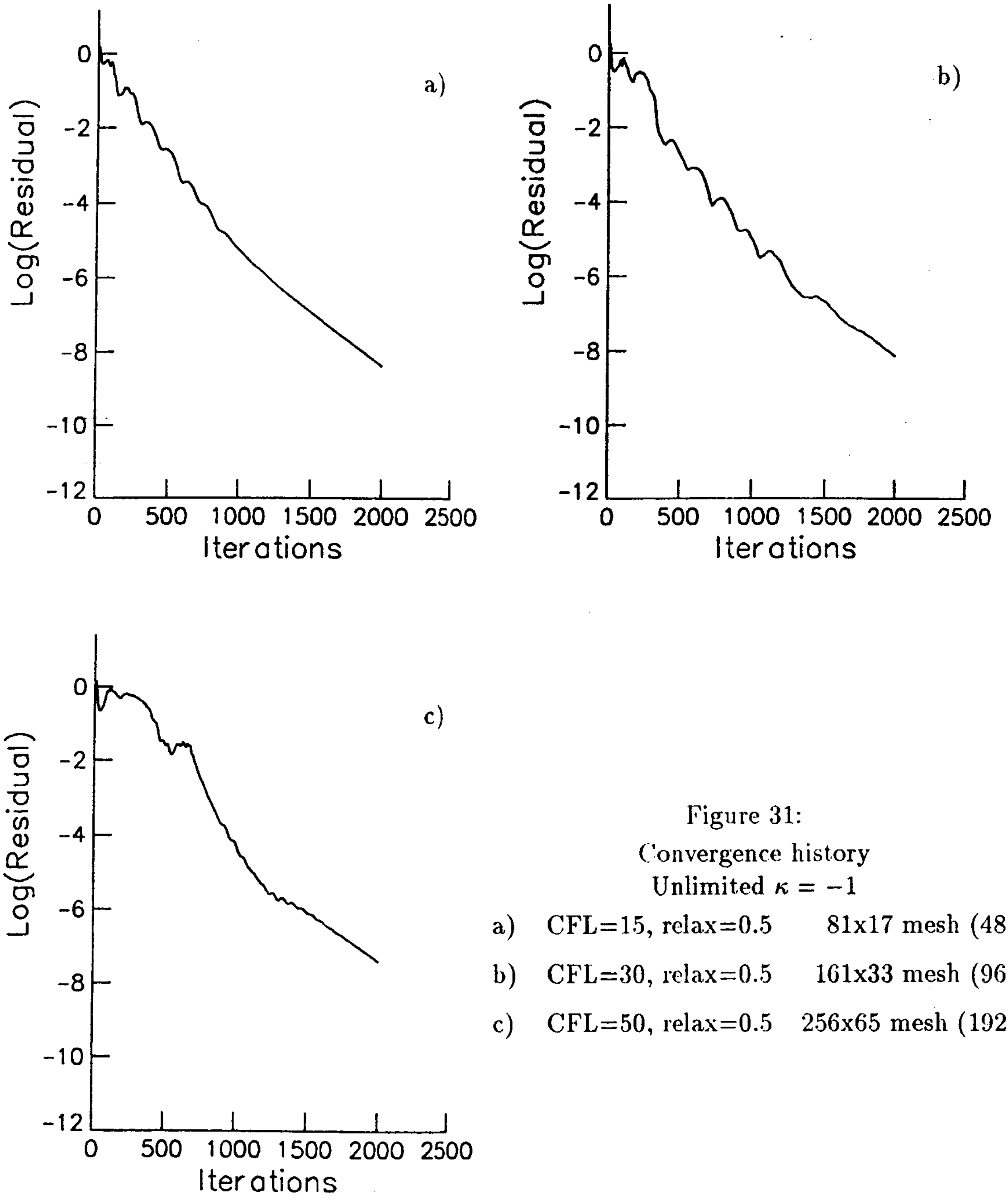

Figure 31:
Convergence history
Unlimited $\kappa = -1$

a) CFL=15, relax=0.5 81x17 mesh (48)
b) CFL=30, relax=0.5 161x33 mesh (96)
c) CFL=50, relax=0.5 256x65 mesh (192)

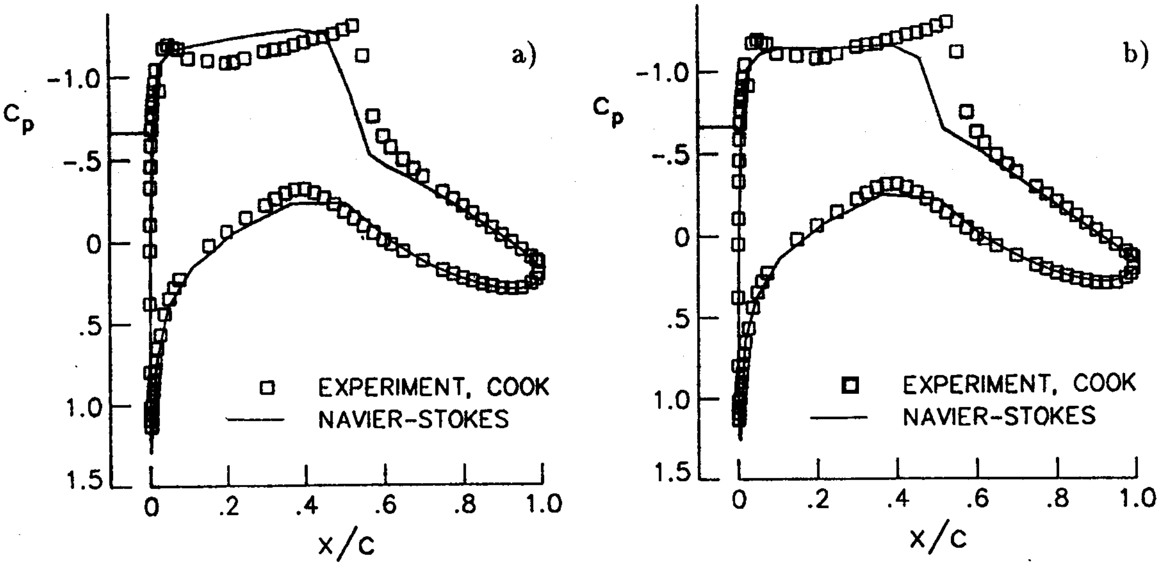

Figure 32:
Pressure distributions
a) unlimited $\kappa = -1$
b) "Smooth limiter" $\kappa = \frac{1}{3}$
c) Chakravarthy-Osher limiter $\kappa = \frac{1}{3}$
d) unlimited $\kappa = \frac{1}{3}$
81x17 mesh (48)

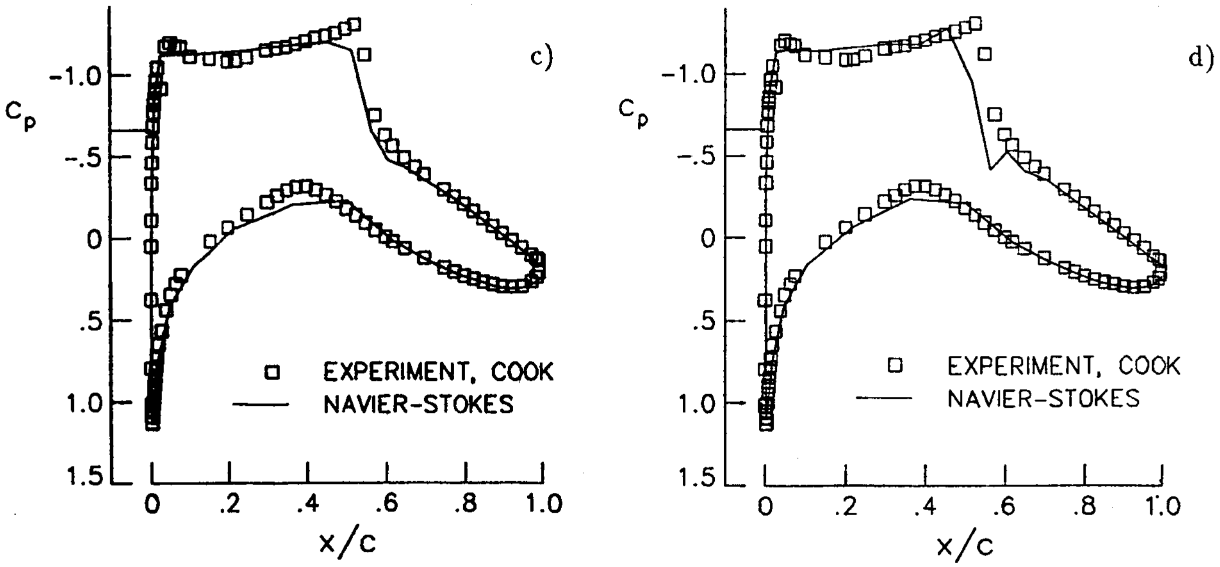

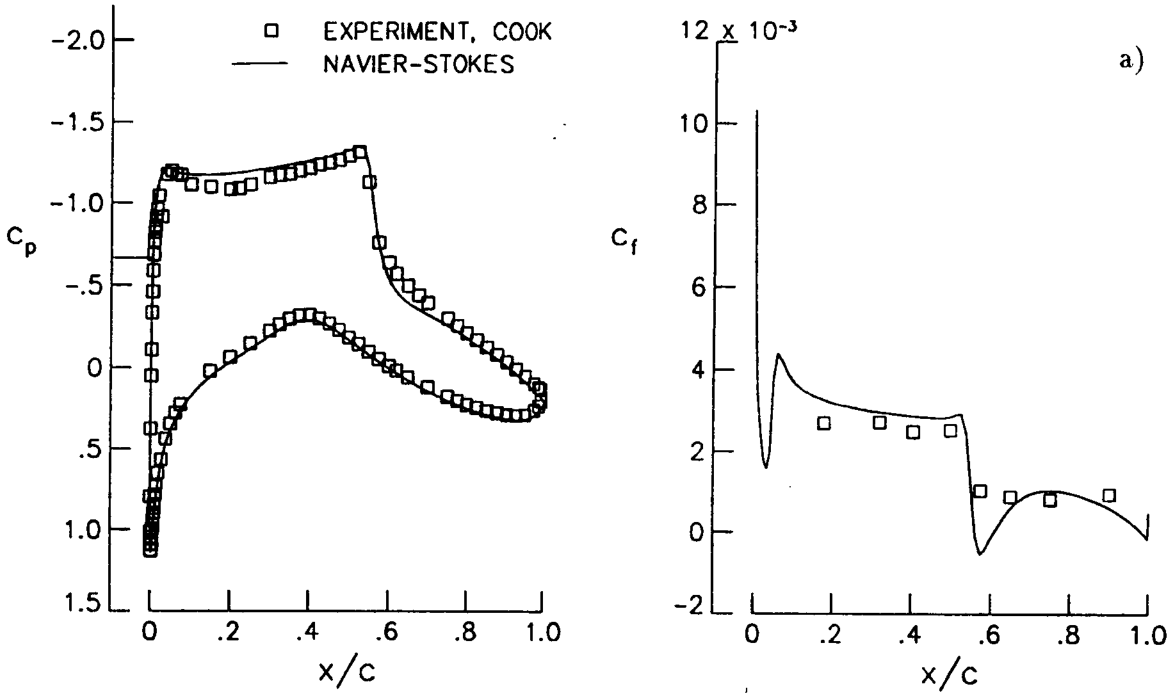
EXPERIMENT, COOK
NAVIER-STOKES
a)
C_p
-2.0
-1.5
-1.0
-.5
0
.5
1.0
1.5
0
.2
.4
.6
.8
1.0
x/c
C_f
12 x 10^-3
10
8
6
4
2
0
-2
x/c

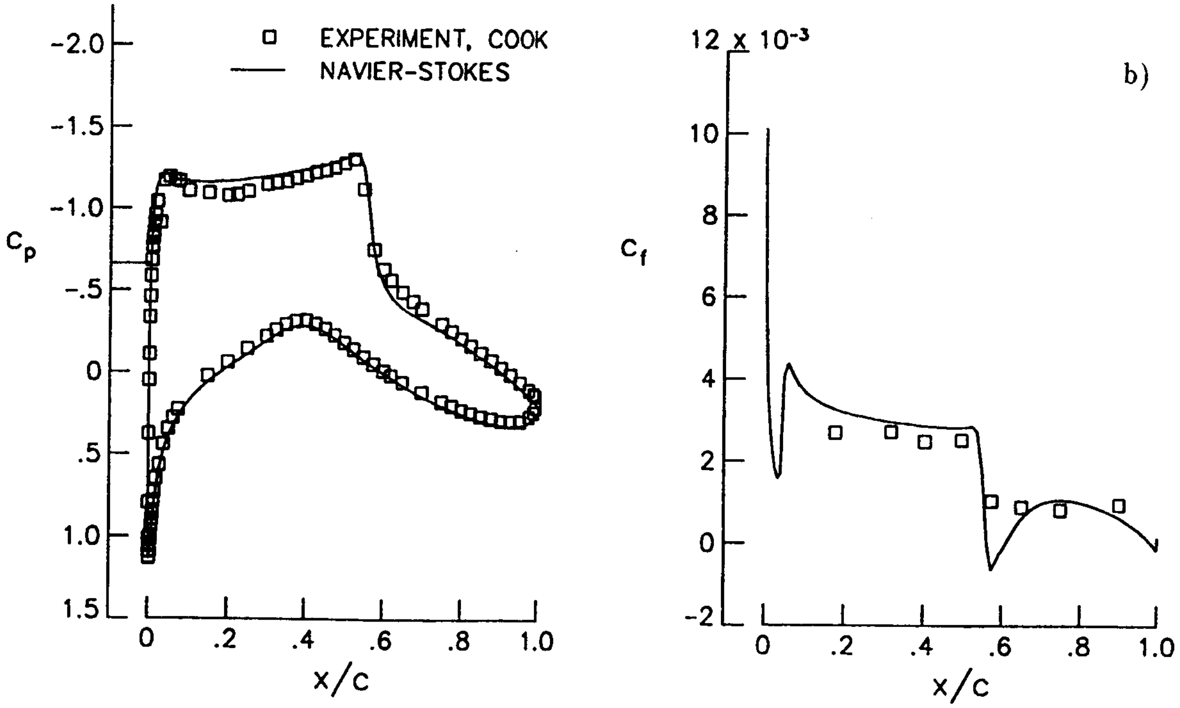
EXPERIMENT, COOK
NAVIER-STOKES
b)
C_p
-2.0
-1.5
-1.0
-.5
0
.5
1.0
1.5
0
.2
.4
.6
.8
1.0
x/c
C_f
12 x 10^-3
10
8
6
4
2
0
-2
x/c

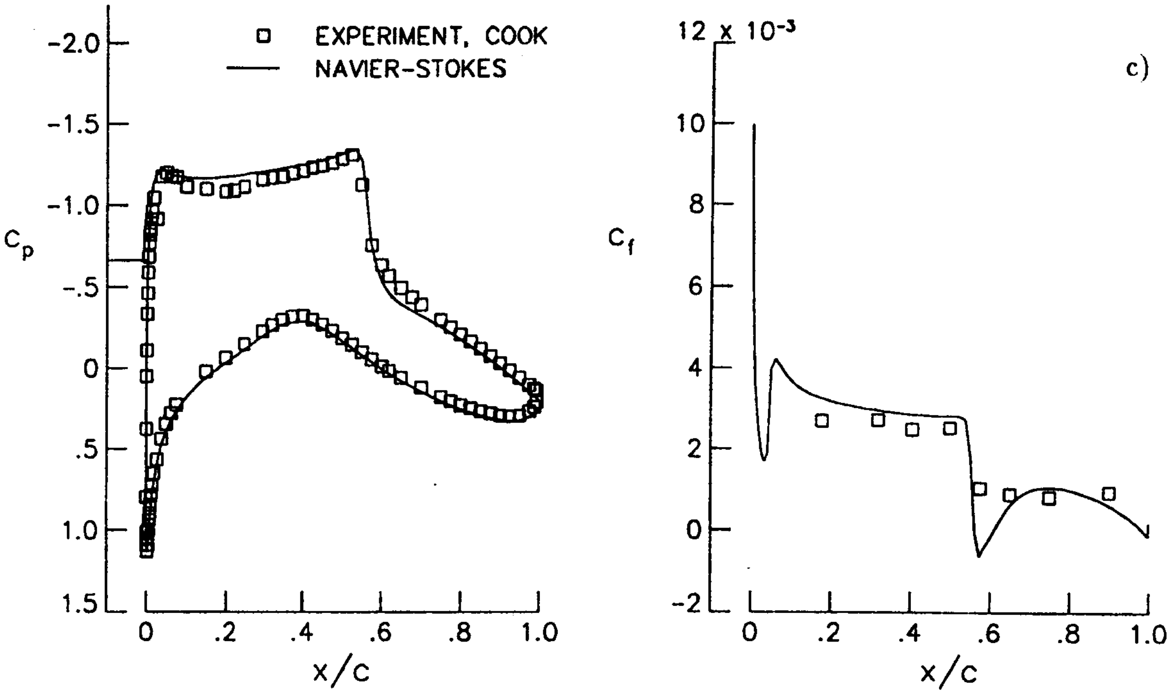

Figure 33:

Pressure and skin friction distributions

a) unlimited $\kappa = -1$

b) "Smooth limiter" $\kappa = \frac{1}{3}$

c) Chakravarthy-Osher limiter $\kappa = \frac{1}{3}$

257x65 mesh(192)

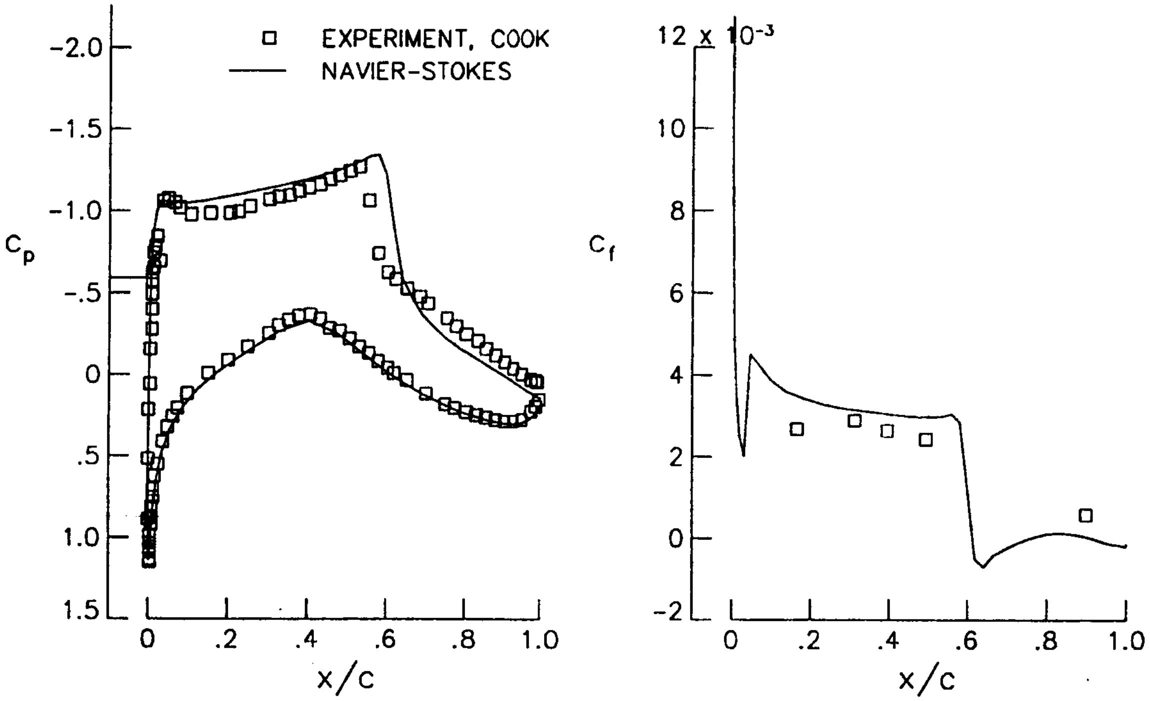

Figure 34:
Pressure and skin friction distributions
RAE2822 (case 10)
"Smooth limiter" $\kappa = \frac{1}{3}$
161x33 mesh (96)

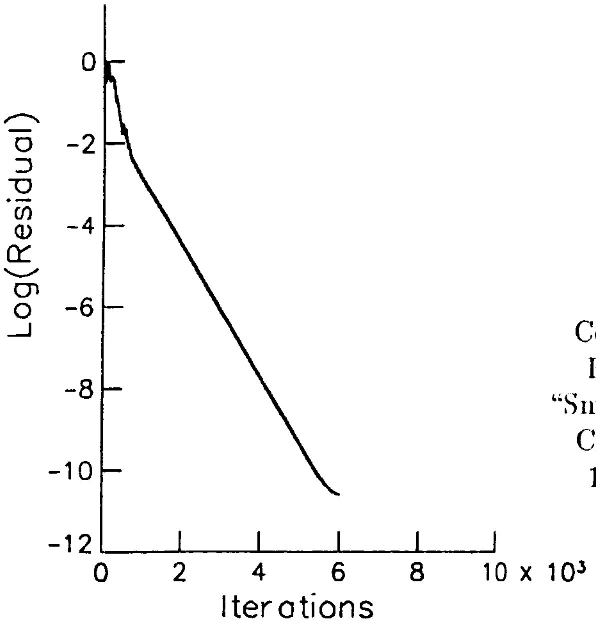

Figure 35:
Convergence history
Rae2822 (case 10)
"Smooth limiter" $\kappa = \frac{1}{3}$
CFL=30, relax=0.5
161x33 mesh (96)

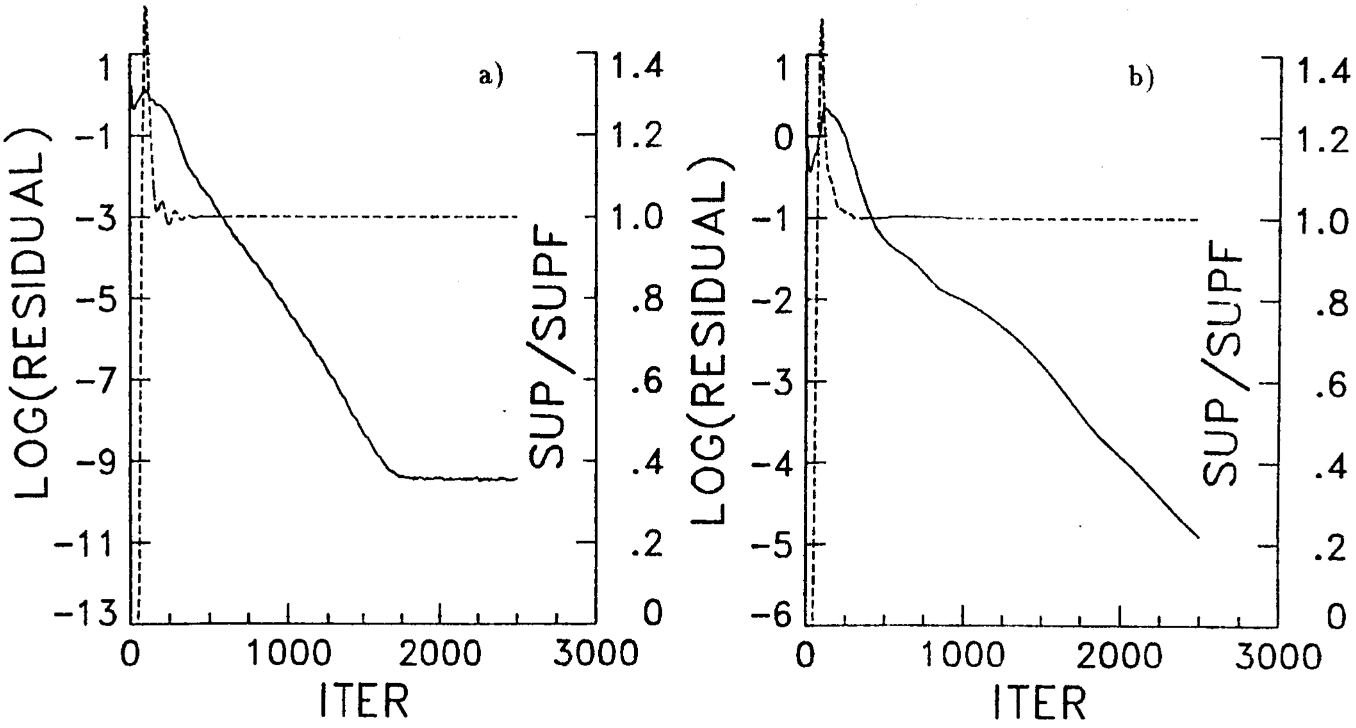

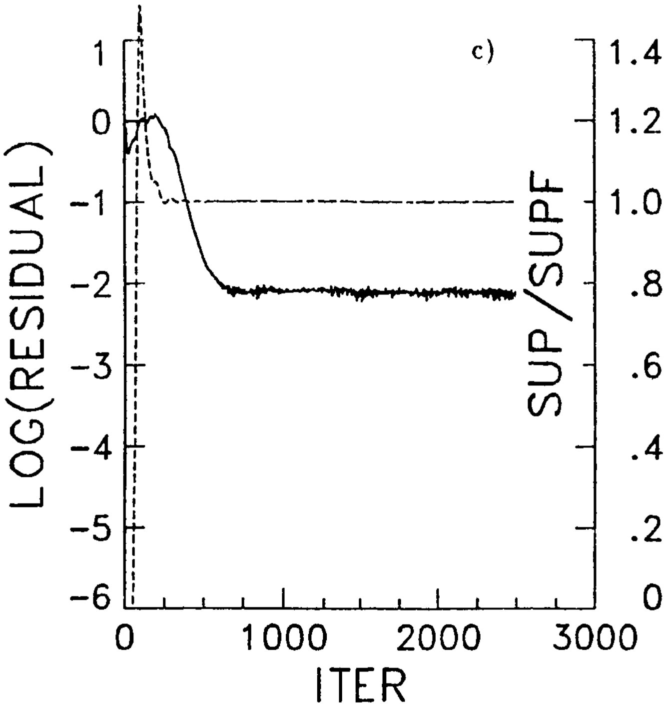

Figure 36:
Convergence history
ONERA M6 $M_\infty = .84$, $\alpha = 3.06$, Re = 11×10^6

a) unlimited $\kappa = -1$

b) "Smooth limiter" $\kappa = \frac{1}{3}$

c) Chakravarthy-Osher limiter $\kappa = \frac{1}{3}$

97x25x17 mesh

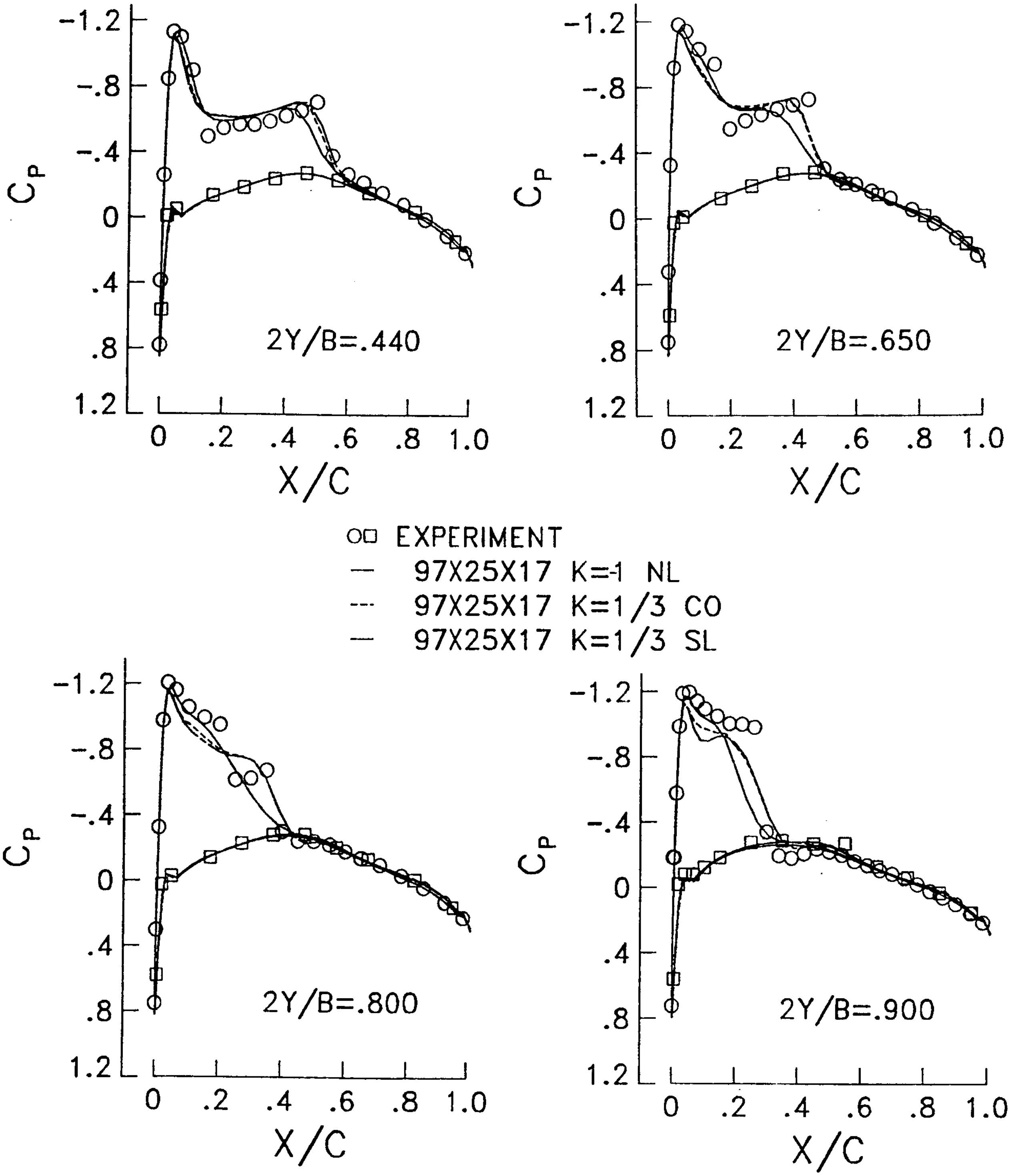

Figure 37:

Pressure distributions

ONERA M6 $M_\infty = .84$, $\alpha = 3.06$, Re = 11×10^6

97x25x17 mesh

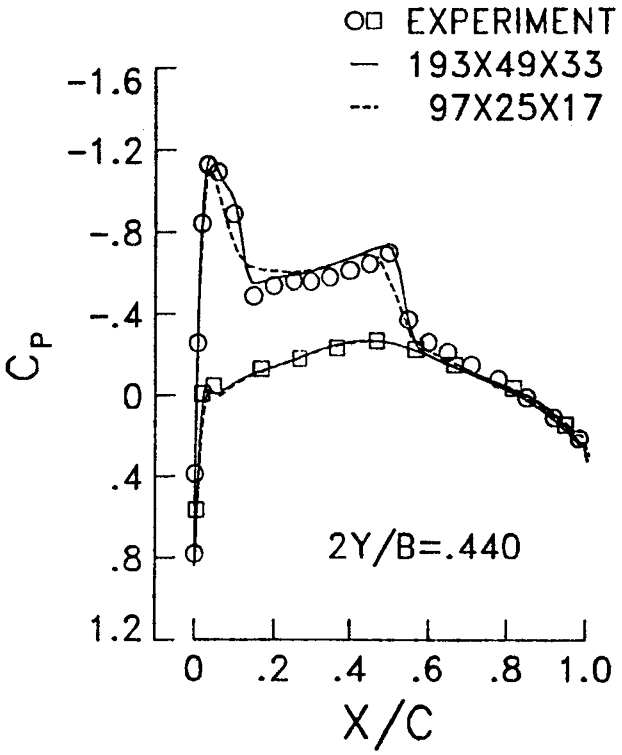

○□ EXPERIMENT
— 193X49X33
--- 97X25X17
-1.6
-1.2
-.8
-.4
0
.4
.8
1.2
C_P
0
.2
.4
.6
.8
1.0
X/C
2Y/B=.440

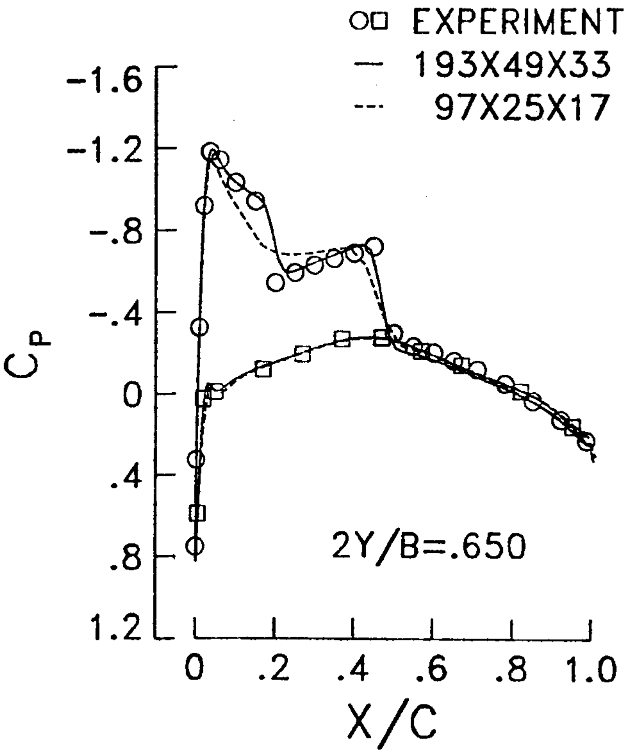

○□ EXPERIMENT
— 193X49X33
--- 97X25X17
-1.6
-1.2
-.8
-.4
0
.4
.8
1.2
C_P
0
.2
.4
.6
.8
1.0
X/C
2Y/B=.650

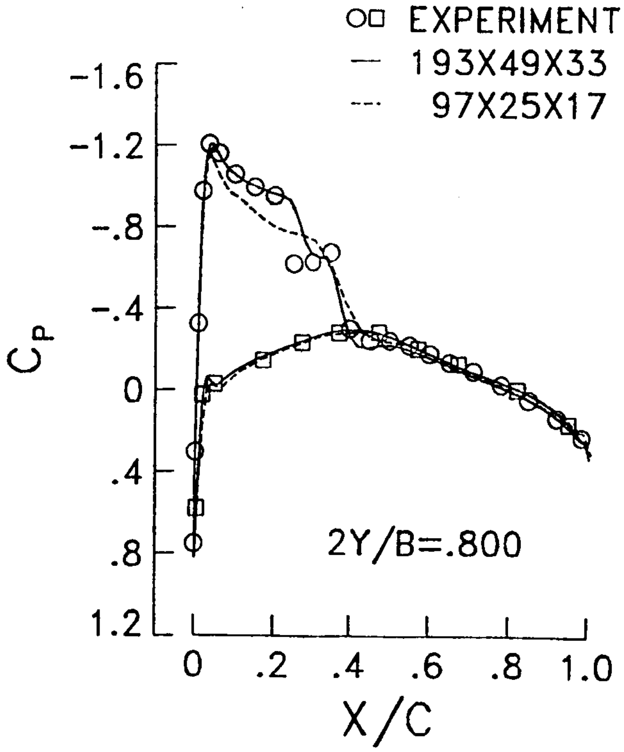

○□ EXPERIMENT
— 193X49X33
--- 97X25X17
-1.6
-1.2
-.8
-.4
0
.4
.8
1.2
C_P
0
.2
.4
.6
.8
1.0
X/C
2Y/B=.800

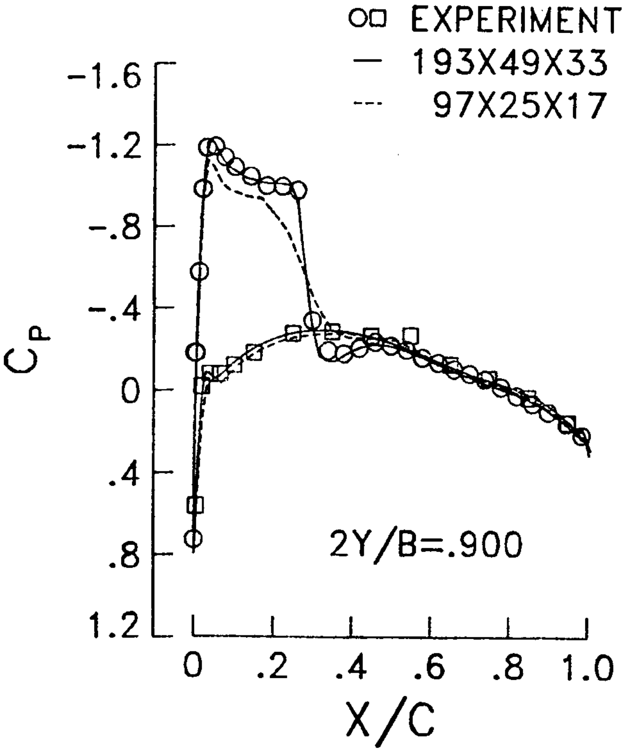

○□ EXPERIMENT
— 193X49X33
--- 97X25X17
-1.6
-1.2
-.8
-.4
0
.4
.8
1.2
C_P
0
.2
.4
.6
.8
1.0
X/C
2Y/B=.900

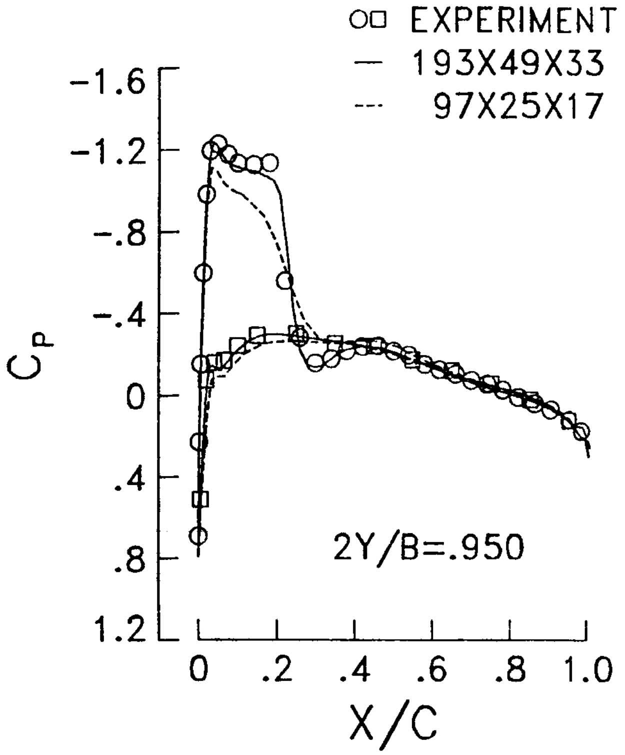

Figure 38:
Pressure distributions
ONERA M6 $M_\infty = .84$, $\alpha = 3.06$, Re = 11×10^6
Baldwin-Lomax model

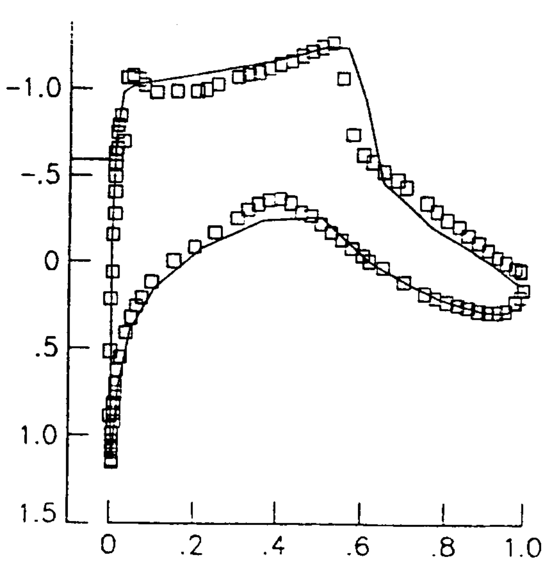

a)

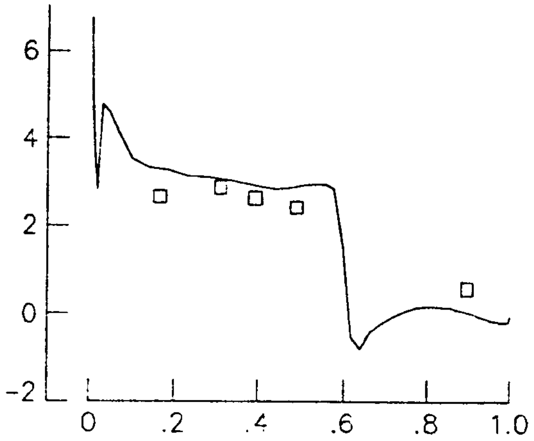

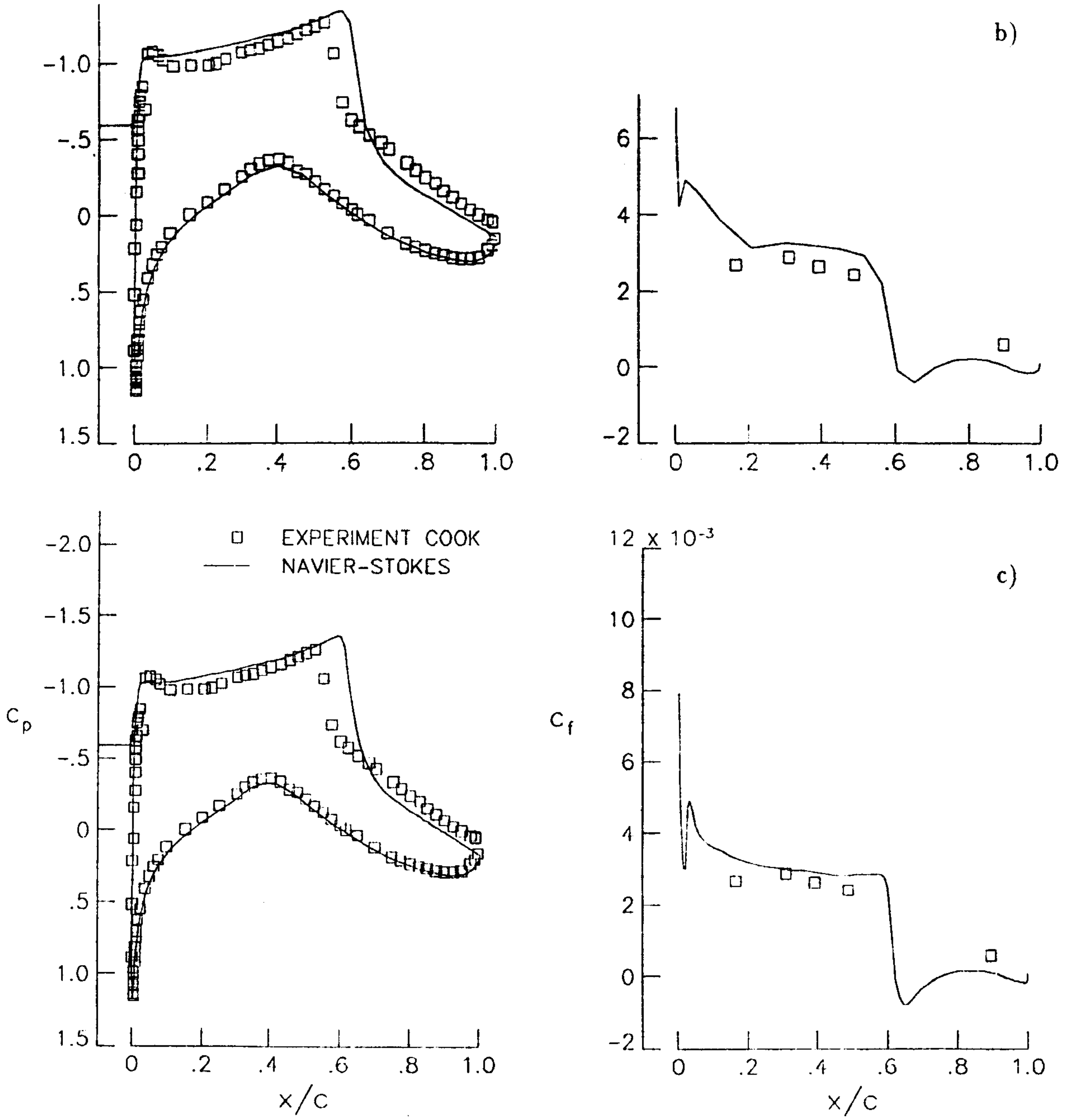

Figure 39:
Pressure and skin friction distributions
Rae2822 (case 10)
Baldwin-Lomax model
a) 81x17 mesh (48)
b) 161x33 mesh (96)
c) 257x65 mesh (192)

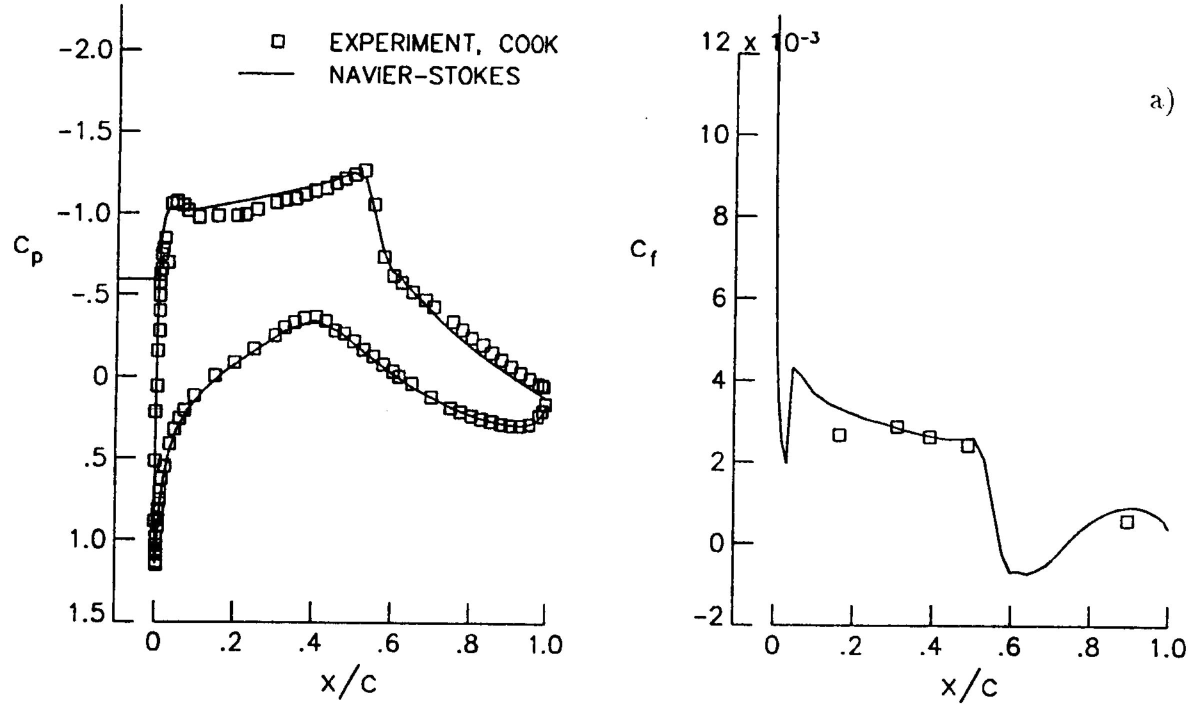

EXPERIMENT, COOK
NAVIER-STOKES
C_p
-2.0
-1.5
-1.0
-.5
0
.5
1.0
1.5
0
.2
.4
.6
.8
1.0
x/c
C_f
12×10^{-3}
10
8
6
4
2
0
-2
0
.2
.4
.6
.8
1.0
x/c
a)

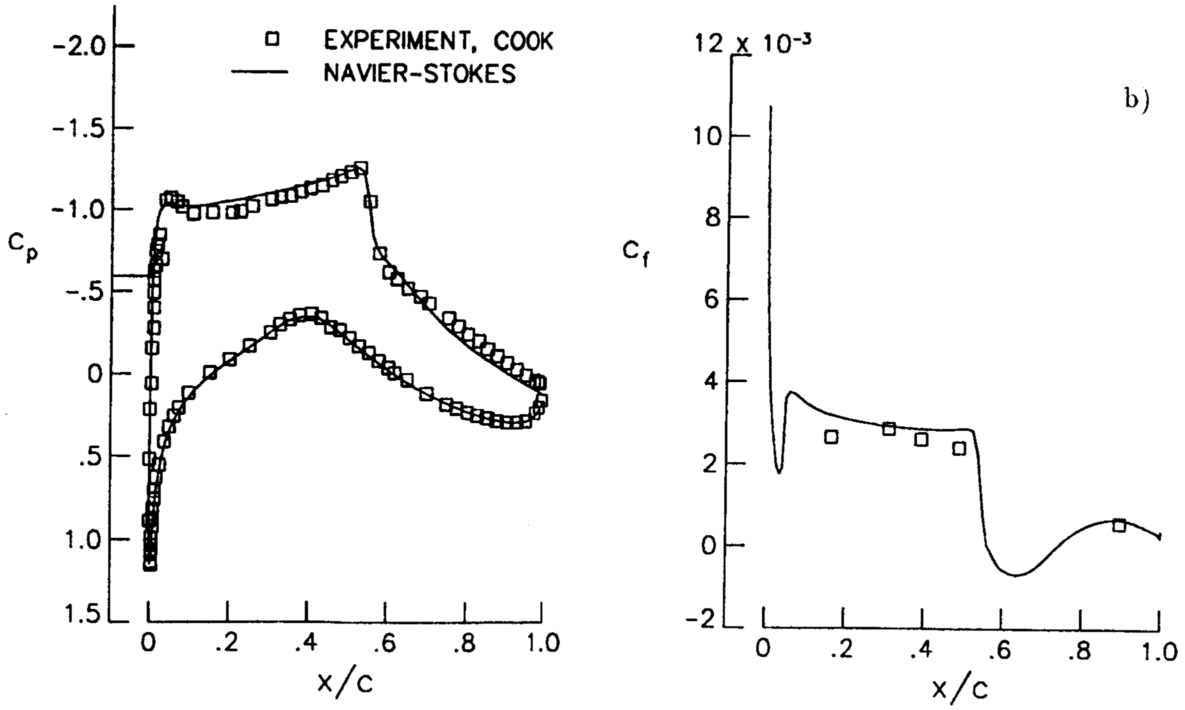

EXPERIMENT, COOK
NAVIER-STOKES
C_p
-2.0
-1.5
-1.0
-.5
0
.5
1.0
1.5
0
.2
.4
.6
.8
1.0
x/c
C_f
12×10^{-3}
10
8
6
4
2
0
-2
0
.2
.4
.6
.8
1.0
x/c
b)

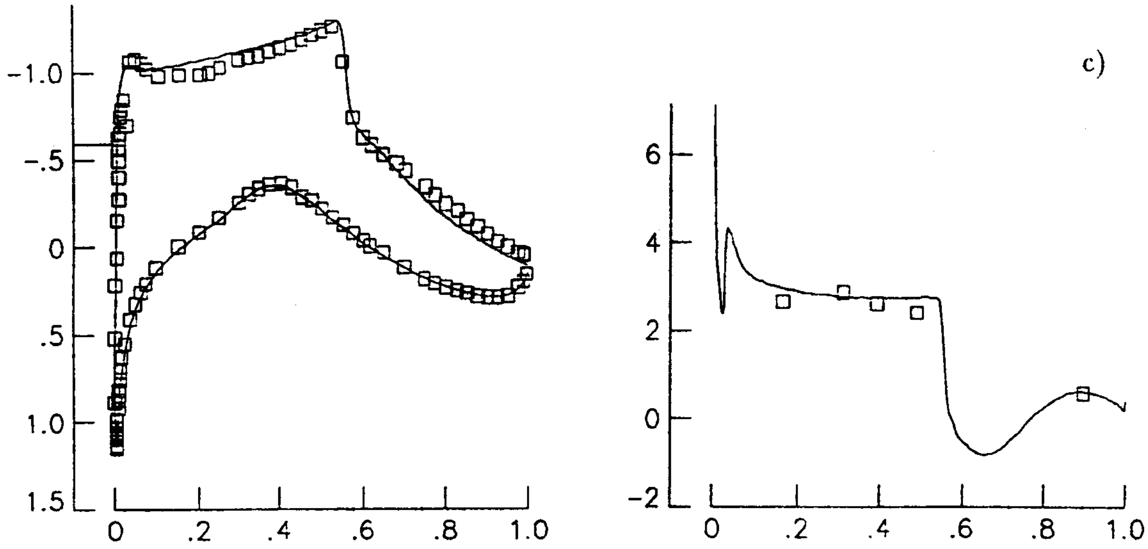

Figure 40:
Pressure and skin friction distributions
Rae2822 (case 10)
Johnson-King model

a) 161x33 mesh (96)

b) 257x65 mesh (192)

c) 321x65 mesh (256)

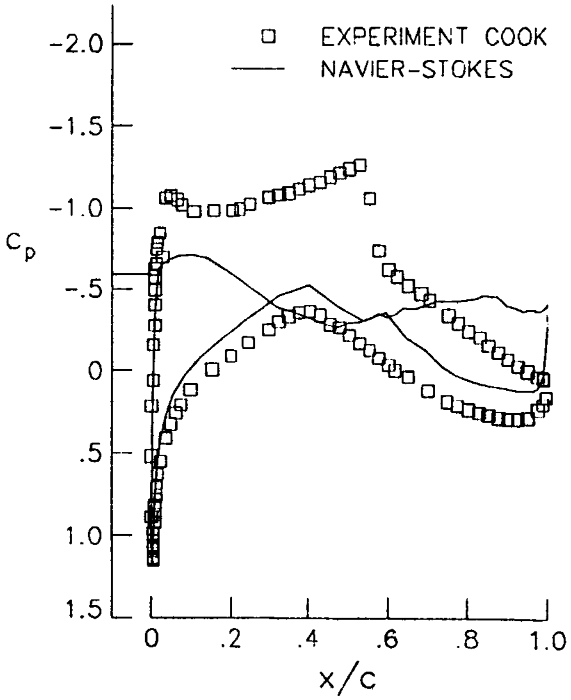

Figure 41:
Pressure distribution
Rae2822 (case 10)
original Johnson-King model
161x33 mesh (96)

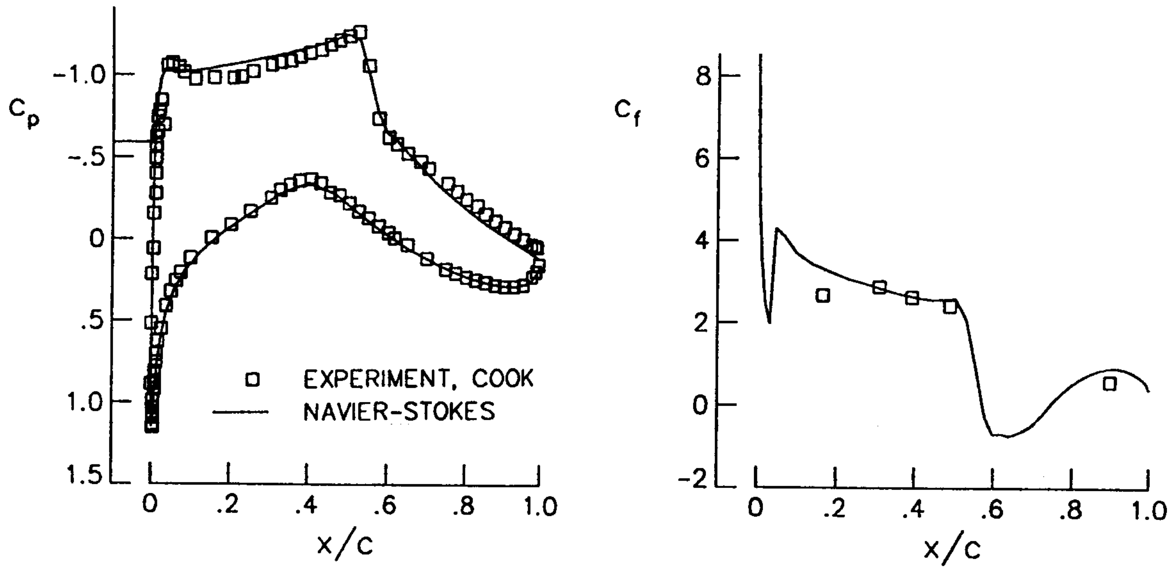

Figure 42:
Pressure distribution
Rae2822 (case 10)
J-K model with B-L formulation for $\nu_{ti\,eq}$
161x33 mesh (96)

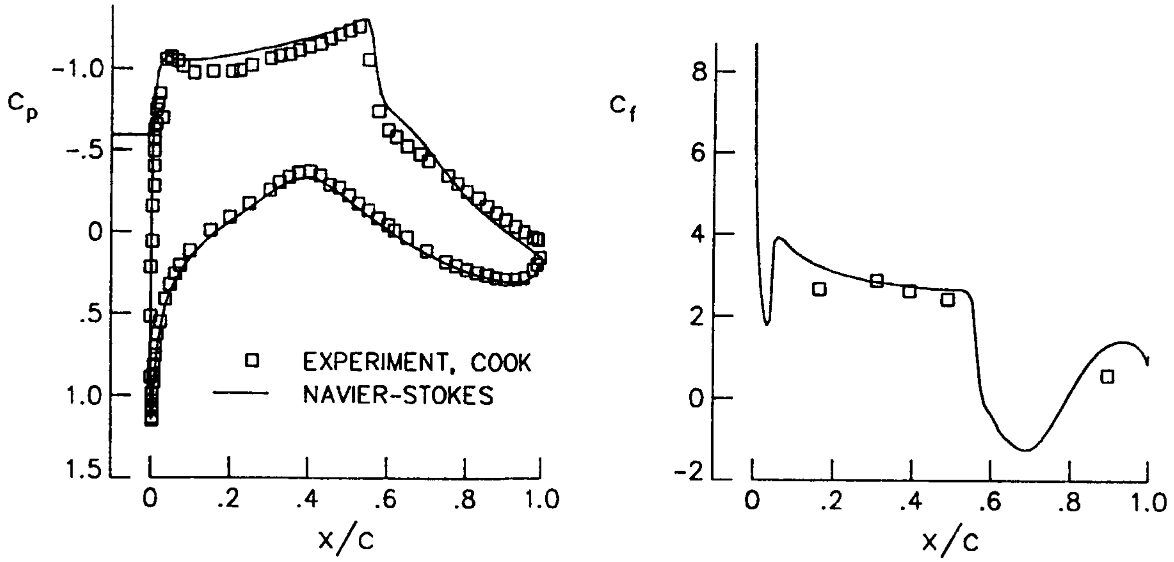

Figure 43:
Pressure distribution
Rae2822 (case 10)
J-K model with B-L formulation for $\nu_{ti\,eq}$
257x65 mesh (192)

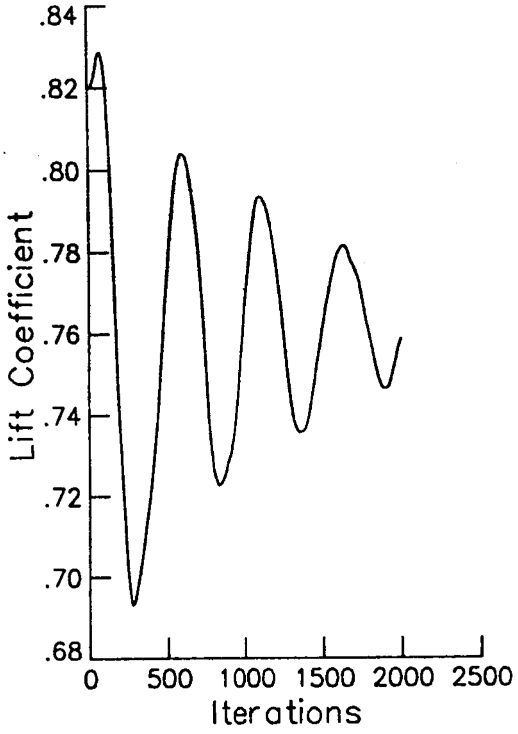

Figure 44:
Convergence history
RAE2822 (case 10)
Johnson-King model
257x65 mesh (192)

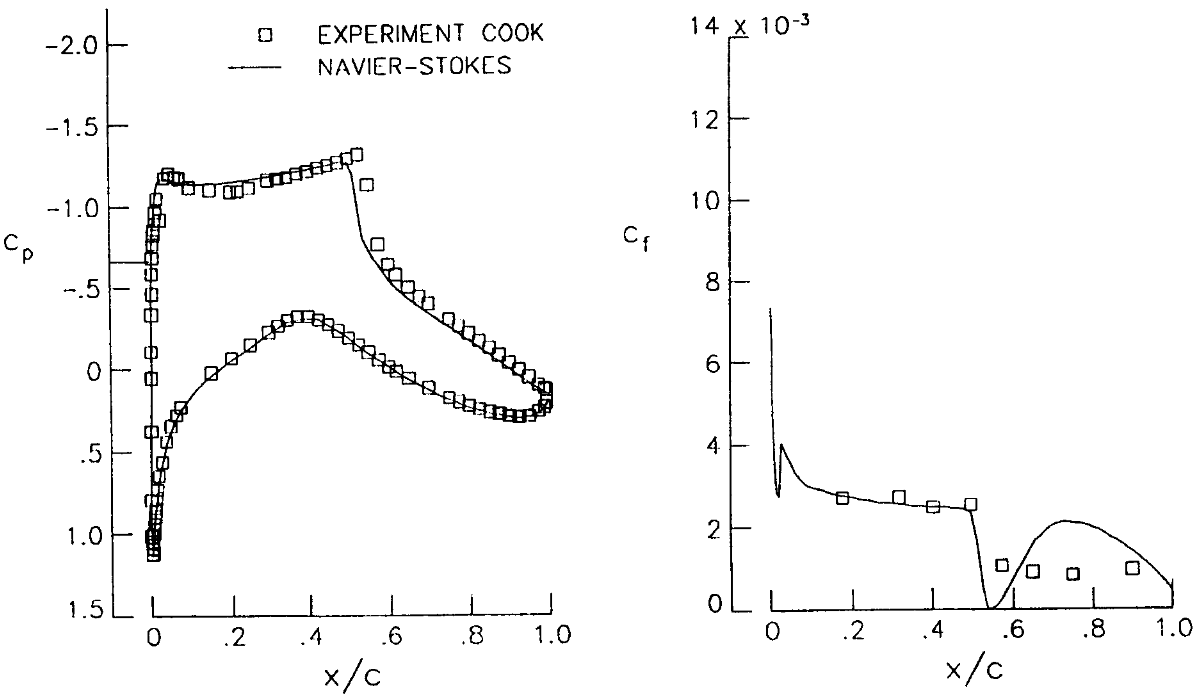

Figure 45:
Pressure and skin friction distributions
RAE2822 (case 9)
Johnson-King model
257x65 mesh (192)

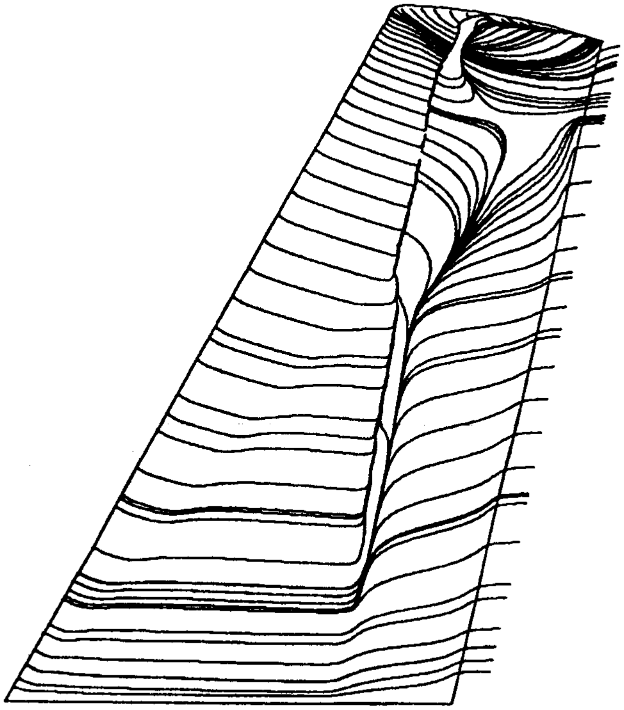

Figure 46:
Wall streanlines
ONERA M6 $M_\infty = .84$, $\alpha = 6.06$, Re $= 11 \times 10^6$
Baldwin-Lomax model
193x49x33 mesh

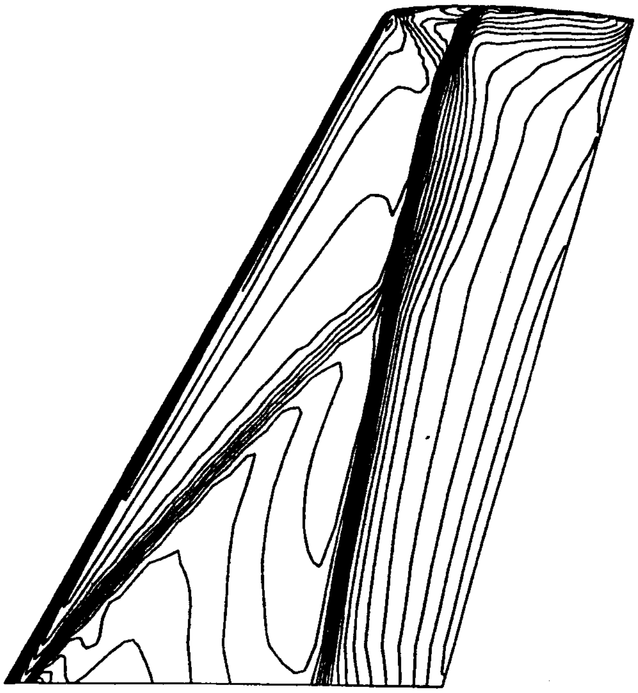

Figure 47:
Pressure contours
ONERA M6 $M_\infty = .84$, $\alpha = 6.06$, Re $= 11 \times 10^6$
Baldwin-Lomax model
193x49x33 mesh

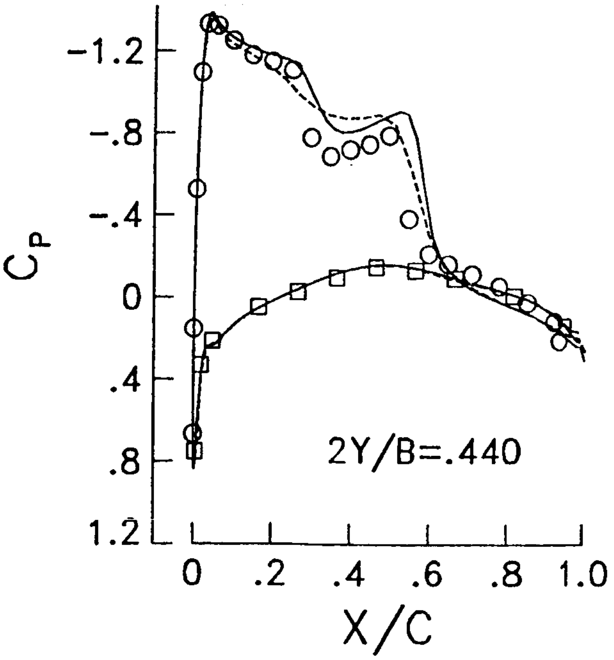

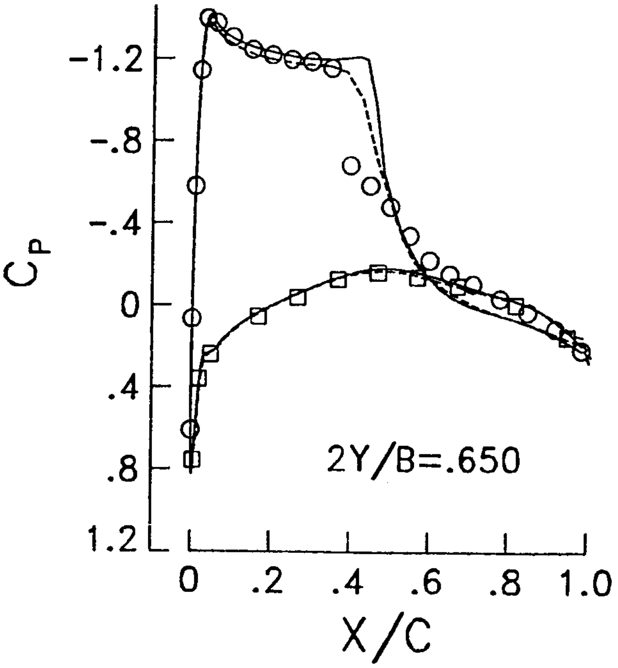

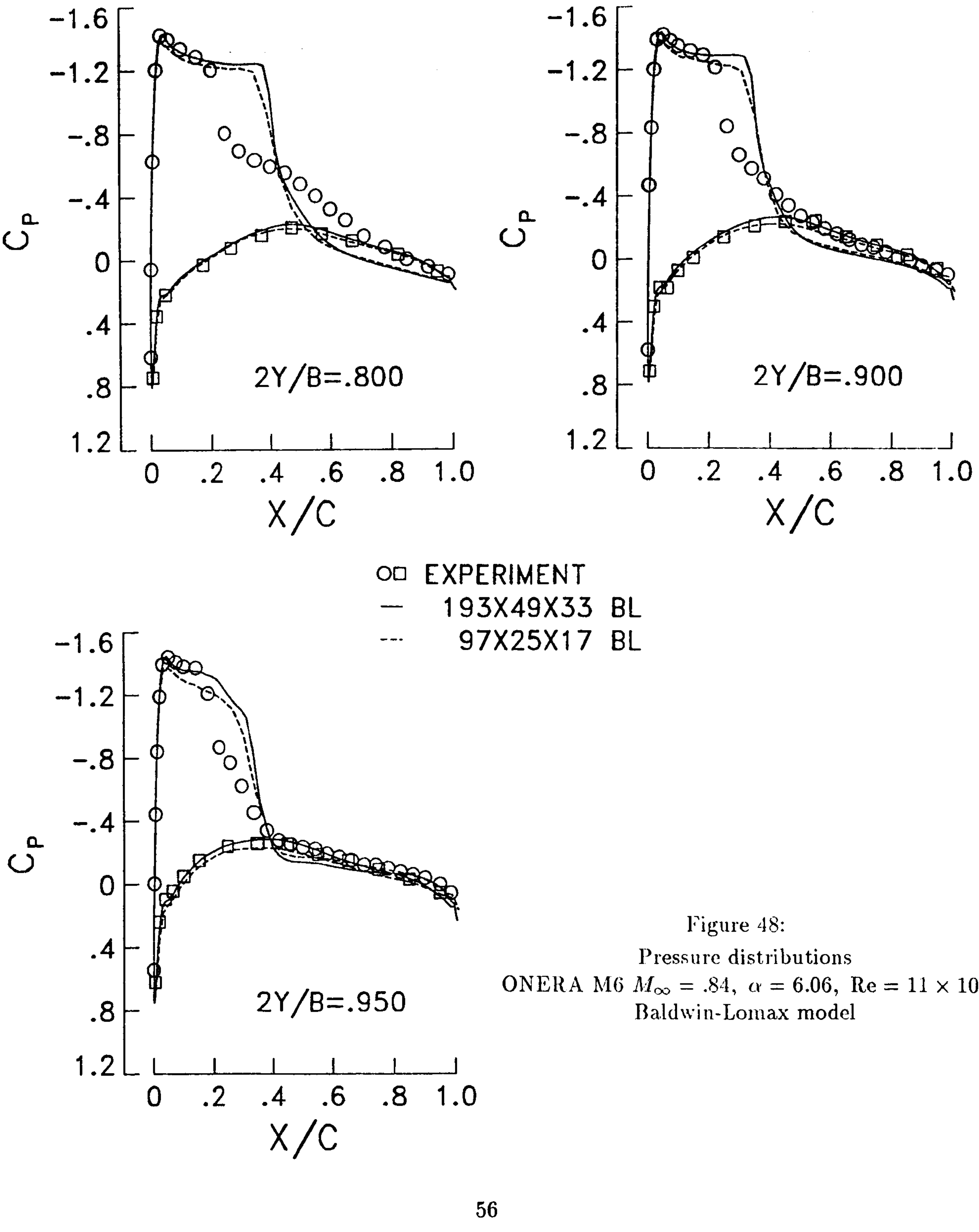

Figure 48:
Pressure distributions
ONERA M6 $M_\infty = .84$, $\alpha = 6.06$, $\mathrm{Re} = 11 \times 10^6$
Baldwin-Lomax model

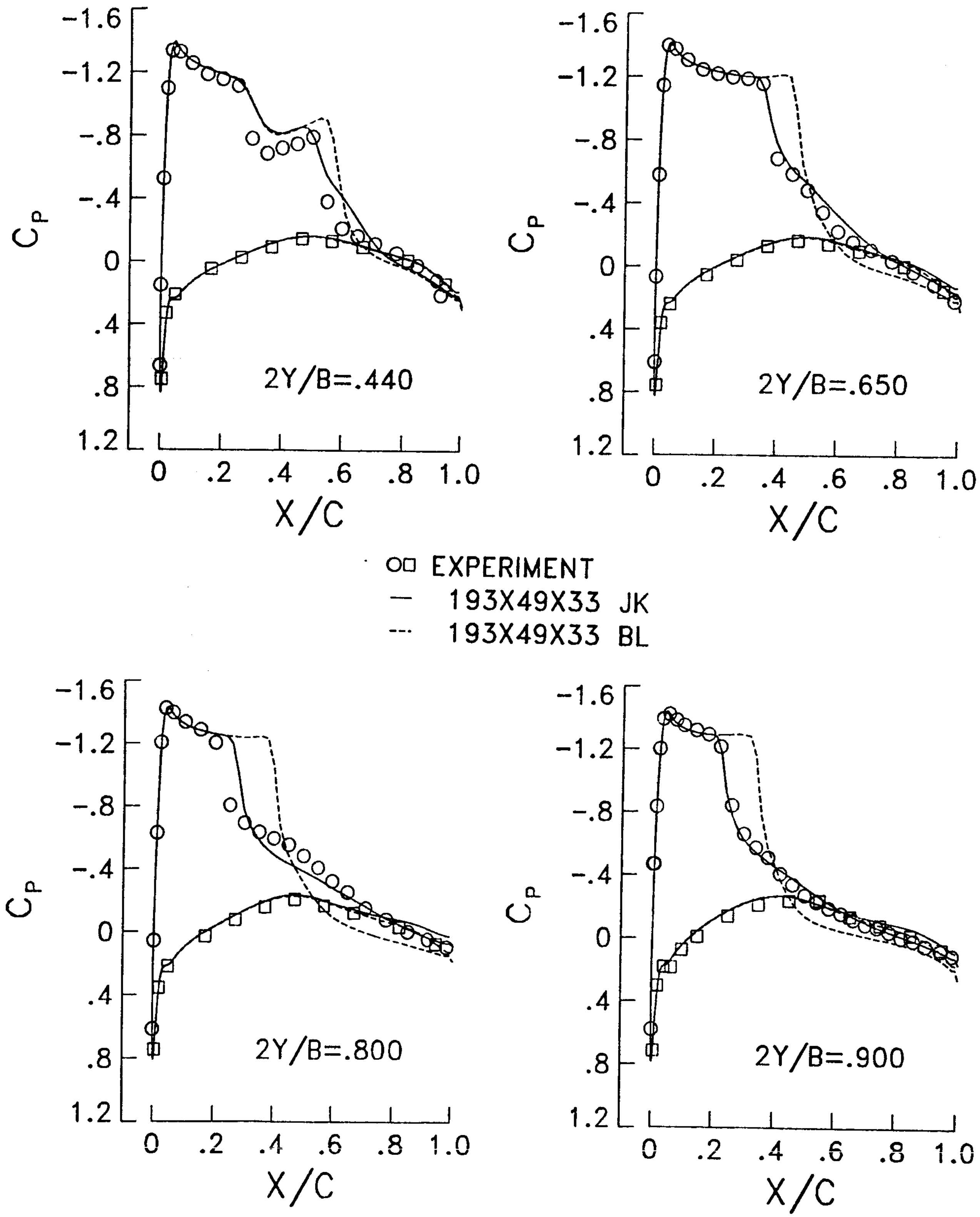

C_P
X/C
2Y/B=.440
2Y/B=.650
2Y/B=.800
2Y/B=.900
-1.6
-1.2
-.8
-.4
0
.4
.8
1.2
0
.2
.4
.6
.8
1.0
○□ EXPERIMENT
— 193X49X33 JK
--- 193X49X33 BL

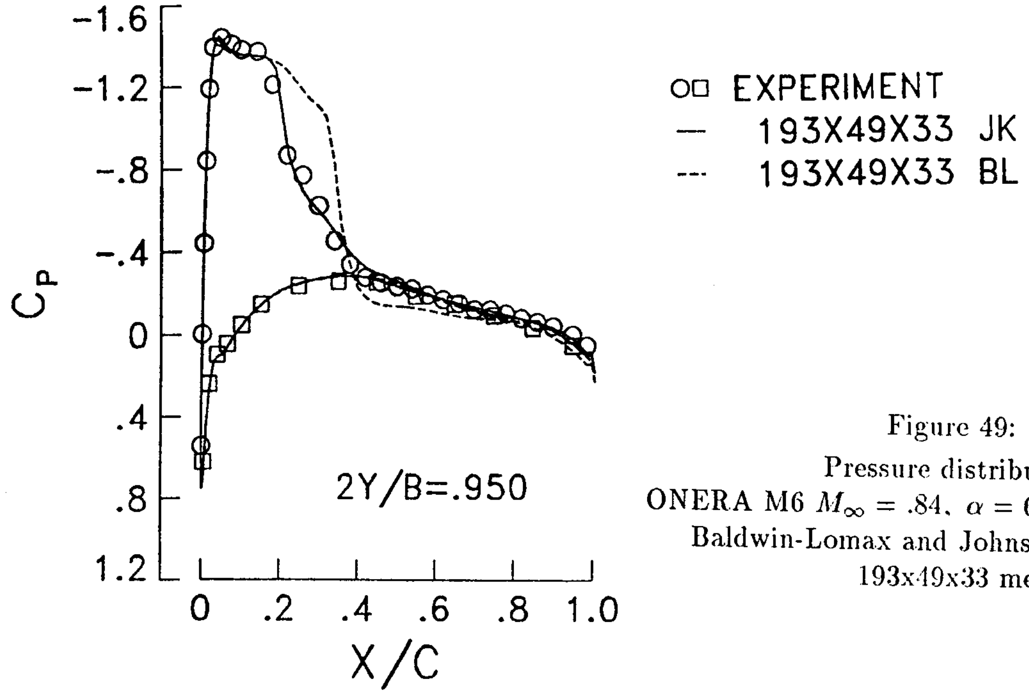

Figure 49:
Pressure distributions
ONERA M6 $M_\infty = .84$, $\alpha = 6.06$, $\mathrm{Re} = 11 \times 10^6$
Baldwin-Lomax and Johnson-King models
193x49x33 mesh

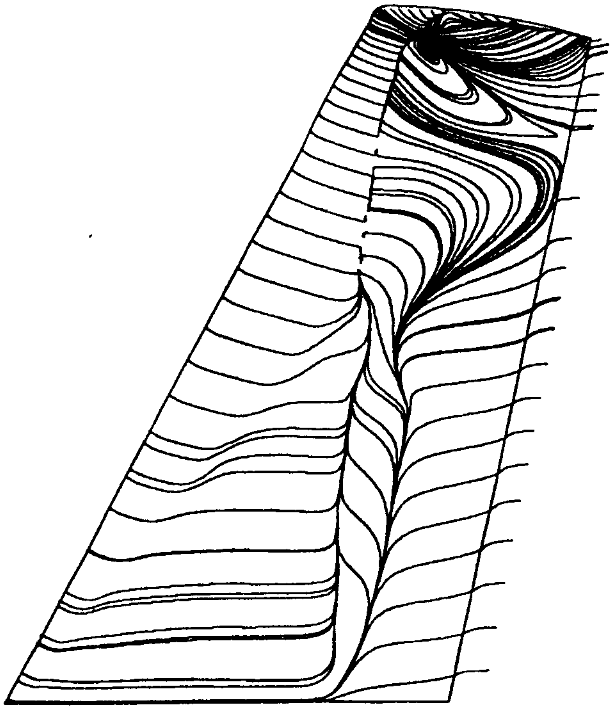

Figure 50:
Wall streanlines
ONERA M6 $M_\infty = .84$, $\alpha = 6.06$, $\mathrm{Re} = 11 \times 10^6$
Johnson-King model
193x49x33 mesh

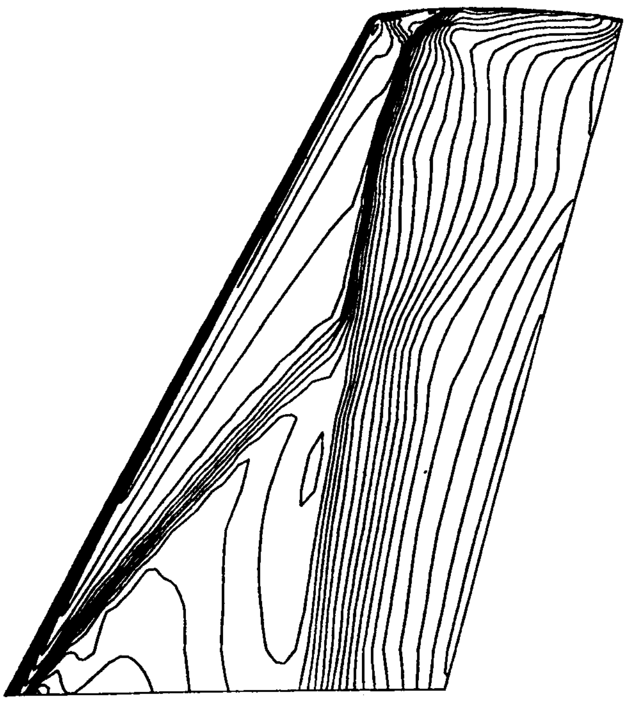

Figure 51:
Pressure contours
ONERA M6 $M_\infty = .84$, $\alpha = 6.06$, $\mathrm{Re} = 11 \times 10^6$
Johnson-King model
193x49x33 mesh

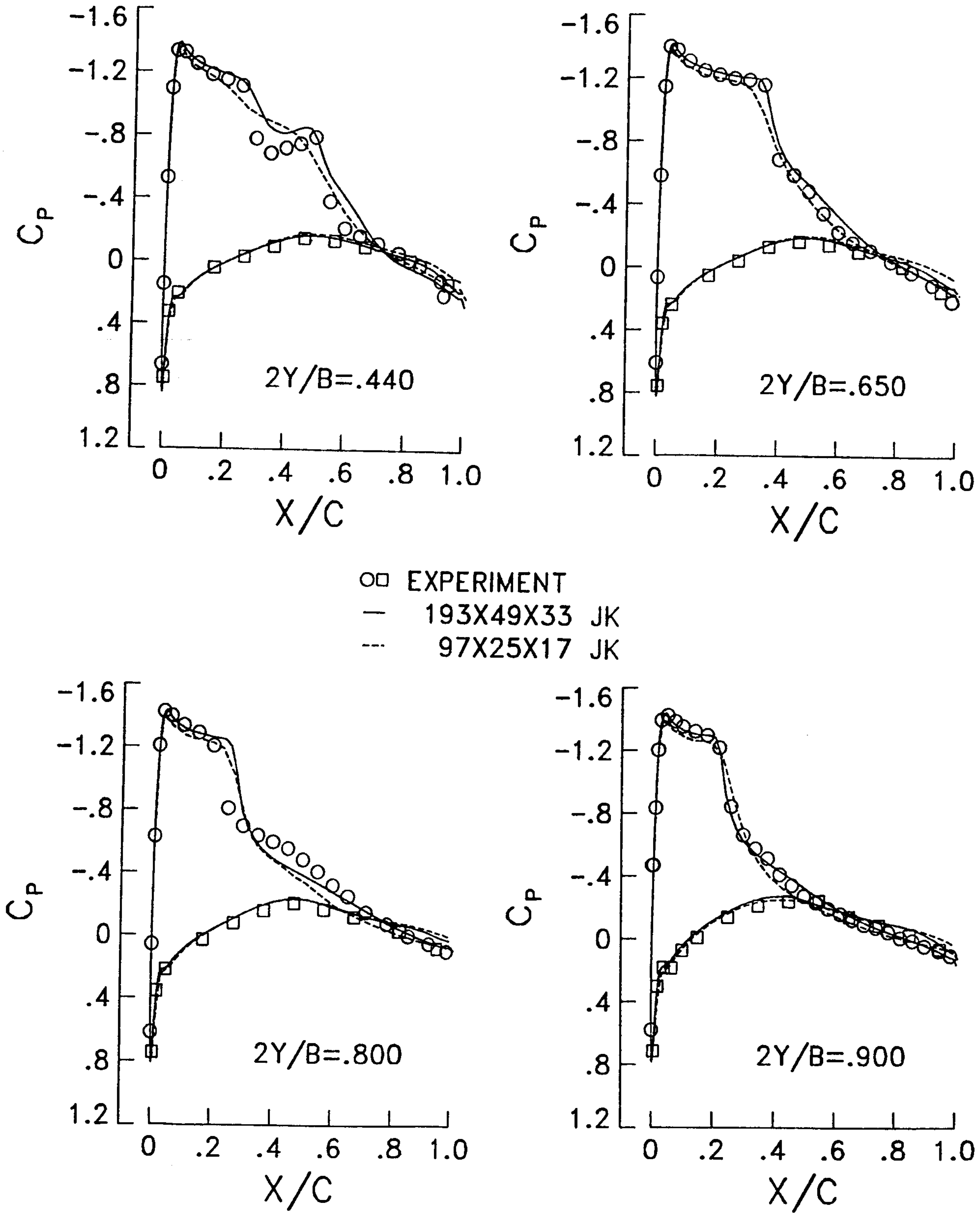

-1.6
-1.2
-.8
-.4
0
.4
.8
1.2
C_P
0
.2
.4
.6
.8
1.0
X/C
2Y/B=.440
2Y/B=.650
2Y/B=.800
2Y/B=.900
○□ EXPERIMENT
— 193X49X33 JK
--- 97X25X17 JK

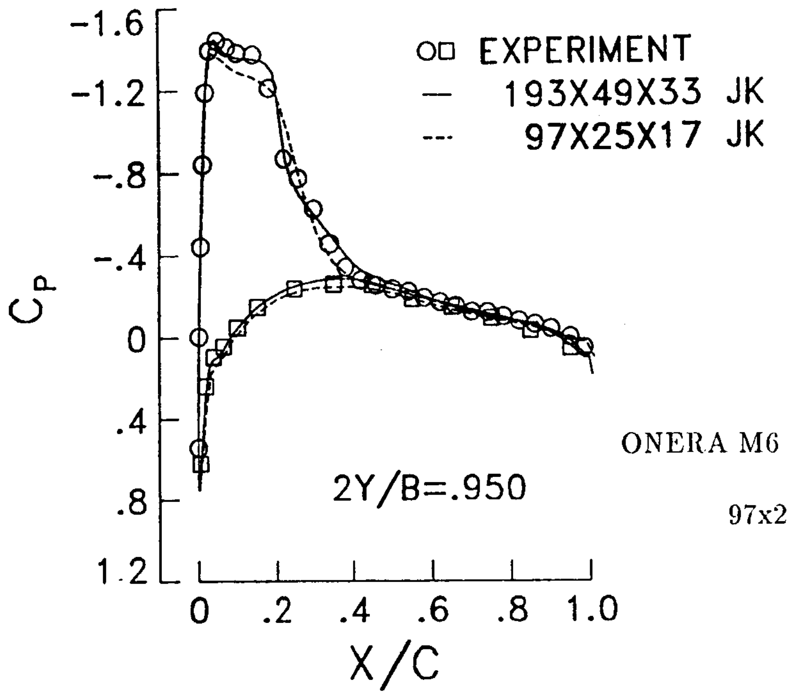

Figure 52:
Pressure distributions
ONERA M6 $M_\infty = .84$, $\alpha = 6.06$, Re $= 11 \times 10^6$
Johnson-King model
97x25x17 and 193x49x33 meshes

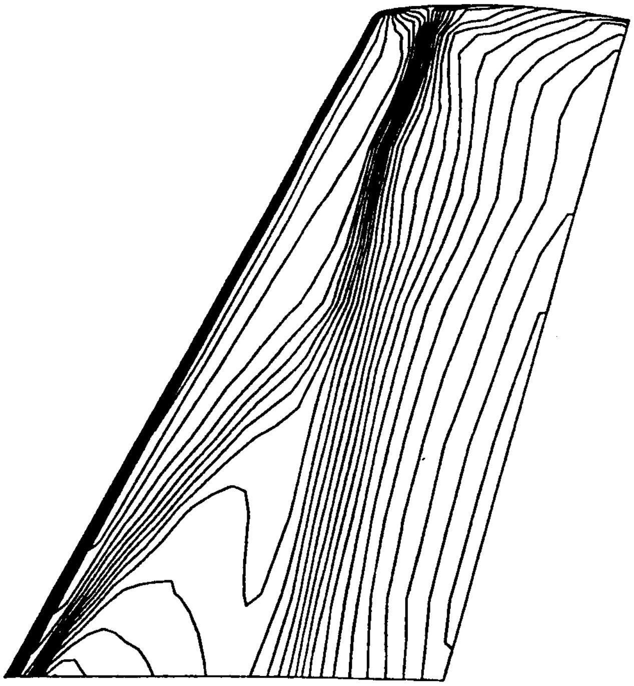

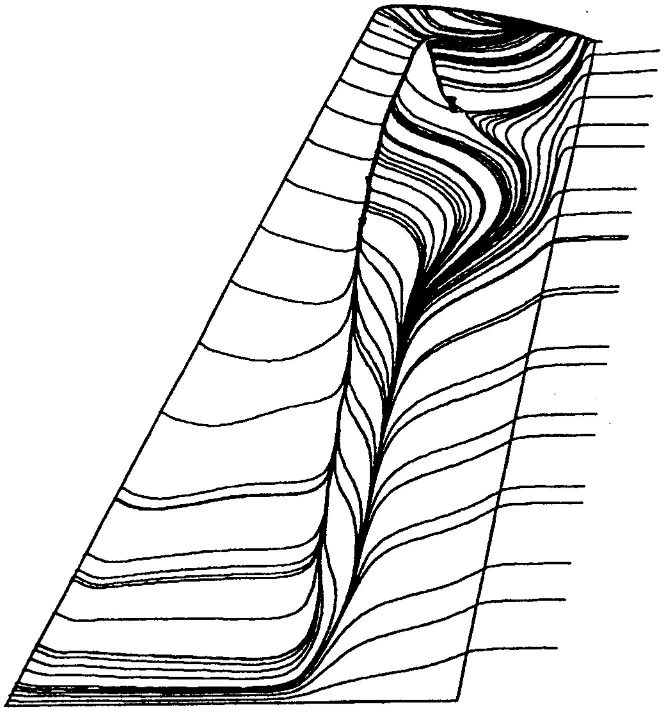

Figure 53:
Pressure contours
ONERA M6 $M_\infty = .84$, $\alpha = 6.06$, Re $= 11 \times 10^6$
Johnson-King model
97x25x17 mesh

Figure 54:
Wall streamlines
ONERA M6 $M_\infty = .84$, $\alpha = 6.06$, Re $= 11 \times 10^6$
Johnson-King model
97x25x17 mesh

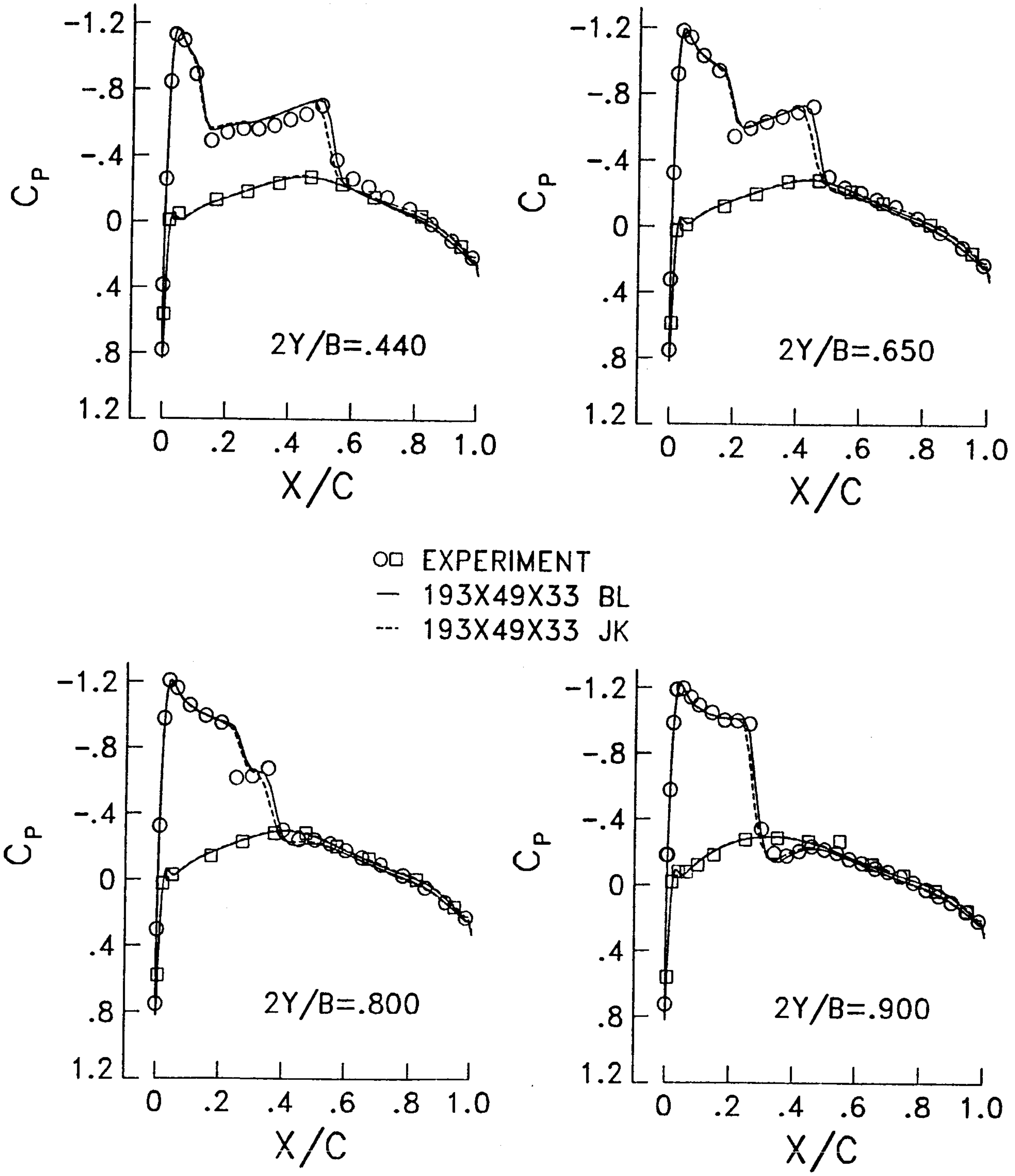
-1.2
-.8
-.4
0
.4
.8
1.2
C_P
0
.2
.4
.6
.8
1.0
X/C
2Y/B=.440
2Y/B=.650
2Y/B=.800
2Y/B=.900
○□ EXPERIMENT
— 193X49X33 BL
--- 193X49X33 JK

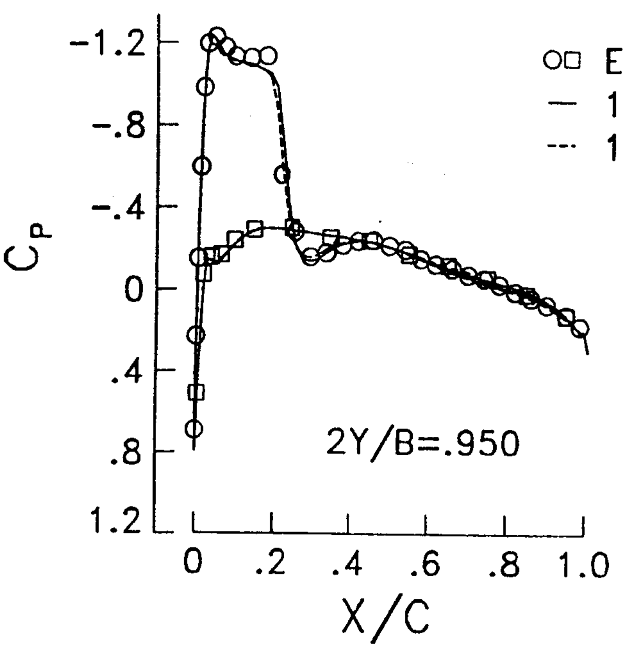

Figure 55:
Pressure distributions
ONERA M6 $M_\infty = .84$, $\alpha = 3.06$, $\mathrm{Re} = 11 \times 10^6$
Baldwin-Lomax and Johnson-King models
193x49x33 mesh

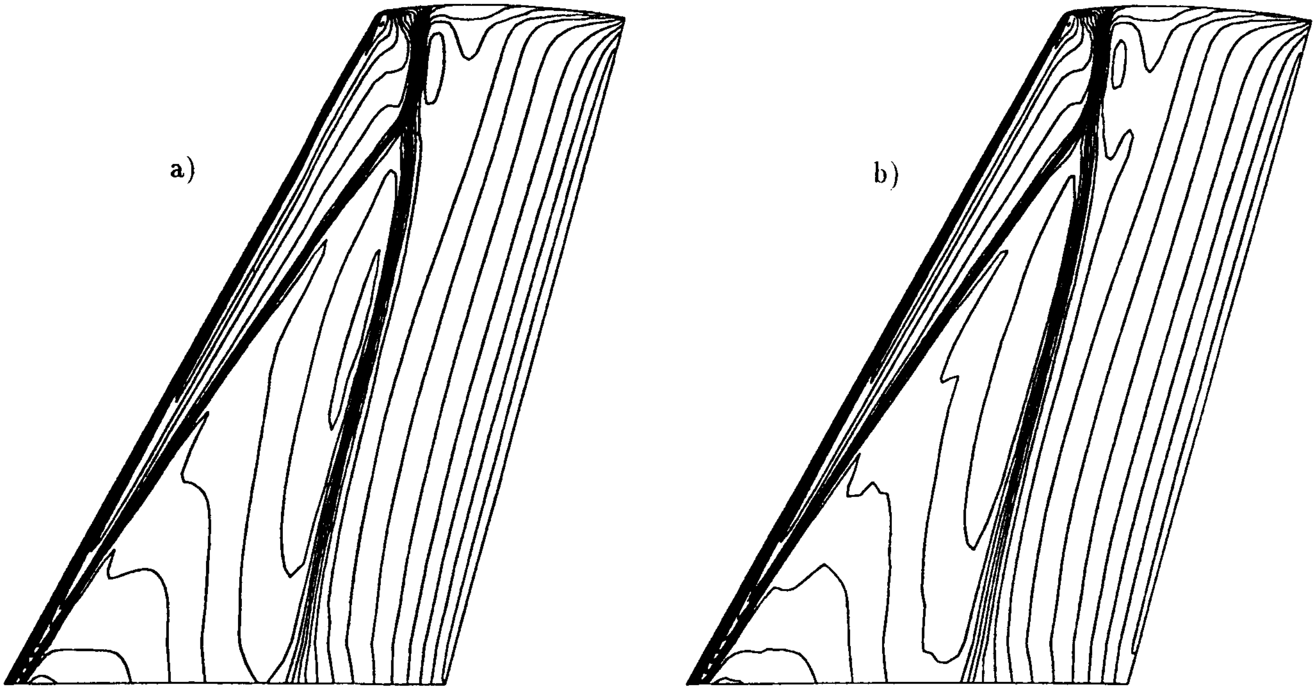

Figure 56:
Pressure contours
ONERA M6 $M_\infty = .84$, $\alpha = 3.06$, $\mathrm{Re} = 11 \times 10^6$
a) Baldwin-Lomax model
b) Johnson-King model
193x49x33 mesh

National Aeronautics and Space Administration

Report Documentation Page

1. Report No.
NASA TM-101656

2. Government Accession No.

3. Recipient's Catalog No.

4. Title and Subtitle
Numerical Solution of 3D Navier-Stokes Equations
With Upwind Implicit Schemes

5. Report Date
January 1990

6. Performing Organization Code

7. Author(s)
Yves P. Marx

8. Performing Organization Report No.

10. Work Unit No.
505-60-01-01

9. Performing Organization Name and Address
NASA Langley Research Center
Hampton, VA 23665-5225

11. Contract or Grant No.

13. Type of Report and Period Covered
Technical Memorandum

12. Sponsoring Agency Name and Address
National Aeronautics and Space Administration
Washington, DC 20546-0001

14. Sponsoring Agency Code

15. Supplementary Notes

Work was performed while the author was at Langley as a National Research Council Associate.

16. Abstract

An upwind MUSCL type implicit scheme for the three-dimensional Navier-Stokes equations is presented. Comparison between different approximate Riemann solvers (Roe and Osher) are performed and the influence of the reconstructions schemes on the accuracy of the solution as well as on the convergence of the method is studied. A new limiter is introduced in order to remove the problems usually associated with non-linear upwind schemes. The implementation of a "diagonal" upwind implicit operator for the three-dimensional Navier-Stokes equations is also discussed. Finally the turbulence modeling is assessed. Good prediction of separated flows are demonstrated if a non-equilibrium model is used.

17. Key Words (Suggested by Author(s))
Navier-Stokes Equations
Upwind Schemes
Numerical Algorithms

18. Distribution Statement
Unclassified - Unlimited

Subject Category 02

19. Security Classif. (of this report)	20. Security Classif. (of this page)	21. No. of pages	22. Price
Unclassified	Unclassified	64	A04

NASA FORM 1626 OCT 86